EPFL

Thèse n° 10 162

Electron Spin Resonance Magnetometers for Particle Accelerators

Présentée le 22 juin 2020

à la Faculté des sciences et techniques de l'ingénieur
Laboratoire de microsystèmes 1
Programme doctoral en microsystèmes et microélectronique

pour l'obtention du grade de Docteur ès Sciences

par

Anthony Jean BEAUMONT

Acceptée sur proposition du jury

Prof. C. Dehollain, présidente du jury
Dr. G. Boero, Dr M. Buzio, directeurs de thèse
Dr Ph. Lerch, rapporteur
Dr G. Severino, rapporteuse
Dr J.-Ph. Hogge, rapporteur

École polytechnique fédérale de Lausanne

2020

To my parents...

Acknowledgements

I would like to express my deepest gratitude to Dr. MER Giovanni Boero, my university supervisor, for his guidance, ideas, availability, and continuous support he has given me throughout the present work.
I am extremely grateful to Dr. Marco Buzio, my CERN supervisor, for his technical and personal supports over these years. He was always available to discuss about magnetic measurements, sensors and B-train system features. The completion of my PhD would not have been possible without his helpful and decisive contributions.
I am very thankful to Dr. Luca Bottura and Dr. Stephan Russenschuck for the opportunity they gave me to work in the CERN's magnet group and magnetic measurement section, they also gave me very good advices for the project and the proof reading of manuscripts.
A special acknowledgement to Dr. Alessandro V. Matheoud who gave me the keys to understand oscillators and PLL electronics, for his time to show and train me on the oscillator setup and measurements at EPFL.
I warmly thanks David Giloteaux, for his training on the B-Train system operation and maintenance without counting his time. He gave me crucial assistance for the design, production, tests of the various electronics boards.
Many thanks to Guy Deferne, Peter Galbraith for their support and politeness during the measurements.
I would like to thank a lot Dr. Fritz Caspers for its suggestions and time he accorded me to explain the ferrimagnetic magnetic resonance and RF features.
I thank Dr. Manfred Wendt for his availability and key advises on the design of the RF mezzanine cards.
I am grateful to Jose Bardanca Iglesias, Ricardo Beltron Mercadillo, Naim Bruti, Xavier Gontero for their help on the design and realisation of the mechanical supports. I thank Elsa Cervera, Maxime Dantas for their availability and very special cabling and soldering I requested them. I thank also Fabienne Boisier who kindly share her microscope in order that I fix the BDPA samples on the oscillator chips.
A grateful thanks to the CERN Magnetic Measurement section including the current and former B-Team team colleagues, Maria Amodeo, Martino Colciago, Vincenzo Di Capua, Christian Grech, Daniel Oberson, Marco Roda, for their supports all along the intense activities

and taking over parts of my work during the writing process of this document. In particular, I thank Melvin Liebsch, Dr. Alessandro Parrella, Trishna Rajkumar and Joseph Vella Wallbank for their support during the last phase of this document preparation.
I wish to express my thankfulness to Dr. Reyes Alemany Fernandez, Dr. Nicolo Biancacci, Stephane Cettour Cave, Denis Cote, Marc Delrieux, Dr. Gian Piero Di Giovanni, Oliver Hans, Simon Hirlander, Dr. Alexander Huschauer, Rodolphe Maillet, Dr. Bettina Mikulec, Dom Nicosa, Jean-Michel Nonglaton, Dr. Angela Saa Hernandez, Dr. Rende Steerenberg, Dr. Guido Sterbini and Dr. Frank Tecker from the Beam Department. They were always available at the CERN Central Control room to give me detailed explanations concerning the accelerators operation. They always gave me time slots during the accelerator Machine Development phases to map all my special cycles.
I address a special thanks to Dr. Simon Albright, Dr. Maria Elena Angoletta, Dr. Heiko Damerau, Alan Findlay, Michael Jaussi, Maciej Lipinski and Damien Perrelet during the B-Train validation tests of the RF, to Sebastien Tholet and Patrick Odier for the Beam instrumentation tests, and to Quentin King and Fulvio Boattini for the help in the power converter tests and explanations on the control part.
I warmly thank G. Corradini from EPFL for wire bonding, Dr. Alessandro La Rosa, Florentina Manolescu and Ian Mcgill from the Bonding and QART Labs at CERN for the wire bonding and optical measurement.
I thank Olivier Crettiez, Dr. Giancarlo Golluccio and Philip Schwarz for our Florimont's review meetings and their support especially during this critical period.
But also I thank all the CERN colleagues from the different groups and departments I worked with, and among our discussions about the wonderful land of particle physics and accelerators.

Pour finir, je remercie de tout mon cœur mes parents, ma famille et mes ami(e)s. Je vous exprime toute ma gratitude pour votre compréhension et votre soutient, plus particulièrement durant ces derniers mois où mon absence fut une constante fondamentale.

Geneva, March 6, 2020 A. B.

Abstract

CERN is the European Organization for Nuclear Research located in Geneva, Switzerland. Its main goal is to explore fundamental physics and it exists primarily to provide physicists the necessary tools for doing this, namely accelerators. These tools bring particles to almost the speed of light and then use them in different experiments. The CERN Accelerator Complex includes a chain of interconnected accelerators allowing the acceleration of charged particles up to 6.5 TeV (Tera electron Volt) per beam (for protons) in 2018 by the Large Hadron Collider (LHC). Different types of accelerator exist, but at CERN the most common are the synchrotrons. For those, the magnetic field is synchronous with the beam momentum. Magnetic models cannot be always used to predict the field within the required reproducibility, which may be as low as 10^{-5}, due to non-linear effects (eddy currents, saturation and hysteresis). Therefore, most of the CERN's synchrotrons are equipped with a real time magnetic field measurement system, the so called "B-Train". The magnetic field measurement devices are composed of absolute field sensors (called "markers"), field tracking sensors (called "induction coils"), an acquisition system, a control system that calculates the magnetic field from the sensors, and a distribution system that delivers the field value to the users. Due to the configuration of the CERN accelerator chain, if one of the injectors fails, the LHC cannot have beam. Consequently, a huge consolidation program of the real time magnetic measurement systems was launched to guarantee operation in the long term. Thus the markers are critical devices for operations at CERN and must be carefully developed to fulfil the high performance and reliability requirements of the B-Train systems.
This thesis propose new designs for electron spin resonance (ESR) field markers. We discuss in details the design, the operation, and performance of the ESR sensors based on resonator and oscillator structures including comparison between paramagnetic and ferrimagnetic samples. We propose four field marker levels at 36 mT, 106 mT, 360 mT and 710 mT that correspond to resonance frequencies of 1 GHz, 3 GHz, 10 GHz and 20 GHz. Those measurement values cover most of the marker level requirements of the CERN accelerators and achieving resolution up to 0.1 nT/Hz$^{1/2}$ for field ramps as fast as 5 T/s and field gradients as strong as 12 T/m. We conclude with measurements validation performed on the Proton Synchrotron (PS) and on the Low Energy Ion Ring (LEIR) accelerators.

Keywords— ESR,FMR, EPR, Electron spin resonance, Ferrimagnetic Resonance, Electron paramagnetic resonance, Magnetic field sensor, Field marker, B-Train, Real time magnetic field measurement, BDPA, YIG, GaYIG, CMOS oscillator.

Résumé

Le CERN est le Centre Européen pour la Recherche Nucléaire situé à Genève en Suisse. Son but principal est d'explorer la physique fondamentale en fournissant aux physiciens les outils nécessaires, dont les accélérateurs de particules. Ces outils permettent d'accélérer les particules très proches de la vitesse de la lumière et de les utiliser dans différentes expériences. Le Complexe des Accélérateurs du CERN inclut une chaîne d'accélérateurs interconnectés entre eux permettant d'accélérer en 2018 les particules chargées jusqu'à 6.5 TeV (Téra électron-volts) par faisceaux de protons grâce au Grand Collisionneur de Hadron (LHC). Différents types d'accélérateurs existent, mais au CERN, les plus répandus sont les synchrotrons. Pour ceux-ci, le moment des particules est synchrone avec le champ magnétique. Pour ce faire, le courant d'excitation des électro-aimants et de la Radiofréquence d'accélération doit croître de manière synchrone. Les modèles magnétiques ne permettent pas toujours de prédire le champ magnétique avec la répétabilité requise, qui peut atteindre dans certains cas 10^{-5}, et ceci dû à des effets non-linéaires, tel que les courants de Foucault, la saturation et l'hystérésis. C'est pourquoi, la plupart des synchrotrons du CERN sont équipés de systèmes de mesure du champ magnétique en temps réel, appelé « Train-B ». Ces équipements de mesure sont composés de capteurs de champ absolu (appelés « marqueurs »), de capteurs de mesure de variation du champ (appelé « bobine »), d'un système d'acquisition, d'un système de contrôle qui permet de calculer le champ magnétique à partir des capteurs et d'un système de distribution qui envoie le champ mesuré aux utilisateurs. Étant donnée la configuration de la chaîne des accélérateurs au CERN, si l'un des Train-B des injecteurs a un défaut, le LHC ne peut plus avoir de faisceau. Pour cette raison, une rénovation de grande ampleur des systèmes de mesure en temps réel a été lancée, afin de garantir un fonctionnement optimal sur le long terme. C'est pourquoi, les marqueurs de champ magnétique sont des équipements essentiels pour un bon fonctionnement au CERN, et doivent être en conséquence développés avec une grande attention pour atteindre les hautes performances et la fiabilité requises pour les Train-B. Cette thèse propose des nouvelles conceptions de marqueur de champ par résonance de spin électronique (RSE). Nous discutons en détail de la conception, du fonctionnement et des performances des capteurs RSE se basant sur des structures résonantes et oscillantes, incluant une comparaison entre des échantillons paramagnétiques et ferrimagnétiques. Nous proposons quatre niveaux de marqueurs de champ à 36 mT, 106 mT, 360 mT et 710 mT ce qui correspond à des fréquences de résonance magnétique à 1 GHz, 3 GHz, 10 GHz et 20 GHz. Ces valeurs couvrent la plupart des niveaux de marqueurs nécessaires pour les accélérateurs du

CERN. Ceux-ci permettent d'atteindre des résolutions jusqu'à 0.1 nT/Hz$^{1/2}$ pour des rampes de champ aussi rapides que 5 T/s, ainsi que des gradients de champ aussi forts que 12 T/m. Nous concluons ce document avec des mesures de validation effectuées en conditions réelles dans les accélérateurs Proton Synchrotron (PS) et l'Anneau pour Ions à Basse Énergie (LEIR).

Mots clés— RSE, RFM, RPE, Résonance de spin électronique, Resonance ferrimagnétique, Résonance paramagnetique électronique, Capteur de champ magnétique, Marqueur de champ, Train-B, Mesure de champ magnétique en temps réel, BDPA, YIG, GaYIG, oscillateur CMOS.

Contents

List of Figures

List of Tables

Introduction

Nowadays particle accelerators are widely used, as almost 35000 machines with particle energy above one million electron-Volt [1] (MeV) are in operation. Among those, about 50% are dedicated to microelectronics (e.g. ion implanter and surface modification), industrial research and processes (e.g. synchrotron light source, material study), while 49% are for medical applications (radiotherapy, research). Only 1% of the accelerators with particle energy above 1 GeV are dedicated to particle physics [1, 2]. The largest accelerator in the world is the Large Hadron Collider (LHC), with collisions up to a center-of-mass energy of 13 TeV. The LHC is operated at the European Organization for Nuclear Research (CERN) since 2010.

Synchrotrons are a common type of high-energy particle accelerator, where the momentum of the particles is proportional at all times to the magnetic field needed to keep the particles beam on the closed orbit at the center of the vacuum chamber. As a result, the frequency of the RF resonant cavities used to accelerate the beam must be controlled as a function of the instantaneous value of the field in the main bending magnets [3]. Often, the field can be predicted with sufficient accuracy from mathematical models that take as input the excitation current of the bends [4]. In certain cases, such as in five of the synchrotrons of the CERN complex, as well as in several hadron-therapy accelerators, perturbations due to hysteresis and dynamic effects in the iron yoke of the magnets are so large that real-time feedback becomes necessary [5]. This is provided by specialized measurement systems called "B-trains", based on an induction coil to track field changes. An additional absolute sensor, known as a field marker, provides the integration constant by generating a trigger pulse whenever a pre-set field value is reached. Emphasis is put on the stability and reproducibility of the marker field measurement rather than on its absolute accuracy.

Among the possible choices for the field marker [6], Hall-effect sensors, peaking strips, and magnetic resonance based sensors have been used with success in the past. Hall sensors are widely available and inexpensive but need frequent re-calibration to provide sufficiently accurate results. Peaking strips are limited in the field range due to the need of a bias field source. Magnetic resonance methods, on the other hand, are particularly appropriate for the role of markers since their operation is based on parameters related to fundamental constants, such as the gyromagnetic ratio, which links the resonance frequency to the magnetic field

[1] 1 eV=1.602×10^{-19} Joules

value.
Considerable experience has been accumulated at CERN with nuclear magnetic resonance (NMR) probes as field markers. However, in spite of their excellent accuracy and resolution, these sensors are typically well suited only for relatively uniform. A very promising alternative is represented by a class of sensors based on different forms of electron spin resonance (ESR).

The main objective of this work is to design, develop, evaluate and implement new ESR magnetic field sensors. The markers operate at specified field levels (36 mT, 106 mT, 360 mT, and 710 mT) (i) in strong magnetic field gradients up to 12 T/m (ii) at high time-transient fields up to 5 T/s and (iii) with a resolution better than 10 nT/Hz$^{1/2}$. Ferrimagnetic and paramagnetic materials applied to magnetic resonance are used in this work. The thesis is divided in the following three main parts:

- **Overview and background** on magnetic field measurements in the context of particle accelerators (Ch. 1) and state-of-the-art of ESR in the field of magnetic field measurements (Ch. 2).
- **Characterization of ESR sensors**:
  The calibration benches used for the metrological characterization of the sensors are illustrated in Ch. 3.
  The design of the resonator structure with the lumped elements is presented in Ch. 4.
  Ch. 5 describes the resonator with the grounded co-planar waveguide.
  In Ch. 6, the metrological characterization of the ferrimagnetic resonance (FMR) sensors is presented. In particular the sensitivity to the field ramp rate, the dependency upon the temperature and the effect of the field direction are discussed.
  The metrological characterization of the electron paramagnetic resonance (EPR) sensors is illustrated in Ch. 7. Emphasis is put on the signal and noise computation, along with the performance of the resonator sensors with paramagnetic material sample at 36 mT and 106 mT field marker levels.
  Ch. 8 describes the use of integrated LC oscillators in the context of high field sensor applications, especially the performance of the oscillators for the 360 mT and 710 mT EPR marker field levels.
- **Experimental validation of the FMR sensors during the operation of particle accelerators**. Operation of the FMR sensor at 36 mT in the Proton Synchrotron (PS) reference magnet is discussed in Ch. 9.
  Ch. 10 details the overall performance of the B-Train system in the Low Energy Ion Ring (LEIR) synchrotron machine. This includes the 106 mT FMR sensor operation and the result during an extensive B-Train reliability run, carried out in coordination with the Low Level Radio Frequency (LLRF) and the particle beam dynamics teams.

A part of this chapter is reproduced with changes from [7], with the permission of AIP Publishing.

Part I Overview and background

1 Real time magnetic field for synchrotron particle accelerator

1.1 Accelerators for particle physics

Particle physics is the study of elementary particles like electrons, quarks, muons, neutrinos and the four forces:

- Strong interaction between quarks by gluon (e.g.: given proton, neutron)
- Weak interaction (origin of the atom fission)
- Electromagnetic interaction between charged particles by photon (for example chemical phenomenon)
- Gravitation interaction between everything that has mass (influent at macroscopic scale)

Particles can be studied by cosmic rays, nevertheless many of them have short life time before given other particles more stable and the events rate is low.
Accelerators create artificially many particles in a closed and controlled environment. Accelerators give energy to charged particles circulating at up to 99.9999991% of the speed of light (at 6.5 TeV in the LHC). When they collide or hit a fixed target, their own energy is transformed into matter and vice versa (in accordance with the theory of relativity by Albert Einstein). Detectors allow measuring the number, charge, energy and mass of particles in order to observe them similar to microscope for cellules and telescope for stars. Among large applications, accelerators combined with detectors serve for fundamental research on (i) elementary particles and forces (Standard Model study) (ii) the dark matter study (iii) the dark energy study and (iv) antimatter study.

1.2 Synchrotron particle accelerator

The CERN accelerators complex shown in Fig. 1.1 accelerates charged particles up to an energy of 6.5 TeV (in 2018) per particles beam with the LHC for collisions up to 13 TeV. To achieve this, a chain of accelerators are connected together to successively inject then extract the beam up to the top energy. The synchronisation between the accelerators is a key factor to allocate the

beam either to the next machine or to experimental areas.

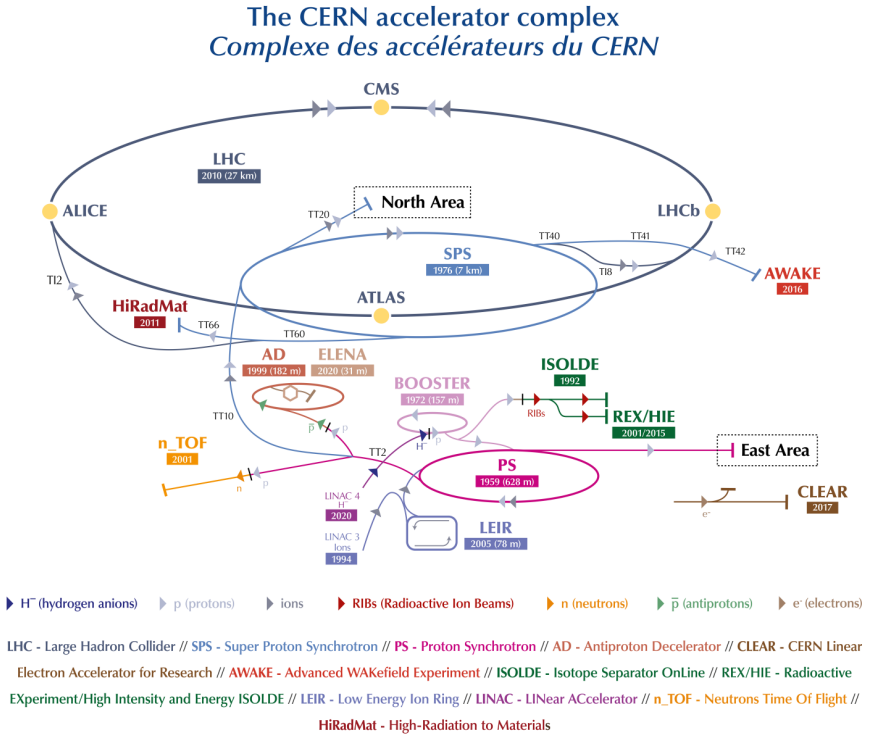

Figure 1.1 – The CERN accelerator complex in 2019 [8].

CERN has five synchrotron accelerators (LEIR, PSB, PS, SPS, LHC) and two synchrotron decelerators (AD, ELENA). Synchrotrons [9] are circular machines composed of RF cavities to accelerate (or decelerate) the beam and magnets to guide the beam. The particle beam circulates inside a vacuum pipe to minimize the interactions with surrounding particles. Many other devices are installed all around the ring to ensure the diagnostic of the beam, the injection, the extraction and the machine protection.
Charged particles are governed by Lorentz forces **F** given by

$$\mathbf{F}(t) = q(\mathbf{E}(t) + \mathbf{v}(t) \times \mathbf{B}(t)) \tag{1.1}$$

where t is the time, q is the electric charge, **E** is the electric field, **v** is the particle velocity and **B** is the magnetic flux density refereed later in this work as the magnetic field for sake of simplicity[1].

For synchrotrons, the electrical and the magnetic field quantities must be driven synchronously to maintain the beam in a stable closed orbit. As a matter of fact, from Eq.(1.1) the electric field can be used to accelerate or guide the charged particles, but for practical reasons (and

[1] When needed, we distinguish the magnetic flux density B from the magnetic field H.

strength), the electric field is dedicated to the acceleration. There are few exceptions, such as radio frequency quadrupole (RFQ) in linear accelerators (Linacs) and electrostatic septum in the beam injection-extraction areas, which use the electric field to guide the beam. Conversely, the cross product in Eq.(1.1), that is, **F** is always orthogonal to **v** and **B**, avoid longitudinal acceleration by the magnetic field. Only indirect approach is possible. In particular, a magnet called "betatron core" [10], which converts the time-transient toroidal magnetic field into a constant axial electric field (during the magnetic field ramps).

For a circular orbit, the transversal force corresponds to the centrifugal force to be compensated by the Lorentz force, that is, $F_L = q\mathrm{v}B$. The particle momentum p (in eV/c) is given by

$$p = qB\rho \tag{1.2}$$

where $B\rho$ is the beam rigidity (in Tm), and ρ is the radius of curvature.
The total energy E (in eV) is given by

$$E = \frac{pc^2}{\mathrm{v}} \tag{1.3}$$

where c is the speed of light in vacuum. $E = E_k + E_0$ where E_k is the kinetic energy and E_0 is the rest energy with $E_0 = 938.27$ MeV for the proton. For relativistic particles $E \equiv p$, this assumption is valid in the SPS and in the LHC.

1.3 Magnets

As recall, the charged particle beam is guided by the magnetic field induced by magnets. Three main types are commonly used:

- Permanent magnet; the magnetic field is induced by hard ferromagnetic materials.
- Iron-dominated electro-magnet; the magnetic field is induced by excitation coils supplied by an electrical current, where the flux is guided by soft ferromagnetic materials.
- Coil-dominated electro-magnet; the magnetic field is induced by excitation coils supplied by an electrical current, with a specific geometry, to obtain the expected magnetic field profile.

The third type is generally made of superconducting coils to produce a very high DC field in a large aperture. As example, the field in the LHC main dipole is 8.3 T with an aperture diameter of 56 mm for a current of 11 kA.
However, it exists sub-types of the aforementioned magnets. Typically, hybrid-magnets [11] where the main field is induced by permanent magnets with an additional correction field induced by iron-dominated magnet. There are also superferric magnets that are composed of ferromagnetic yoke with superconducting coils [12].

The magnets are designed to produce different magnetic field profiles determined by the wanted effect on the beam. Those effects and magnetic field types are listed below:

- Bending; by dipole field.

- Focusing and defocusing called "*tune*" [13]; by quadrupole field.
- Chromatic aberration correction called "*chromaticity*" [14]; by sextupole field
- Landau damping [15] or multi-turn extraction [16]; by octupole field.

Higher order magnets than sextupole are typically used to correct the multipoles created by the main magnets.
This is why, the magnetic flux density used in particle accelerators are generally expressed as a Fourier series expansion [17, 18] in the two dimensions imaginary planes for the integral in long straight magnets

$$\mathbf{B}(\mathbf{z}) = B_y + iB_x = \sum_{n=1}^{\infty} (B_n + iA_n)\left(\frac{\mathbf{z}}{R_\mathrm{r}}\right)^{n-1} \tag{1.4}$$

where $\mathbf{B}$ is the field integral parallel to the beam axis, $\mathbf{z} = x + iy$, n is the mulipole order ($n = 1$ dipole, $n = 2$ quadrupole, etc...), B_n is the normal magnetic field component, A_n is the skew magnetic field component, and R_r is the reference radius.

1.4 Magnetic measurement for magnets

Magnetic measurements (MM) in particle accelerators are performed before the magnet installation, as part of the quality assurance. Four main types of measurement are required in an accelerator

- The absolute value of the main field component, that is its strength.
- The field homogeneity or field harmonics.
- The field direction of the main component.
- The magnetic center for quadrupole and higher order magnets.

The last two measurements are used for the alignment of the magnet in the machine.
Two additional measurements can be conducted regarding the magnet operation. First, the eddy currents strength and decay time can be measured for pulsed magnets. And second, the 3D field map can be performed for the beam tracking survey of spectrometer magnets.

At CERN, many measurement devices are based on induction coils (in Sec. 1.5.2), such as rotating coils [19, 17, 20], single stretch wire technique [21, 22] and translating fluxmeter [23]. When the magnets are pulsed (typically for the synchrotrons), the approach with static fluxmeter [24] is privileged.
Lorentz force based sensors are also used, in particular, the oscillating wire [25] and the vibrating wire [26]. NMR sensors are also widely used to calibrate the aforementioned MM measurement equipment.

Nevertheless, many other measurement techniques exist with their own characteristics. L. Bottura and K. N. Henrichsen [27] resumed in Fig. 1.2 the general magnetic field measurement with their typical range and accuracy levels.

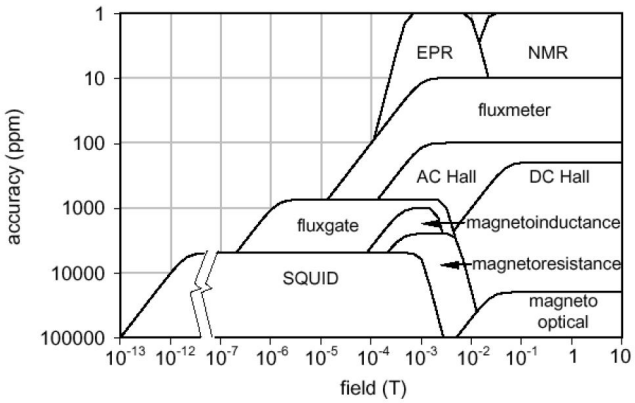

Figure 1.2 – Accuracy and range of general magnetic measurement methods [27].

1.5 Real time magnetic field measurements

As aforementioned, for iron-dominated magnets the field cannot be predicted with sufficient accuracy from mathematical models in the LEIR, PSB, PS, ELENA, and the SPS of the CERN's synchrotrons, therefore the real-time feedback becomes necessary [5]. The B-Train systems are based on an induction coil to track field changes and an additional absolute sensor to provide the integration constant (B_m in the Eq.(1.5)). The appropriate correction is found as part of the normal procedure following any major operational change or maintenance stop, which is known as energy matching [28]. In practice, the extracted beam from the upstream accelerator chain is injected into the downstream accelerator with all the RF feedback systems deactivated. The position of the beam at injection is measured during several turns (from 200 to 800 turns) in the accelerator, then the reference field is corrected such that the beam position at injection is on the closed orbit.

The magnetic flux density $B(t)$ is measured in real-time in the gap of a suitable main bending reference magnet written as

$$B(t) = \kappa\left(B_\mathrm{m}(t_\mathrm{k}) + \frac{\upsilon}{K_\mathrm{c}}\int_{t_\mathrm{k}}^{t} V_\mathrm{c}(\tau)\,d\tau\right) \tag{1.5}$$

where κ is the global gain correction factor, B_m is the field marked at the time t_k, $k = 1, 2...$ for the low and high field markers, υ is the integral gain correction factor, K_c is the effective area of the induction coil, and V_c is the induced voltage in the coil. The actual implementation of Eq. (1.5) in the CERN B-train systems includes additional offset and gain factors [5] to compensate for various kinds of errors, ensuring that the mean radial position [29] of the beam is centred in the vacuum chamber. The magnetic field varies cyclically as the particles are injected, accelerated and extracted, as shown schematically in Fig. 1.3. Integration is restarted when the trigger from the field marker is received at least once per cycle, as necessary

A part of this chapter is reproduced with changes from [7], with the permission of AIP Publishing.

to limit the build-up of integrator drift. The field marker could be, in principle, set at any arbitrary level during the cycle. However, since the beam is most sensitive to perturbations during the injection phase, a low field level just below injection is often chosen (t_1 in Fig.1.3). Optionally, a second marker (t_2) is introduced in order to improve the drift correction. In this case, choosing the highest field level possible allows calibrating accurately the gain of the whole acquisition chain.

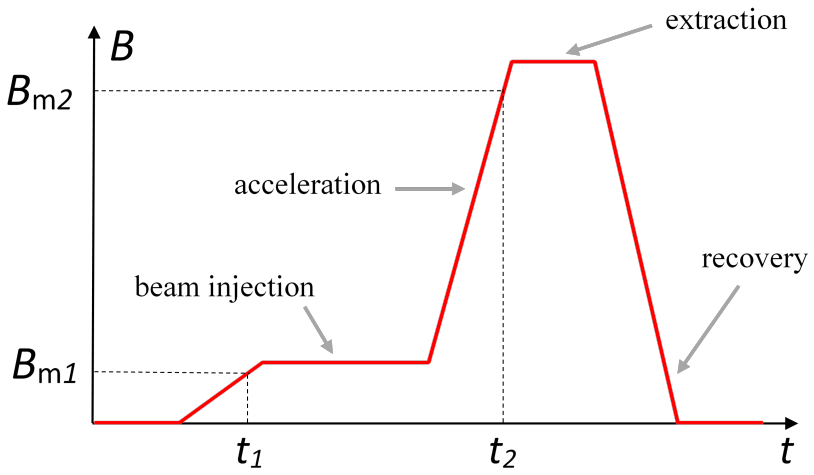

Figure 1.3 – A typical synchrotron accelerating magnetic cycle.

The real-time magnetic field is generally distributed to three users:

- The LLRF control system.
- The beam current transformer control system.
- The power converter control system.

Side users are also involved, such as the general MM White Rabbit [30] diagnostic system [31] and the beam dump of the SPS.

For the LLRF system, the revolution frequency $f_{\mathrm{rev}}(t)$ is determined according to the main bending magnetic field given by

$$f_{\mathrm{rev}}(t) = \frac{c}{2\pi R}\sqrt{1-\frac{1}{1+\left(\frac{B(t)\rho q}{m_0 c}\right)^2}} \tag{1.6}$$

where R is the mean orbit radius, and m_0 is the particle's rest mass. The revolution frequency is controlled via additional correction and feedback terms that are detailed in the literature [32, 33, 34].

The beam current transformer measures the beam current [35, 36] in order to determine the

number of particles per beam $N_p(t)$ given by

$$N_p(t) = \frac{2\pi R}{qc} \frac{\sqrt{\left(B(t)\right)^2 + \left(\frac{m_0 c}{q\rho}\right)^2}}{B(t)} I_{BCT}(t) \tag{1.7}$$

where I_{BCT} (in A) is the measured equivalent current. The correction of the particle momentum by the magnetic field is especially relevant for non-relativistic particles (i.e., below the relativistic gamma transition in the LEIR, PSB, PS, and ELENA synchrotrons).

The power converter can use the B-Train to regulate in magnetic field the main bending magnets[2]. The advantage is a significant cycle time gain, because the eddy currents, the magnetic saturation and the hysteresis effect of the magnets are intrinsically corrected. The power converter is voltage controlled by a R-S-T feedback-feedforward regulator [37, 38] with a magnet model given by

$$V_{ref}(s) = B(s)\left(sK_m + \frac{R_m}{L_m}K_m\right) \tag{1.8}$$

where V_{ref} is the voltage applied across the main bending magnets, s is the Laplace variable, R_m is the total main bending magnets resistance, L_m is the total main bending magnets inductance and K_m is the regulation coefficient. The simplified model of the magnetic field regulation is shown in Fig. 1.4.

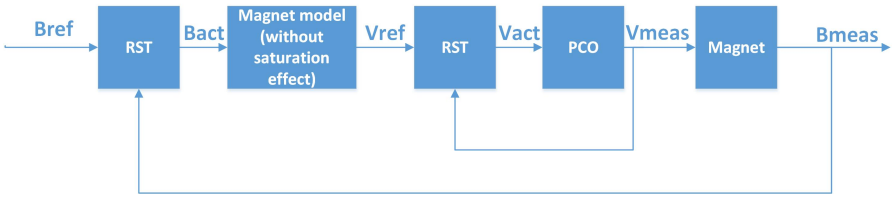

Figure 1.4 – Simplified bloc diagram of the power converter regulation system composed of a voltage R-S-T regulator stage, embedded in the field R-S-T regulator.

1.5.1 Electronics and control

The real time magnetic field measurement system needs electronics for the sensors conditioning, the remote control, and the distribution to a coherent magnetic field signal for the users. This electronics called "FIRESTORM" has five main functions listed below and illustrated in block diagrams in Fig.1.5

- Condition of the field sensors
- Reception and distribution of the CERN central timing events
- Computation the magnetic field $B(t)$
- Distribution of the real time magnetic field to the users

[2] Usually, the electro-magnets are regulated in electrical current .

- Communication to the CERN Control System. The B-Train receives the settings, provides the status, the alarms, and the diagnostics information.

The electronics and its performance is detailed in the Ref. [39].

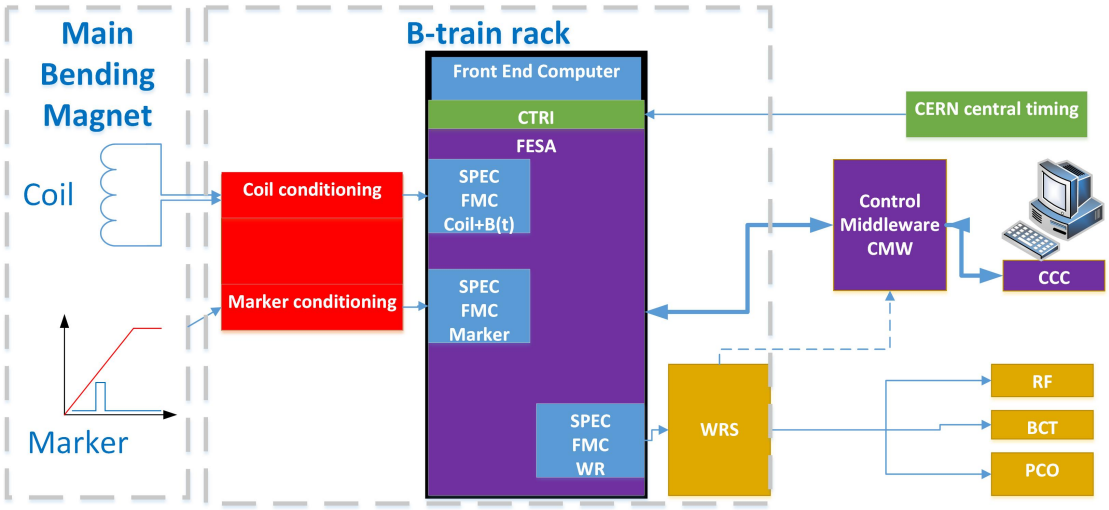

Figure 1.5 – B-Train electronics layout. The red blocks are the sensor conditioning parts, the green blocks are the timing parts, the blue blocks are the field computation parts, the orange blocks are the White Rabbit transmission (via optical fibers) to the users and the purple blocks are remote control and diagnostic parts.

1.5.2 Induction coil sensor

The B-Train system measures the field variation with induction coils as shown in Eq. (1.5). The design, fabrication, and calibration are detailed in the Ref. [40]. Its sensing principle is based on the Faraday-Lens law given by

$$U = -\frac{d\Phi(t)}{dt} \tag{1.9}$$

where U is the induced voltage when a magnetic flux $\Phi(t)$ varies with time. Hence, the magnetic flux variation is determined by integrating the induced voltage over time written as

$$\Phi(t) = -\int U dt. \tag{1.10}$$

The magnetic flux density variation is written as

$$\Delta B(t) = -\frac{\Phi(t)}{K} \tag{1.11}$$

where K is the closed surface. For an induction coil $K = K_c$ and $U = V_c$ (in the Eq. 1.5) and shall be known with an uncertainty of 10^{-4}. The induction coil must be operated in two conditions

- The coil is displaced in a fixed field,
- The coil is fixed, the field is varying with time (B-Train case).

1.5.3 Field marker sensor

The B-Train system measures the integration constant B_{m} (in the Eq. 1.5) field markers. As previously introduced, typical field makers are the Hall probes [4, 41, 42], and the NMR probes [43, 44, 45, 46]. They have advantages and drawbacks [47, 48, 49, 50] but for special applications requiring fast time-response, high accuracy and field gradient insensitive, the only known sensor was the peaking strips [51, 52].
In the 1990's, Dr. F. Caspers proposed to adapt the YIG filter principle based on FMR [53, 54] to measure the magnetic field in pulsed magnets. This sensor was tested on the PS accelerator. Almost twenty years later, following the approval of the consolidation program for the LHC's injectors, a complete review of the electronics and sensors was launched. The limitations of the peaking strips and its quasi-impossibility to re-manufacture, we came to the conclusion of using the FMR.
While the YIG filters are commercial products, several adaptations are required to be used as field marker. Only one firm provide these adaptations with several limitations (field-frequency range, size and packaging). A prototype of this version was tested in the PS [55, 56] from 2015 to 2018. Considering long-term maintainability constrains, we decided to develop in-house ESR markers.

Two key parameters shall be considered, that are the resolution and the reproducibility .
The resolution (in T/Hz$^{1/2}$) is the smallest measurable variation of the magnetic field written as

$$\Xi = \frac{n}{\delta} \tag{1.12}$$

where n is the noise spectral density, and δ is the sensitivity (the transfer function of the transducer) either in V/T for amplitude detection or in Hz/T for frequency detection. In this work, we refer also to the integrated resolution $\xi = \Xi\sqrt{\Delta f}$ where Δf is the equivalent noise bandwidth (ENBW).
The reproducibility (in T) is the cycle-to-cycle variation of the marker field value. The reproducibility is computed from the standard deviation of the reference magnetic field B_{r} at the marker trigger given by

$$\sigma_{B_{\mathrm{m}}} = \sqrt{\frac{1}{\mathrm{J}-1}\sum_{j=1}^{\mathrm{J}}(B_{\mathrm{r}_j} - \bar{B}_{\mathrm{r}})^2} \tag{1.13}$$

where J is the cycle count. B_{r} is determined either (i) by another characterized marker, typically by an NMR probe (ii) by the rest field measured in DC (iii) by the trigger time if the magnetic cycles of the machine are identical or (iv) by the beam radial position, in that case, the momentum of the beam must be very well known. In this work, we also refer to the relative reproducibility with respect to the field at beam injection B_{i} value, that is, $\sigma_B = \sigma_{B_{\mathrm{m}}}/B_{\mathrm{i}}$.
The field reproducibility includes all the uncertainties from the sensor itself, the conditioning electronics, the magnet, the power converter and the mechanics. This is a fundamental criteria for the beam operation. The entire accelerator operation is impacted in case of field jumps or field drift. The consequences are beam loss or path distortion [14].

The markers have strict tolerances to ensure the correct measurement of the field by the B-Train system as shown in Tab. 1.1.

Table 1.1 – Marker requirements.

Parameters	Value
Sensor size (mm × mm × mm)	$<30 \times 30 \times 30$
Minimum field (mT)	30
Maximum field (mT)	700
Field ramp rate (T/s)	<5
Field gradient (T/m)	<1.2
Field inhomogeneity G/B_{m} (m^{-1})	<10
Field resolution ($\mathrm{nT/Hz}^{1/2}$)	<10
Field reproducibility (-)	$<2 \times 10^{-4}$
Field accuracy (-)	$<1 \times 10^{-3}$
Maximum allowed downtime (hour/year)	<2
Required lifetime (years)	>20

To fulfill the requirements, a family of six marker sensors were developed and detailed in this work. Their performances are summarised in Appendix A.

2 Electron Spin Resonance

Methods based on ESR, also known as EPR phenomenon are powerful spectroscopic tools used in material science, physics, chemistry, biology, and medicine [57, 58]. Magnetometers based on the EPR phenomenon have been also proposed, essentially as an alternative to NMR and dynamic nuclear polarization (DNP-NMR) magnetometers at low magnetic fields [59, 60, 61, 62, 63, 64, 65]. The difficulty of ESR is its higher operating frequency because the gyromagnetic ratio of the electron is 28 GHz/T comparing to 0.042 GHz/T for the NMR with the hydrogen (about 670 times lower). For example, considering a field of about 1 T, the excitation frequency is in the VHF-band for the NMR while it is in the K-band[1] for the ESR. The source and detection elements are drastically different and required a very careful design for the ESR. Despite their lower absolute accuracy, EPR magnetometers have the advantage to allow for the use of smaller sample volumes for the same magnetic field resolution and, hence, are more indicated to operate in magnetic fields with strong gradients. Additionally, the EPR relaxation times are typically several orders of magnitude shorter than NMR relaxation times, facilitating the measurements in fast-changing magnetic fields which counterbalance the main drawback linked to the higher gyromagnetic ratio.

2.1 Electron paramagnetic resonance

In the following, we review in a simplified form the theory behind EPR. Electrons possess an intrinsic angular momentum that is quantized along any given direction, and is expressed by their spin $S = \pm\frac{1}{2}\hbar$, where $\hbar = \frac{h}{2\pi} = 1.054571817 \times 10^{-34}$ Js is the reduced Planck constant. In the classical view, a spinning electrical charge would give rise to a magnetic field. Analogously, in the quantum view an electron has an intrinsic magnetic moment given by

$$M = \gamma_e S = \pm\frac{1}{2} g_e \mu_B, \tag{2.1}$$

[1] According to IEEE standard

where $\gamma_e = \frac{g_e e}{2m_e}$ is the gyromagnetic ratio, e is the elementary electric charge and m_e is the electron rest mass. The g-factor is a constant that can be evaluated from quantum electrodynamics or measured. $\mu_B = \frac{e\hbar}{2m_e}$ is the Bohr magneton. For a free electron, $\mu_B = 9.2740100783(28) \times 10^{-24}$ J/T, $g_e = -2.00231930436256(35)$ [66] and the gyromagnetic ratio can be expressed in units of frequency, rather than angular velocity, written as

$$\frac{\gamma_e}{2\pi} = \frac{1}{2\pi}|g_e|\frac{\mu_B}{\hbar} = 28.0249514242(85) \text{ GHz/T} \tag{2.2}$$

The ESR manifests when the electron interacts with a uniform background magnetic field $\mathbf{B}_0$. In the classical view, the vector product of the magnetic moment $\mathbf{M}$ and the field gives rise to a torque that causes the electron to precess, as represented schematically in Fig. 2.1, according to the equation of motion:

$$\frac{1}{\gamma_e}\frac{d\mathbf{M}}{dt} = \mathbf{M} \times \mathbf{B}_0 \tag{2.3}$$

Precession occurs with an angular velocity Ω_0 such that:

$$\left\| \frac{d\mathbf{M}}{dt} \right\| = M\Omega_0 sin\theta = \gamma_e M B_0 sin\theta \tag{2.4}$$

where θ is the angle between the magnetic moment and the background field. The corresponding Larmor frequency is given by

$$f_0 = \frac{\Omega_0}{2\pi} = \frac{\gamma_e}{2\pi}B_0 \tag{2.5}$$

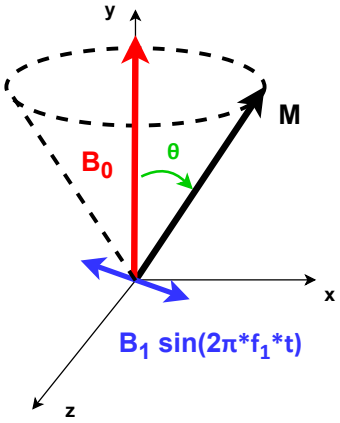

Figure 2.1 – Magnetic resonance motion diagram.

Let us now consider what happens when the sample is irradiated with microwaves at frequency f_1, so that the RF excitation field B_1 is orthogonal to B_0 as shown in Fig. 2.1. The B_1 field is typically from 1 to 100 μT, that is much smaller than the background. At resonance, when

$f_1 = f_0$, the precession axis of **M** coincides with the xz-plane ($\theta = 90°$), which results in the periodic change of sign of the component of the magnetization parallel to the background field. This inversion is closely analogous to the quantum mechanical description of the phenomenon. In the quantum view, the interaction between electron and magnetic field is expressed by the potential energy E associated with the torque, that is, $-MB_0$, which takes opposite values in the two spin states, as shown in Fig. 2.2:

$$E_{\pm\frac{1}{2}} = \mp\frac{1}{2} g_e \mu_B B_0 \tag{2.6}$$

In the case of a material sample immersed in the background field, at any given time the population of unpaired electrons will be roughly split in half between the two spin polarities. In fact, there is a slight excess of electrons at the lowest energy level, corresponding to the spin being parallel to the field, which decreases with the temperature and gives rise to a net macroscopic magnetization of the sample (paramagnetic effect). The energy difference between the two states is proportional to the frequency f_0 of the photons that are absorbed or re-emitted, causing the spin to flip in the opposite direction, according to:

$$\Delta E = g_e \mu_B B_0 = \gamma_e \hbar B_0 = h f_0 \tag{2.7}$$

The transition energy ΔE is proportional to B_0, leading to an increasing absorption signal amplitude. As a result, for a identical spin density and sample volume, the sensitivity is improved by applying stronger magnetic field, which is widely exploited in magnetic resonance imaging and spectroscopy [67, 68, 69].

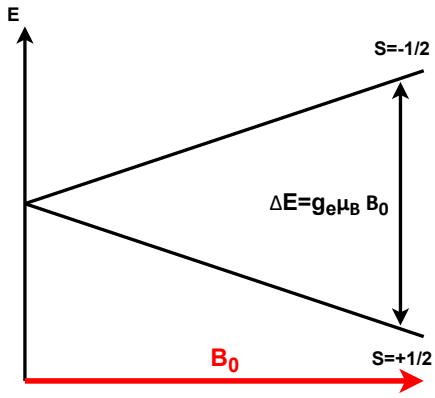

Figure 2.2 – Spin states functions of B_0.

The resonance mechanism described above also applies to NMR. For an isolated proton (^{1}H), the magnetic moment is given by the nuclear magneton $\mu_N = 5.0507837461(15) \times 10^{-27}$J/T, while the g-factor is about 5.6, leading to a gyromagnetic factor $\gamma_p/2\pi = 42.577478518(18)$ MHz/T [66]. This value varies for the protons in the nuclei of different chemical species. In this case, for the same background field, resonant frequencies are almost three orders of magnitude

lower than for ESR, which makes NMR easier in practice for very high field magnetometry applications.

2.2 Ferrimagnetic resonance

Ferrimagnetic resonance [70, 71] is also based on the electron spin, however ferrimagnetic (i.e, two unequal population of atoms with anti-parallel magnetic moments) or ferromagnetic (i.e., one population of atoms with parallel magnetic moments) materials introduce anisotropy terms into Eq. 2.5. The frequency f_0 is expressed by Kittel's formula [72] for an ellipsoid sample, adapted by Okamura [73] assuming that the relative permeability $\mu_r = 1$ due to the material being fully saturated and operating at gigahertz frequency [74, 75, 76], so that $B_0 = H_0/\mu_0$:

$$f_0 = \frac{\gamma_e}{2\pi}(B_0 + B_a - (N_z - N_t)\mu_0 M_s) \tag{2.8}$$

where N_t is the transverse demagnetizing factor, N_z is the axial demagnetizing factor, B_a the crystal anisotropy field and M_s the saturation magnetization, which is material dependent. Magnetic resonance cannot be established accurately [77, 78] when the material is not fully saturated, therefore the FMR must be operated above this threshold (i.e., $B_m > \mu_0 M_s$) for the field markers application.

In case of a sphere, where $N_t = N_z$:

$$f_0 = \frac{\gamma_e}{2\pi}(B_0 + B_a) \tag{2.9}$$

FMR is widely used in commercial RF devices such as circulators and insulators [79, 80], as well as in tunable filters [81, 82], resonators [83] and oscillators [84] in spectrum and vector network analysers. FMR has the relevant advantages of been highly selective (high quality factor, low insertion and return losses) and tunable. The use of FMR in magnetometer is reported in Ref. [85].

2.3 Magnetic resonance materials

2.3.1 Yttrium iron garnet (YIG and GaYIG)

The commonly ferrimagnetic material used in RF is the Yttrium iron garnet YIG ($Y_3Fe_5O_{12}$) in its pure formulation or doped with various elements such as Lithium, Aluminium, Gadolinium, Magnesium in mono and poly-crystalline forms. A non-exhaustive list can be found in J. Nicolas's book [77]. The doping elements allow reducing the magnetization saturation $\mu_0 M_s$ from 178 mT for pure-YIG down to about 20 mT for highly doped YIG. In this work we used Gallium doped GaYIG ($Ga_xY_3Fe_5O_{12}$), where x corresponds to the doped fraction of the material. YIG and GaYIG have a cubic crystal structure with three types of crystal axes the ⟨100⟩, the ⟨110⟩ and the ⟨111⟩ [78]. The direction of B_0 with respect to the crystal axes changes

$\gamma/2\pi$ through B_a. YIG can be produced in a thin layer, or in a sphere by grinding and polishing processes. In this work, we used spheres of 0.3 mm diameter by Ferrisphere Inc. (USA). The sphere is mounted on an aluminium oxide ceramic rod (Alumina Al_2O_3) and aligned on the ⟨110⟩ crystal axis (in Fig. 2.3). The specific alignment method used by the manufacturer is not disclosed but a well-known process is reported in the Refs. [86, 87, 88].

From Eq. (2.9), B_a can be canceled out if the crystal structure of the YIG sphere is rotated around its ⟨110⟩ axis, considering the B_0 orthogonal and formulated as

$$B_a = -\left(2 - \frac{5}{2}\sin^2\alpha - \frac{15}{8}\sin^2 2\alpha\right)\frac{K_1}{M_s}\mu_0 \tag{2.10}$$

where α is the angle between B_0 and the ⟨100⟩ axis as shown in Fig. 2.3 and K_1/M_s is the first-order anisotropy field constant [89, 78] typically -3419 A/m for YIG and -4436 A/m for GaYIG [78]. By orienting the YIG sphere to $\alpha = \pm 29.7\,°$ [90, 91] (slightly lower value of $\alpha = \pm 27\,°$ can be found in the reference [78]) called "temperature stable axis", the Eq. (2.5) becomes valid for the FMR. Moreover, there is no more temperature dependency of the gyromagnetic ratio. For that reason, we developed a calibration bench described in Sec. 3.3 to perform the temperature stable axis alignment. However, the tuning process to reach the optimum angle is very difficult due to the stiffness the curve as presented in Fig. 2.4.

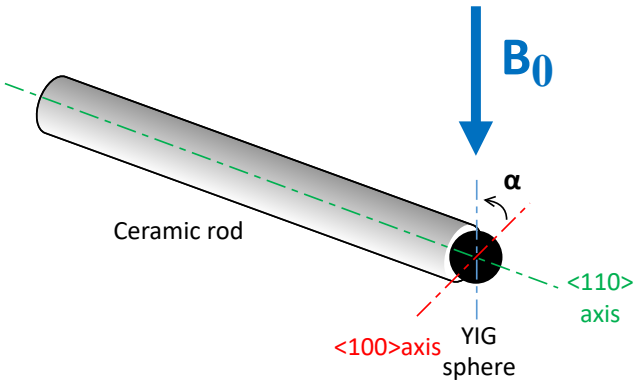

Figure 2.3 – Axis of YIG crystal mounted on the ceramic rod.

2.3.2 α,γ-bisdiphenylene-β-phenylallyl (BDPA)

For the paramagnetic sample we selected the organic free radical α,γ-bisdiphenylene-β-phenylallyl complex with benzene (BDPA, Merck 152560). This material is widely used as standard to characterize EPR spectrometers [93]. BDPA has a single narrow line of about 100 μT [94], a low g-factor anisotropy [95], and it is more chemically stable compared to other free radicals [96]. The spin density n_s of a single crystal of BDPA is about 1.5×10^{27} spin/m^3 [97], its effective gyromagnetic ratio $(\gamma_{BDPA}/2\pi) = 28.02048$ GHz/T computed from the reported g-factor of BDPA g_{BDPA} of 2.0020 [95], as $(\gamma/2\pi) = g_{BDPA}(\mu_B/\hbar)$. Its g-factor anisotropy Δg is less than 2.7×10^{-4} [98].

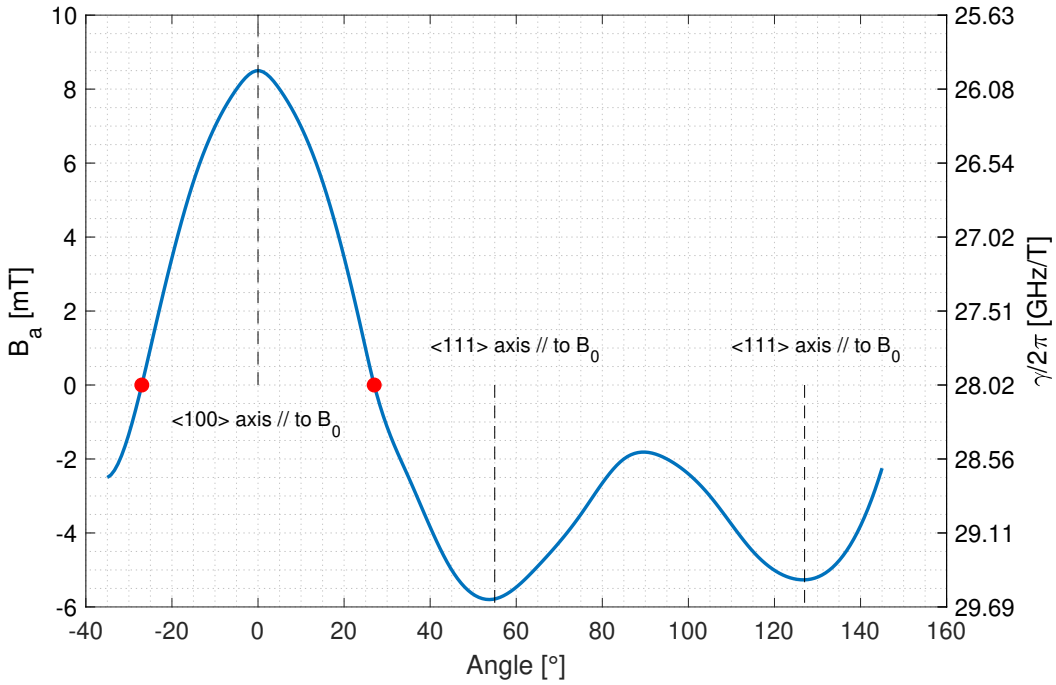

Figure 2.4 – B_a variation as a function of YIG sphere rotation around $\langle 110 \rangle$ axis with a fixed excitation frequency f_0. This curve is adapted from P. S. Carter [92, 78] and derived from Eq. (2.10). $B_a = 0$ mT (red markers) corresponds to the magnetic field at theoretical gyromagnetic ratio value of Eq. (2.2), that is, the temperature stable axis.

2.4 Magnetic resonance sensor design architectures

Different topologies can be used to measure the magnetic resonance. Three main architectures are commonly used:

- Resonator structure
- Oscillator structure
- Coupling structure

The first and the second architectures are especially well adapted for field markers, by their high sensitivity in a narrow operating band. They can be tunable around their working point, typically by tens of megahertz (few militesla). Both topologies are based on an LC circuit with an external source for the resonators, or internal source via additional cross-coupled transistors [99, 100] for the LC oscillators. At magnetic resonance, the ESR sample acts on the inductance value, which changes its impedance. The perturbed signal can be detected by the signal amplitude, the frequency, or the phase variation. In this work, we focus on the amplitude detection for the resonator detailed in Sec. 6.1 and on the frequency detection for the oscillator detailed in Sec. 8.4. We report a preliminary study with phase detection in the Appendix C.

The coupling structure is generally used for broadband devices. The typical application is the YIG filter [91, 101, 81, 102]. The magnetic resonance changes the coupling coefficient between two transmission lines, which implies the transmission of a portion of the input power to the output. This variation is detected in the same manner as detailed in Sec. 6.1.

Part II

Design and characterization of ESR sensors

3 Calibration benches

We performed the metrological characterization of the sensors with three dedicated test benches. The first system (detailed in Sec. 3.1) is used to measure the effective gyromagnetic ratio[1], the resolution, the temperature dependency, the field ramp rate $\dot{B} = dB/dt$, and the field direction. The second system (detailed in Sec. 3.2) is used to measure the dependency to the field gradient. Both benches provide a known background field as function of time (trapezoidal shape as shown in Fig. 1.3). The third system (detailed in Sec. 3.3) is used to align the YIG sphere to the temperature stable axis (i.e., Sec. 2.3.1).This bench provides a constant background field.

The magnetic resonance signal is detected with specific electronics, detailed in Sec. 6.1 for the FMR resonator sensors, in Sec. 7.2 for the EPR resonator sensors and in Sec. 8.4 for the EPR oscillator sensors.

The data acquisition (DAQ) is performed by a multifunction card (National Instruments™, USB-6366) with non-multiplexed analog-to-digital conversion at a maximum speed of 2 MS/s and 16 bit. We developed a LabVIEW™ based software running on a National Instruments™ PXI Controller (PXI-8119) to drive the different devices via GPIB, RS 232 and USB. Data analysis is performed with Matlab™.

3.1 Dipole bench

The dipole bench (in Fig. 3.1) is composed of a dipole electromagnet producing a nominal dipolar field of about 0.4 T for 450 A in an aperture of 100 mm. The current is supplied by an AC/DC power converter with current regulation and measured by an internal direct current current transformer (DCCT) with an accuracy of ±10 ppm. A second power converter with

[1] We computed the effective gyromagnetic ratio from NMR measurement at the rest field combine with an induction coil for the time-transient field. The overall uncertainty on the magnetic field is 380 ppm by considering the homogeneity of the magnet in the sensor volume of ±350 ppm, the accuracy of the NMR of ±5 ppm, the accuracy of the induction of ±100 ppm and the eddy current contribution of about ±100 ppm. Therefore the uncertainty on the gyromagnetic ratio is about ±0.01 GHz/T.

higher current and voltage capability is used to reach nominal field of 0.8 T for 900 A and ramp rates up to 5 T/s, in particular, for the 710 mT EPR sensor characterisation.
The field measurement device consist of an NMR probe to measure the rest field and an induction coil to measure the field variation. The ESR sensors are installed in the center of the magnet in between the NMR and the coil. In this configuration, the field error due to the intrinsic non-uniformity of the magnet is minimized (3.5×10^{-4} in the sensors volume region).

Additional modular elements can be installed, including a Peltier unit [103] to measure the temperature dependency and a Theta-Phi-Goniometer to measure the effect of the field direction.
The Peltier module is used to cool and heat the sensor in its operation range 17-35 °C and installed inside the magnet aperture with non-ferromagnetic equipment. Moreover, the Peltier element and its thermal insulation box are very compact and cost-efficient compared to standard temperature controlled systems. A fan outside the magnet is connected to the system via a flexible pipe, which blows ambient air to cool-down the heat sink fixed on the Peltier element. The heat sink was chosen to maximize the thermal exchange surface, while minimizing the eddy currents effect caused by the B_0 field variation. The Lorentz force induced by the DC current supply of the Peltier module can be considered negligible.
The goniometer element is placed outside the magnet and the sensor is installed at the end of a T-shaped arm. This arm is fixed to the goniometer with a counterweight to minimize the torque on the element. Two angular directions are possible: the pitch angle ϕ corresponding to the rotation around the x-axis and the roll angle ψ corresponding to the rotation around the z-axis. The overall angular range is $\pm 15°$ with a adjustment sensitivity of 0.1°. The third angular direction is the yaw angle κ corresponding to the rotation around the y-axis. The sensor is only rotated by 180° around the yaw angle.

The summary of the equipment is shown in Tab. 3.1.

Table 3.1 – Dipole calibration bench components.

Components	Manufacturer	Model
Magnet	SIGMAPHI	PXMBHDCHWP-SP000002 (MBL16)
Power converter #1	TRANSTECHNIK	LHC600A/40V
Power converter #2 [1]	CERN	COMET 4P 1000A/120V
NMR teslameter	Metrolab	PT2025
NMR probe	Metrolab	1062 type #1 and #3
Induction coil	CERN	40 mm × 40 mm 700 turns (0.94456 m^2)
Peltier module	MULTICOMP	38.1 W 30 mm × 30 mm × 3.6 mm MCPE-127-10-13
heat sink	Fischer Elektronik	40 mm × 40 mm × 20 mm ICK S 40x40x20
Peltier controler	Laird Technologies	PR-59
Peltier insulation box	CERN	90 mm × 70 mm × 55 mm wall thickness of 5 mm in EPG 103
Theta-Phi-Goniometer	OWIS	±15° TP65-W30-W40
Mechanical supports	CERN	-

[1] Used for field ramp rate dependency measurements and for the 20 GHz oscillator that requires 0.8 T/900 A peak.

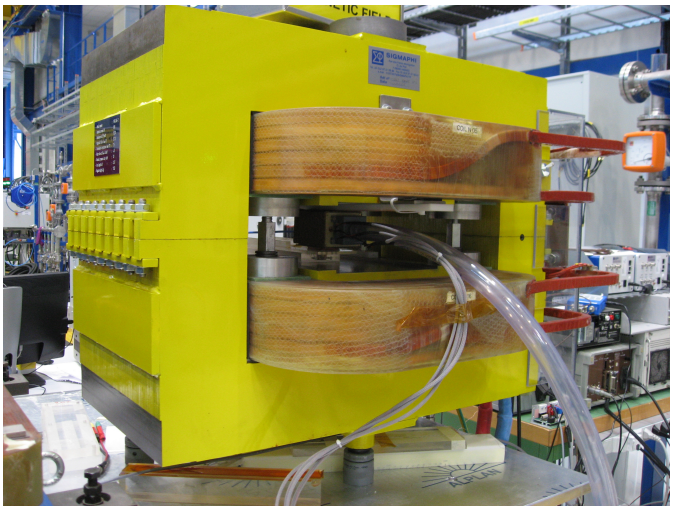

(a)

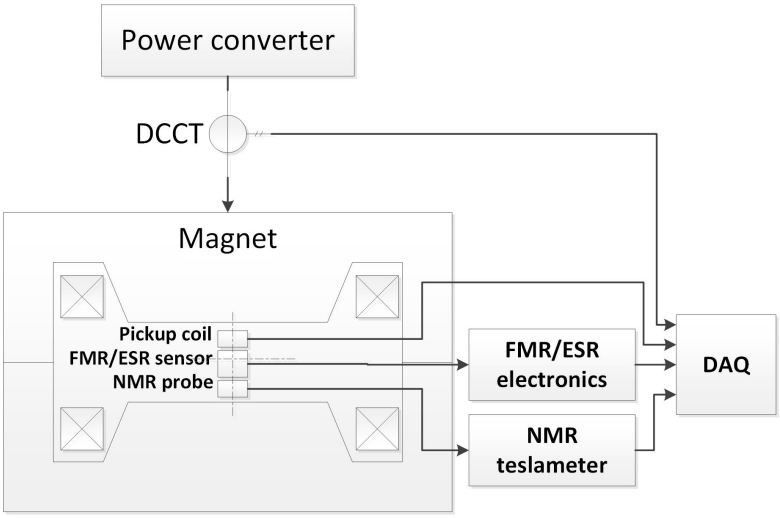

(b)

Figure 3.1 – Dipole calibration bench. (a) Dipole bench with the peltier module and its cooling system. (b) Dipole bench block diagram.

3.2 Quadrupole bench

The quadrupole bench (in Fig. 3.2) is composed of a quadrupole magnet[2] producing a main field gradient of about 7.2 T/m for 400 A in a aperture diameter of 120 mm. The current is supplied by a AC/DC power converter with current regulation. For the 710 mT sensor, the magnet has to be operated in the saturated regime of the magnet to reach the marker value. Therefore, to reach a field marker of 710 mT the quadrupole has to be operated at 900 A producing a gradient of about 12 T/m.
The field measurement devices consist of two induction coils spaced by 10 mm measuring the gradient variation. The sensors (coils and ESR sensor) are positioned on the vertical symmetry plane of the magnet. Thus, the sensors are sensitive only to one component of the gradient (i.e., $\partial B_x/\partial y$). The orientation of the sensor is in the same polarity as the PS and LEIR gradients detailed in Chapter 9 and 10. The vertical position with respect to the magnetic centre of the quadrupole, where the field is zero, determines the ratio of the gradient over the marker field level. The ratio is 4.6 m^{-1} for the PS and 10 m^{-1} for LEIR. The summary of the equipment is shown in Tab.3.2.

Table 3.2 – Quadrupole calibration bench components.

Components	Manufacturer	Model
Magnet#1 [a]	CEM	PXMQNFINWP-00000016 (ACOL QN 016)
Magnet#2	BBC	PXMQNETNWP-B2000152 (LEP main quad)
Power converter#1	CERN	COMET 2P 500A/120V
Power converter#2 [b]	CERN	COMET 4P 1000A/120V
Induction coil #1	CERN	6B 42mmx10mm 330 turns (0.13085 m^2)
Induction coil #2	CERN	8B 42mmx10mm 330 turns (0.13032 m^2)
Mechanical supports	CERN	-

[a] Used for the FMR resonators.
[b] For the 20 GHz oscillator that requires higher field dynamic range.

[2] Due to availability, we used another quadrupole for the FMR sensors with lower gradient of 2 T/m for 500 A and a aperture diameter of 386 mm

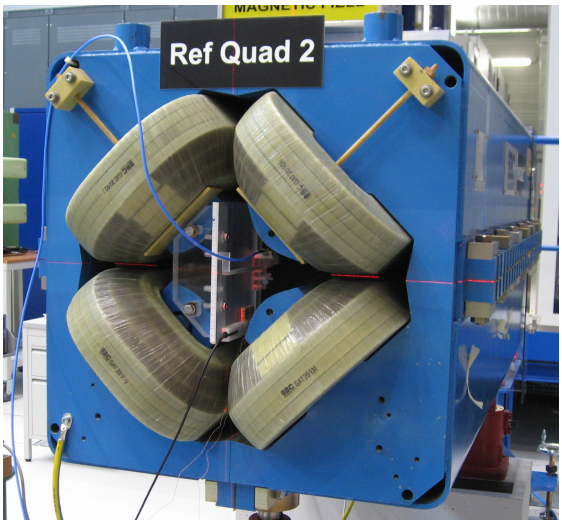

(a)

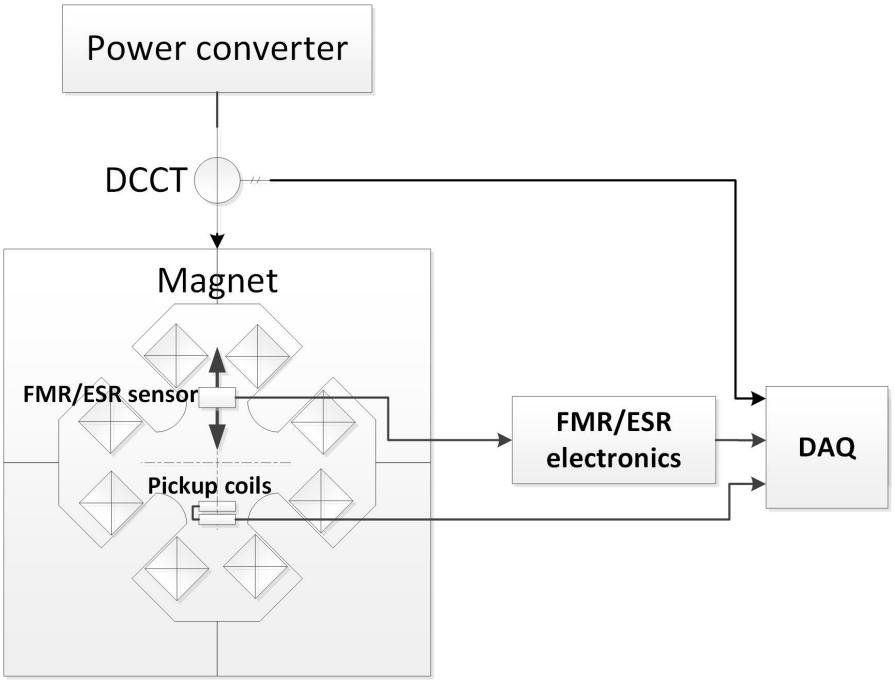

(b)

Figure 3.2 – Quadrupole calibration bench. (a) Quadrupole bench picture with magnet#2. (b) Quadrupole bench block diagram.

3.3 Stable axis adjustment bench

As previously introduced in Sec. 2.3.1, the GaYIG sphere must be aligned to the temperature stable axis. We setup a bench (in Fig.3.3) with an C-shape skew electro-magnet producing a DC horizontal dipolar field. We machined a dedicated support to ensure the positioning of the sensor in an uniform field region (better than $\pm 6 \times 10^{-3}$/mm). The support is placed near the aperture ends for an hand access to the sphere rod.
The bench is equipped with a Hall probe measuring the field next to the sensor. The GaYIG spheres is heated with a heating gun. The maximum temperature is set to 60 °C. The magnetic resonance is measured with a Vector Network Analyser (VNA). We adjusted the sphere orientation using its ceramic rod equipped with a brass sleeve. We used non-feromagnetic tools (ceramic and titanium) to not change the magnetic resonance point during the adjustment process. The summary of the equipment is shown in Tab.3.3.

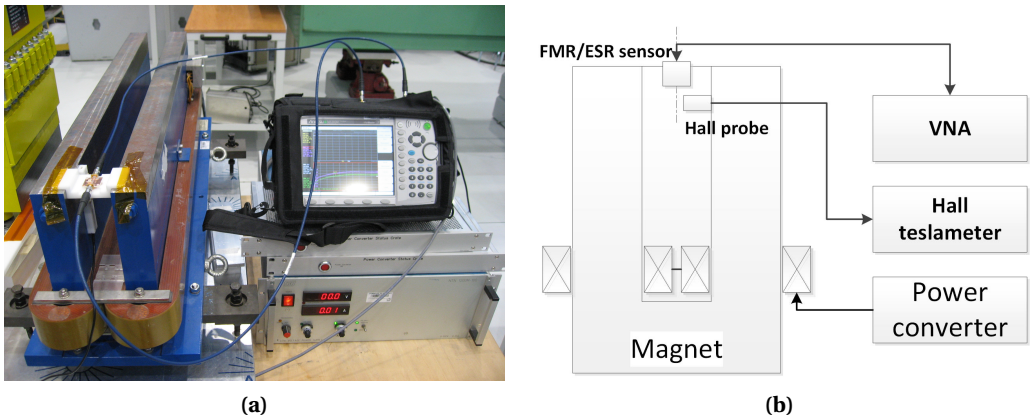

(a) (b)

Figure 3.3 – Stable axis adjustment bench.(a) Bench picture.(b) Bench block diagram.

Table 3.3 – Stable axis adjustment bench components.

Components	Manufacturer	Model
Magnet	OSWALD	HCMMWDRCAP-00900120 (MDR)
Power converter	FUG	NTN 1200M-100
VNA 5 kHz-6 GHz	Anritsu	MS2026C
Heat gun	Triac	set to max. 60°C
Mechanical supports	CERN	-

4 Design of the 1 GHz resonator structure

4.1 Base design

The resonant-circuit at 1 GHz for the 36 mT sensor is based on a fixed LC circuit with lumped elements. We privileged this choice with respect to a planar waveguide for size reasons. The minimum size required for a planar waveguide would be a 75 mm long strip (considering a $\lambda/4$ resonator as detailed in Section 5.1).

The resonator elements ($L1$, $R1$, $C1$, $C2$ and $C3$ in Fig. 4.1) are selected to obtain the desired resonance frequency f_{res} and a load impedance matched to Z_0=50 Ω at resonance. The parasitic elements (L_{p} and R_{p}) take into account the parasitic effects of the connections. We selected the matching-circuit, as shown in Fig.4.1 to have only capacitors, to avoid inductances interacting with the field, and because the resistance of the load is lower than Z_0[104]. The role of $C3$ is to increase the capacitor value $C2$ compared to the typical NMR matching and tuning circuit (having only the capacitors $C1$ and $C2$). The operating frequency and the resistance of the coil would require a capacitor $C2$ having a value below 0.5 pF (thus similar to the estimated parasitics). This circuit design uses standard capacitance values in the picofarad range and provides flexibility to fine-tune the resonance frequency.

The capacitors are surface mounted devices (SMD), standard size 0402. The inductor is a single-turn planar coil of inductance $L1$ and series resistance $R1$, having an internal diameter of 0.6 mm (i.e., sufficiently large to accommodate the YIG sphere or a BDPA crystal). We used the ANSYS Electronics Desktop™ simulation tool to optimize the layout, in particular the HFSS™ Finite Element (FE) simulation module for the planar coil parameters, and the Circuit Design and Simplorer modules for the lumped elements. In this way we adjusted the parasitic elements to match the resonance frequency as measured in Fig. 4.2. The layout and the elements values are given in Fig. 4.1 and Table 4.1.

We performed the routing of the board to minimize the size of the sensor, minimize the eddy currents effect due to the time-transient field, and to allow the installation of the ESR sample.

This chapter is reproduced with changes from [7], with the permission of AIP Publishing.

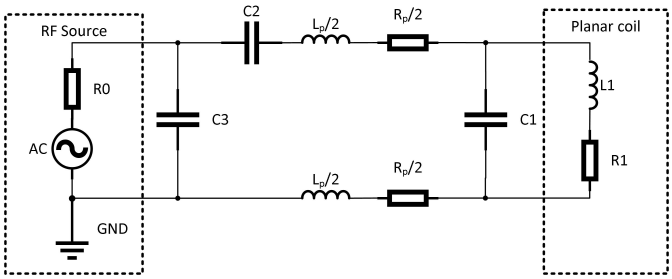

Figure 4.1 – Schematics of the 1 GHz resonator L_p and R_p are the parasitics elements.

Table 4.1 – Element values for the 1 GHz resonator.

Elements	Simulation value	Measured value
Substrate type	Rogers RO4350 B	
Tuning circuit $C1$ (pF)	4.7	
Matching circuit $C2$ (pF)	4.7	
Matching circuit $C3$ (pF)	15	
$L1$ (nH)	1.2	-
$R1$ at 1 GHz (mΩ)	38	-
f_{res} (MHz)	1109	
S_{11} (dB)	-19	
Q at -3 dB (-)	14	36
L_p (nH)	4.13	-
R_p (Ω)	1.35	-

In case of the FMR, the YIG sphere (mounted on a ceramic rod as detailed in Sec. 2.3.1), which is raised up by 0.55 mm with respect to the substrate to avoid strong coupling [105]. All the parts (connectors, PCB plated layers, capacitors, YIG fixation elements) were carefully selected and tested to be non-ferromagnetic. The sensor is shown in Fig. 4.3. We measured a variation if the resonator frequency after the pre-series production, this is attributed the manufacturing tolerances of the capacitor values. In order to use this sensor type in the B-train system, we performed a sorting of the produced resonators to select the devices that have resonant frequency values within 28 MHz (1 mT). This approach allows having interchangeable spare parts without changing the main B-train parameter settings.

4.2 Upgrade design

We did not change the RF resonator structure part as very good results were obtained. However, in order to be more precisely positioned and standardized with respect to the other sensors, minor modifications were implemented only on the mechanical function of it. With this upgrade, removal and replacement of the sensor by a spare piece is obvious. The improvements consist of replacement of two clearance holes, by one dowel hole and a oblong dowel hole of 2 mm diameter as shown in Fig. 4.4.

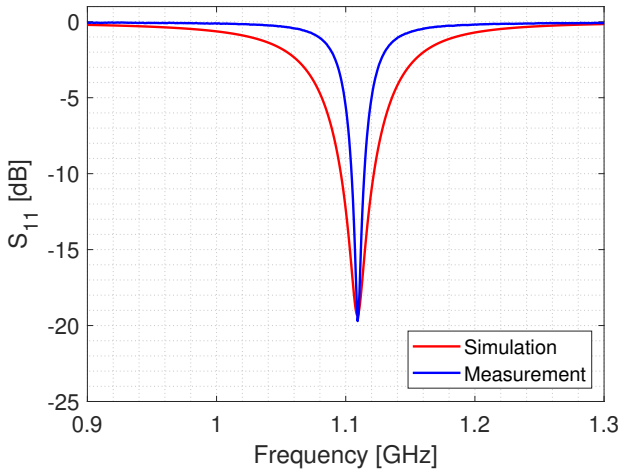

Figure 4.2 – Simulation versus measurement (1 GHz resonator).

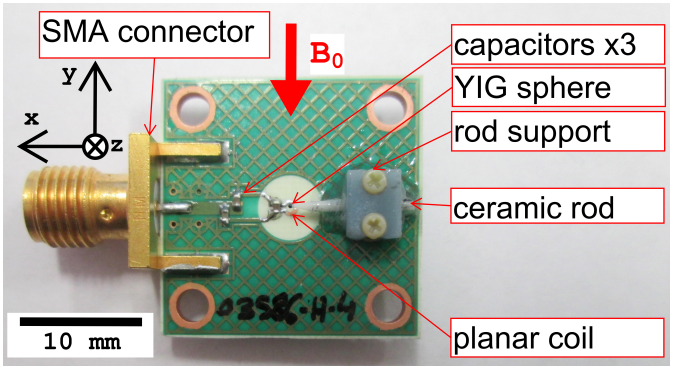

(a)

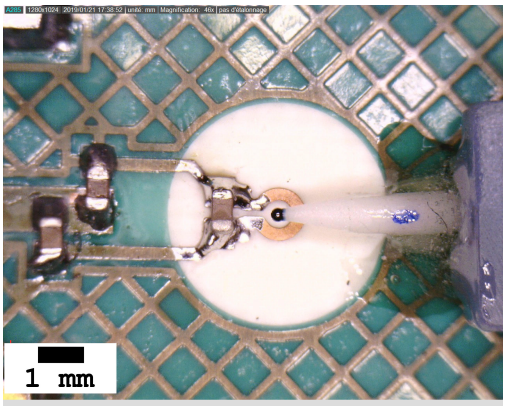

(b)

Figure 4.3 – 1 GHz resonator (with FMR GaYIG sample). (a) The resonator with the description of the elements. (b) The zoom-in of the mounted YIG sample area.

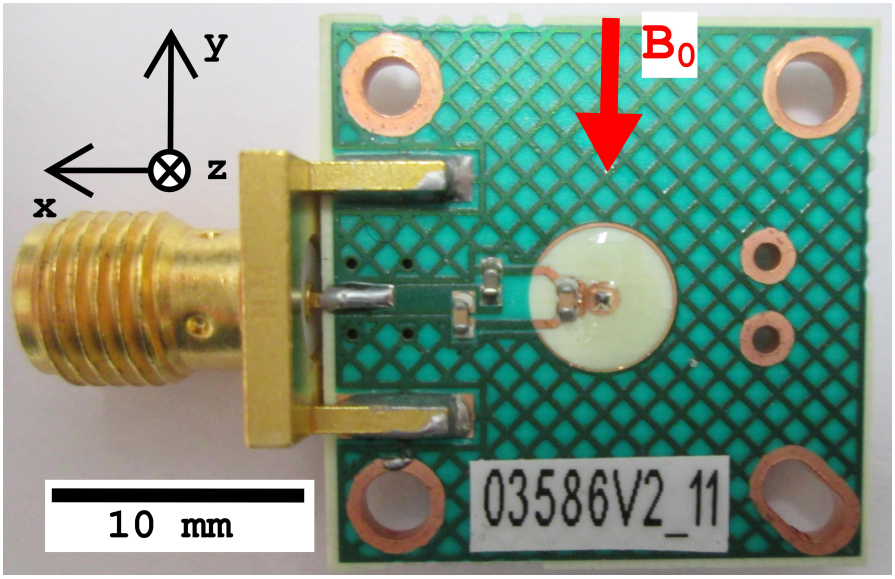

Figure 4.4 – 1 GHz resonator version 2 (with EPR BDPA sample).

5 Design of the 3 GHz resonator structure

5.1 Base design

The resonant-circuit at 3 GHz for the 106 mT sensor is based on a grounded coplanar waveguide (GCPW), which simplifies the inter-connection compared to striplines and microstrips. A quarter wavelength ($\lambda/4$) resonator reduces the size of the sensor with respect to a $\lambda/2$ resonator [106, 107]. The total length of the strip is 15.3 mm for 3 GHz.

To optimize the layout, as for the 36 mT sensor, we used the HFSS™ simulation tool with a complete 3D model of the waveguide to confirm the design parameters (see Tab. 5.1). We designed a full parametric model in view of future resonance frequency operating points. Due to the excitation field direction produced by the GCPW, the strip is rotated by 90° in order to have B_0 (parallel to y-axis) orthogonal to B_1 (parallel to x-axis) in the coordinate system as shown in Fig. 5.1a. Since sharp edges create discontinuities (parasitic capacitor and inductor) [107], the junction was simulated with a straight chamfer and optimized with an adapted mitres. The FMR sample is placed at the shorted end position of the trace (Fig. 5.1), while the ESR sample is placed at 2.4 mm from the shorted end (detailed in Sec. 5.2). The ground planes on the top and bottom layer are uninterrupted to ensure an optimal distribution of the electric (in Fig. 5.3a) and magnetic (in Fig. 5.3b) field lines.

The produced sensor performance differs from the design values by only 50 MHz in the resonance frequency and by 7.7 dB in the reflected power (see Tab. 5.1 and Fig. 5.2). The difference is attributed to the coaxial to GCPW junction and to the etching process. The repeatability over five produced sensors is ±1.5 MHz for the resonance frequency and ±2.7 dB for the matching.

This chapter is reproduced with changes from [7], with the permission of AIP Publishing.

Table 5.1 – Element values for the 3 GHz resonator.

Elements	Design value	Measured value
Substrate type	Rogers RO4350 B	
Strip width (mm)	2.1	
Strip clearance width (mm)	0.32	
Strip length (mm)	15.3	
Mitres (%)	70	
Open gap length (mm)	0.17	
f_{res} (MHz)	3110	3050
S_{11} (dB)	-31.7	-24.0
Q at -3 dB (-)	78	81

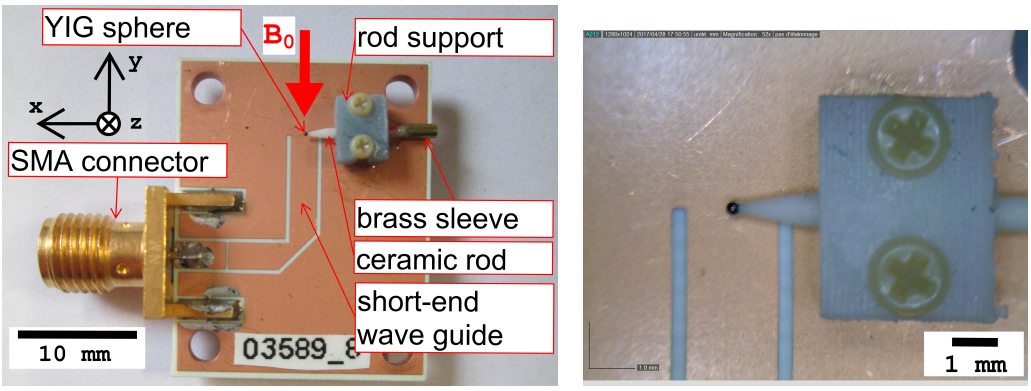

(a) **(b)**

Figure 5.1 – 3 GHz GCPW resonator mounted with GaYIG sample. (a) The GCPW with the description of the elements. (b) The zoom-in of the mounted YIG sample area.

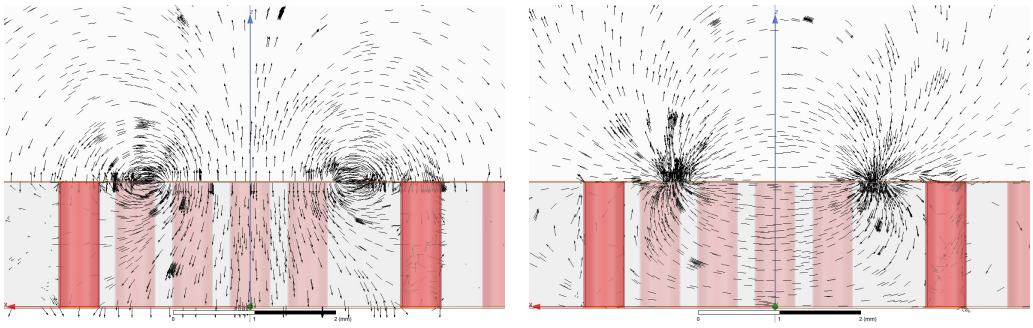

(a) **(b)**

Figure 5.3 – 3 GHz field lines on the resonator cross-section (xz-plane). (a) The E-field lines parallel to the z-axis at the center of the trace. (b) The B-field lines parallel to the x-axis at the center of the trace, i.e, B_{RF}.

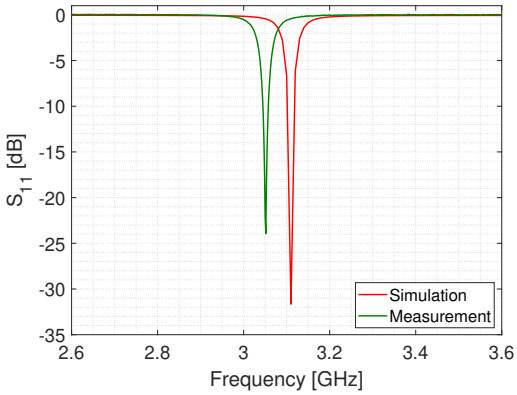

Figure 5.2 – Simulation versus measurement (3 GHz resonator).

5.2 Upgrade design

We designed a second version of the GCPW to suppress the effect of the ceramic rod fixation holes. After the tapping operation, we measured significant changes on the resonance frequency and on the matching. For better performance, we also suppressed higher order modes for the magnetic resonance and standardized the mechanical interface with respect to the sensor support.
The strip is slightly shorted by 50 μm, vias of 0.5 mm diameter are added all along the strip spaced by 1 mm. This second version of the resonator is shown in Sec.7.1 (Fig. 7.1d). The comparison between the simulation and the measurements are presented in Fig. 5.4a with a zoomed-in view in Fig. 5.4b.

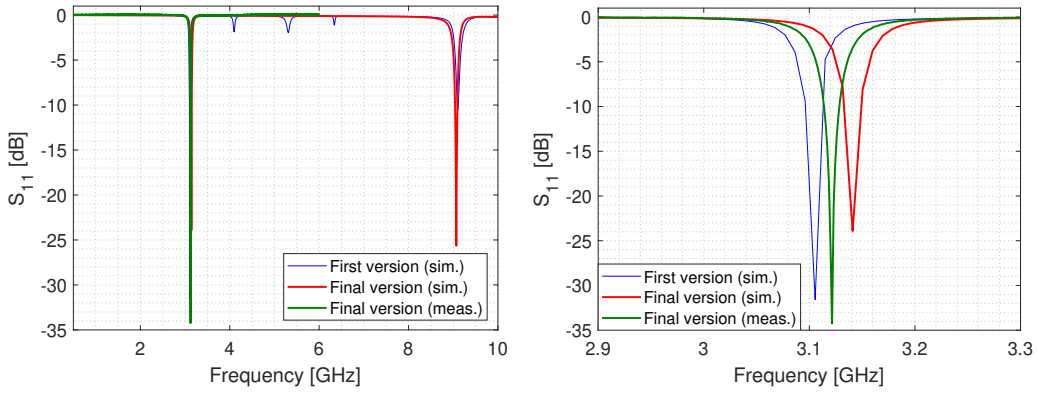

Figure 5.4 – Simulation S_{11} of the 3 GHz resonator version 1 and 2 (a) up to 10 GHz, only the $2f_{\text{res}}$ ($\lambda/2$) higher mode remains on the version 2. (b) Zoom-in from 2.9 to 3.3 GHz around f_{res}.

The resonance frequency is at 3.140 GHz with the return loss $S_{11} = -21.6$ dB, for a Q-factor $Q = 79$. The unwanted higher order modes at 4.05 GHz, 5.25 GHz and 6.30 GHz present in

the first version are suppressed by the vias. The normal higher mode at 9.07 GHz remains as shown in Fig.5.4a, which corresponds to a $\lambda/2$ GCPW resonator. This resonance can be used as a higher field marker at about 324 mT by placing the ESR sample at the middle of the trace length. In Table 5.2 we summarize the simulated and measured characteristics of the second version of the 3 GHz resonator.
The measured resonance frequency is lower by 18 MHz and the return loss are lower by -34 dB. These differences are attributed to the connector interface and etching process. The manufactured resonator is very close to the critical coupling as shown in Fig. 5.5, which then improves the matching. The minor rotation around the origin is due to the coaxial cable between the resonator and the VNA [108] (i.e., a phase shift).

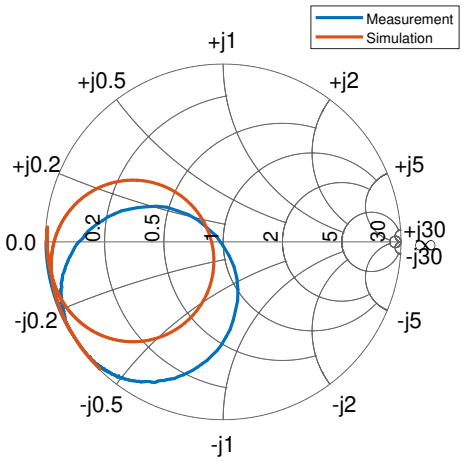

Figure 5.5 – Smith chart representation of the 3 GHz resonator. The red curve is the simulation while the blue curve is the measurement performed on the resonator used with BDPA sample.

Table 5.2 – Element values for the 3 GHz resonator version 2.

Elements	Design value	Measured value
Substrate type	Rogers RO4350 B	
Strip width (mm)	2.1	
Strip clearance width (mm)	0.32	
Strip length (mm)	15.25	
Mitres (%)	70	
Open gap length (mm)	0.17	
f_{res} (MHz)	3140	3122
S_{11} (dB)	-22	-34.25
Q at -3 dB (-)	79	70

We use this resonator version for the sensor with paramagnetic sample due to the aforementioned improved performance. The optimal position of the sample was determined from the HFSS™ model as shown in Fig. 5.6. This corresponds to $y = -2.4$ mm from the trace short-end, where the microwave magnetic field (H_{RF}) is the highest as shown in Fig. 5.7.

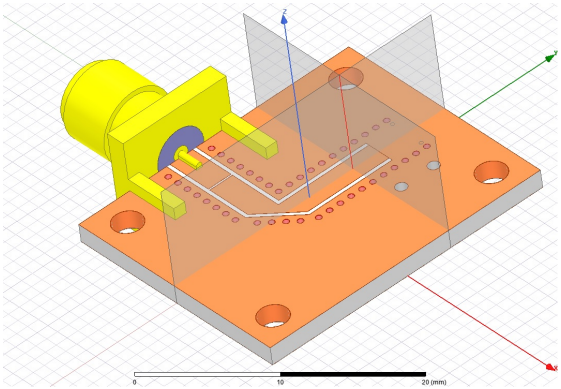

Figure 5.6 – HFSS™ model of the 3 GHz resonator where the coordinate system are shown. The xz-plane and yz-plane in semi-transparent grey are used to plot the magnetic field magnitude distribution (in Fig. 5.7), while the z-axis red line is used to plot the H_{RF} field (in Fig. 5.8) at the EPR sensor position.

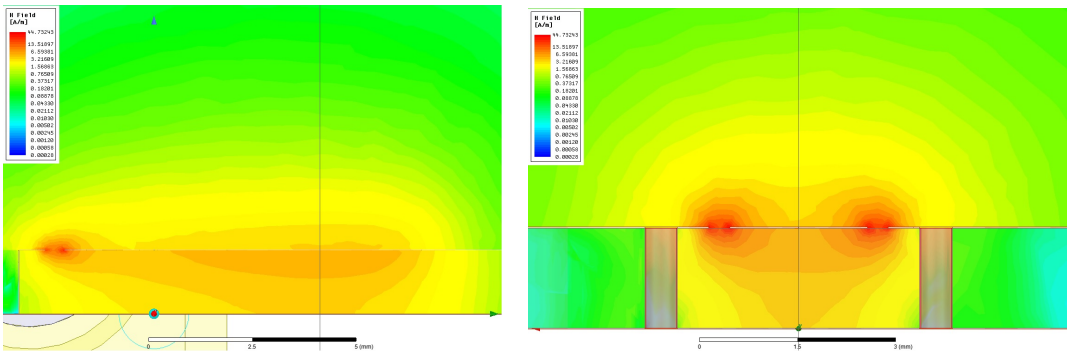

(a) **(b)**

Figure 5.7 – H_{RF} magnetic field magnitude distribution on the trace. (a) On the yz-plane. (b) On the xz-plane.

At $y = -2.4$ mm and $x = 0$ mm, the component of the magnetic field is mainly on the x-axis as shown in Fig.5.3b. The RF excitation field B_1 , in free space, is given by

$$B_1 = \frac{\mu_0 H_{RF}}{2} \tag{5.1}$$

Considering the input RF power at the resonator $P_w = -5.86$ dBm, the resulting H_{RF} along z-axis is shown in Fig. 5.8. At the vertical position of the EPR sample ($z = 0.14$ mm, above the top layer) $H_{RF} = 4$ A/m, hence $B_1 = 2.5\,\mu$T. This value is part of the noise and signal computation detailed in Sec. 7.3.

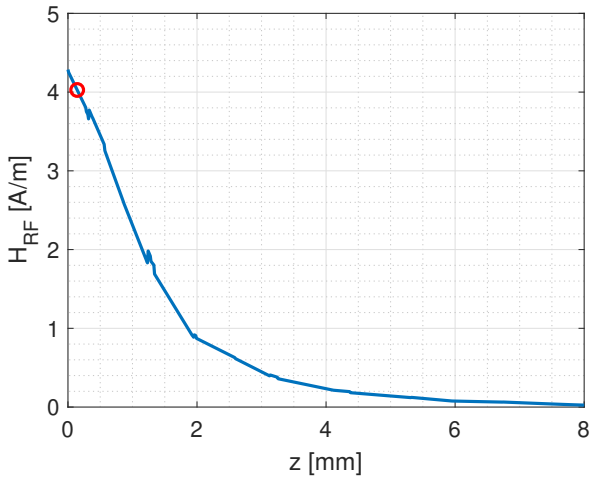

Figure 5.8 – H_{RF} magnetic field distribution on the z-axis. $z = 0$ mm is the top surface of the PCB. The red dot marker is the position of the EPR sample at $z = 0.143$ mm. The presence of glitches (as example at about $z = 1.25$ mm) are due to the simulation mesh size.

6 Characterisation of the FMR sensors

6.1 FMR resonator detection electronics

The magnetic resonance signal is detected by a 180 ° hybrid coupler, called "Magic-T" in some documentation, combined with a RF amplifier and a Schottky diode (see Fig. 6.1). The hybrid coupler is used as a comparator. When the sensor approximately matches 50 Ω, the output signal is minimized (limited by the coupler directivity). At magnetic resonance, the matching circuit is perturbed and a fraction of the input signal is transferred to the output of the hybrid coupler. This signal is amplified and the Schottky diode is used for the amplitude detector [109, 110], where the RF signal is converted into a low frequency (LF).The devices used for the detection are shown in Tab. 6.1.

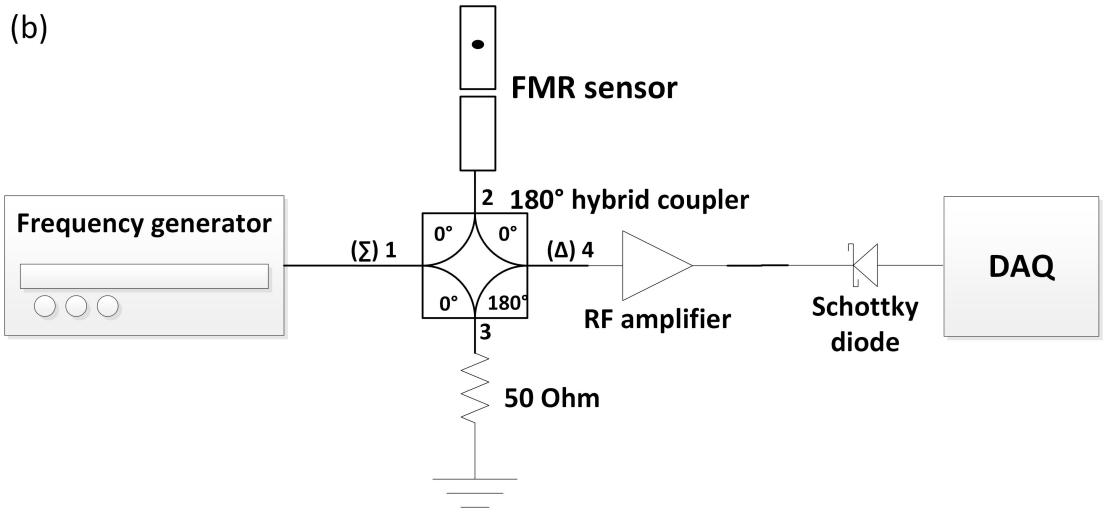

Figure 6.1 – FMR resonator detection electronics.

The detection electronics of the 106 mT FMR sensor is similar to the 36 mT FMR sensor shown in 6.1, we only change the hybrid coupler by an Anaren 30056 to operate in the sensor

This chapter is reproduced with changes from [7], with the permission of AIP Publishing.

Table 6.1 – FMR detection electronics components.

Components	Manufacturer	Model
Frequency Generator 0.01-6 GHz	TTi	TGR6000
Hybrid coupler 180° 1-2 GHz	Anaren	30055
Hybrid coupler 180° 2-4 GHz	Anaren	30056
50 Ω termination 0-12 GHz	Mini-Circuits	ANNE-50L+
RF amplifier 0.5-8 GHz gain 42 dB	Narda-MITEQ	AMF-4D-00500800-18-13P-HS-R
Schottky Diode	Agilent Technologies	8473B
DAQ	National Instruments	USB-6366

frequency range from 2 to 4 GHz.

6.2 Ramp rate effect

In order to determine the influence of ramp rate, we measured the position and the linewidth of the magnetic resonance signal with the dipole bench described in Sec. 3.1. The linewidth is defined as the full width at half maximum (FWHM). Figure 6.2 shows the impact of the ramp rate ($\dot{B}$) on the marker-field value. This value is unchanged within 10 μT, which corresponds to a relative variation of 2.6×10^{-4}.

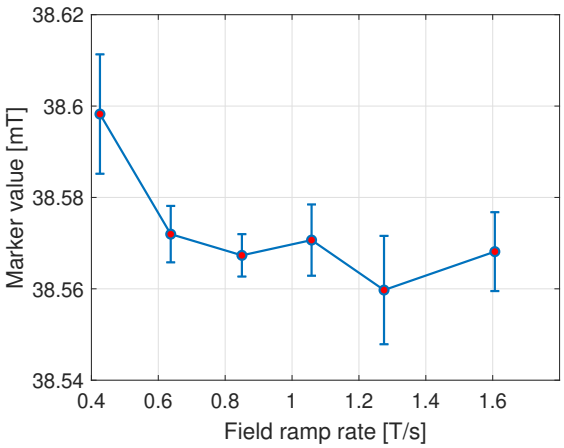

Figure 6.2 – Field ramp rate effect on the measured field value.

We measured a constant linewidth of 320 μT within ±10 μT over a range of ramp rates from 0.4 to 1.6 T/s.

6.3 Gradient effect

The sensitivity to a magnetic-field gradient is a relevant parameter, since the sensor shall be installed in non-homogeneous fields. In the first application, the 36 mT sensor will be installed in the PS combined function magnet (as discussed in Sec. 9.1), which generates a quadrupolar

field on top of a dipolar field. In the second application, the 106 mT sensor will be installed in the fringe field of the LEIR main bending dipole (as detailed in Sec. 10.1).

The measurements were performed in pulsed mode in the quadrupole calibration bench described in Sec. 3.2. To determine the quadrupole component, we used the excitation current in the magnet. The relation between the gradient versus the current, which is known as the transfer function of the magnet, was measured offline with a rotating coil magnetometer. The sensor was step-wise positioned close to the magnetic axis where the field is null, therefore increasing the field inhomogeneity G/B_{m} ratio while the marker-field level remained the same.

As shown in Fig. 6.3, the resonance linewidth is weakly affected by field gradients up to 1.2 T/m. This is not surprising because at this field gradient, the field difference across the 0.3 mm diameter sphere is 360 μT, that is, approximately equal to the linewidth at zero gradient. As expected and shown in Fig. 6.3, the resonance position is also unaffected by the field gradients.

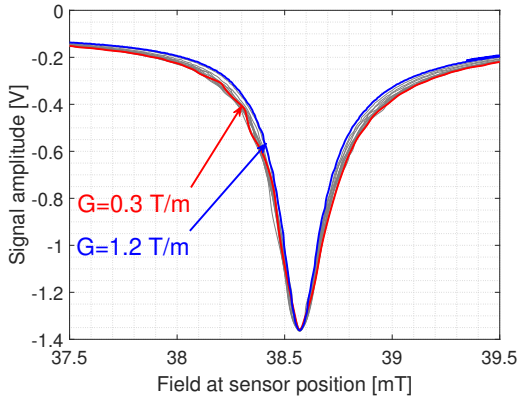

Figure 6.3 – Gradient effect on the linewidth and resonance position.

6.4 Effect of the field direction

The field direction sensitivity is the influence of the angular position of the sensor with respect to the external field direction on the effective gyromagnetic ratio. The coordinate system is defined in the Figure 4.3a. We measured the three angular directions ϕ (pitch, rotation about x-axis), φ (yaw, rotation about y-axis), and ψ (roll, rotation about z-axis) with respect to the main field orientation B_0 along y-axis. The center of the coordinate system is at the YIG sphere position. We used the goniometer introduced in Sec. 3.3 to rotate the sensor by steps of 2°; the roll angle up to ±8° and the pitch angle up to +4°, limited by the magnet aperture. For the yaw angle, we used the sensors support to rotate by steps of ±90°. Figure 6.4 shows the marker value variation as a function of the angle. The sensor sensitivity to the roll angle is $\psi = 433\ \mu\mathrm{T}/°$.

This is mainly explained by the angle α (in Eq. 2.10) between the field B_0 with respect to the YIG sphere's temperature stable axis. A minor contribution is attributed to the angle

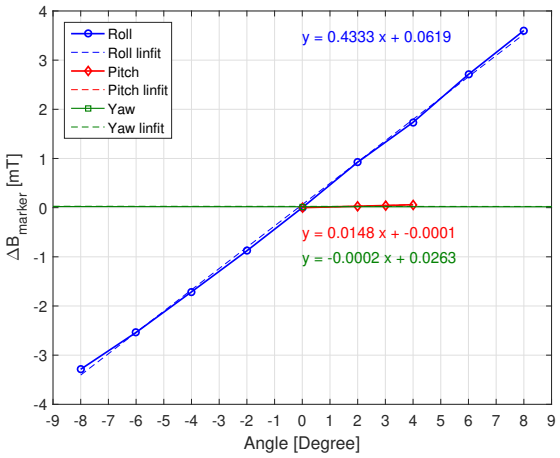

Figure 6.4 – Field direction effect on the marker level.

between the field B_0 with respect to the RF excitation field B_1 direction, which deviates from the optimum value of 90°. There is also a small sensitivity to the pitch angle of about 15 μT/° due to cross-sensitivity between the two rotation axes. The yaw angle has negligible effect on the field measurement. The roll angle variation implies mechanical tolerances of 2 μm on the sensor support to reach 25 μT of absolute accuracy. We took into account this tight tolerance for the design of the support in the PS and LEIR magnets.

6.5 Temperature effect and stable axis adjustment

For the YIG filters, this process is performed by its embedded electro-magnet and heater system. For the FMR sensor proposed in this work, we set up a special bench detailed in Sec. 3.3. The temperature-stable axis is aligned with the field when the resonance peak does not change with temperature and corresponds to an angle $\alpha = \pm 29.7$ ° as detailed in Sec. 2.3.1. This is achieved by an iterative process consisting of the rotation of the rod, the adjustment of the magnetic field to keep the magnetic resonance in the minimum peak of the resonator (see red curve in Fig. 6.5), and toggling the heater in ON/OFF position. When the stable axis was identified, we tightened the fixation screws of the ceramic rod support and re-checked the magnetic resonance in case of the tightening changed the mechanical position of the sphere.

In order to measure precisely the temperature dependency after the alignment along the stable axis, we installed the sensor in the dipole calibration bench described in Section 3.1 equipped with the Peltier module extension where the temperature and the magnetic field are well controlled and measured.

Figure 6.6 shows the marker field level dependency with respect to the temperature before (red line) and after (green line) the stable axis alignment procedure. A variation of 4 μT/°C is adequate as the PS reference magnet is in a temperature controlled room with ±2°C variation, corresponding to a field error of 16 μT. On the contrary, for the LEIR reference magnet which

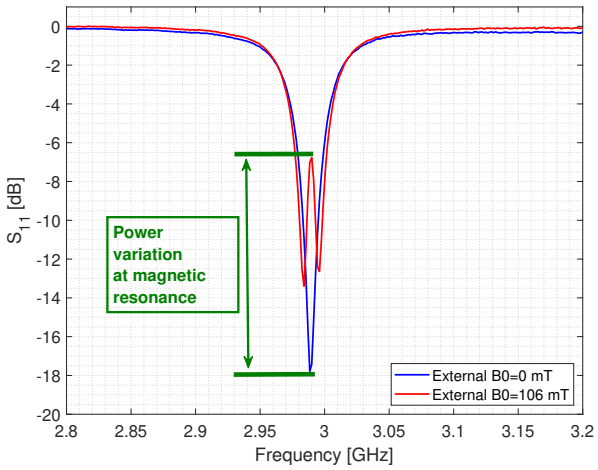

Figure 6.5 – Return loss of the 3 GHz resonator, the blue curve is with B_0 outside magnetic resonance, the red curve is with B_0 at the magnetic resonance.

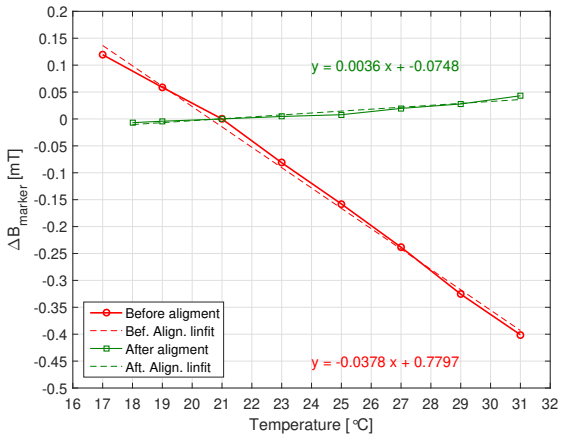

Figure 6.6 – Temperature stable axis alignment.

is exposed to higher temperature variation, we decided to add a heating controlled system in order to limit the temperature variation impact on the marker as well as the induction coil as detailed in Sec.10.1.

6.6 Summary of results

We performed identical measurements also with the 106 mT FMR sensor. The Table 6.2 summarizes the main results obtained with both sensors.

Table 6.2 – FMR resonator sensors summary.

Parameters	36 mT resonator	106 mT resonator
Operating frequency (MHz)	1109	3050
Q (-)	36	81
B_{m} (mT)	35.9	106.3
Linewidth (μT)	320	370
Effective γ (GHz/T)	28.29±0.01	28.69±0.01
$\dot{B}$ sensitivity (-)	no effect up to 2.3 T/s	no effect up to 5 T/s
Gradient sensitivity (μT/(T/m))	-56	0
Temperature sensitivity (μT/°C)	3.6	2.2
Field direction sensitivity ψ (μT/°)	433	368
Resolution (nT/Hz$^{1/2}$)	0.7	1.3
Bandwidth (kHz)	150	150
Integrated resolution (μT_{RMS})	0.3	0.5

7 Characterisation of the EPR resonator sensors

We detail in this chapter the measurements preformed on the 106 mT sensors with paramagnetic sample mounted on the 3 GHz resonator structure respectively. However, identical setup, operation and characterisation were realized on the 36 mT (i.e., 1 GHz) sensor with paramagnetic sample. The performance obtained with this sensors is summarised at the end of the chapter.

7.1 Sample preparation

We positioned a single crystal of BDPA with a size of $920 \times 390 \times 450\,\mu\text{m}^3$ on the co-planar waveguide at 2.4 mm from the trace short-end (see Fig. 7.1d), where the excitation field B_1 is the strongest (previously determined in Sec. 5.2).

In order to fix the sample on the PCB at its optimal position, we first encapsulated it to minimize the degradation of its magnetic properties due to reaction with the ambient air. We wrapped the sample into a polyethylene terephthalate (PET) shrink tube (Nordson Medical, 103-0002) as shown in Fig. 7.1b. We chose the smallest available wall thickness of 6 μm to minimize the distance between the sample and the PCB surface. The shrink tube was heated up to about 70 °C, and after its cool-down we positioned the packet on the PCB and covered it with epoxy resin (Araldite®) as shown in Fig. 7.1d. The tube also prevents any direct contact between the resin and the BDPA sample, which would strongly react chemically during polymerization of the resin and lose it EPR properties, as we observed on dummy samples.

7.2 Detection electronics

The magnetic resonance signal with the resonator is detected by a 180° hybrid coupler, combined with a RF amplifier with a gain of $G_{\text{rf}} = 126$ (42 dB) as shown in Fig. 7.2. We recall that we designed the sensor to approximately match 50 Ω such that the coupler output signal

This chapter is reproduced with changes from [111].

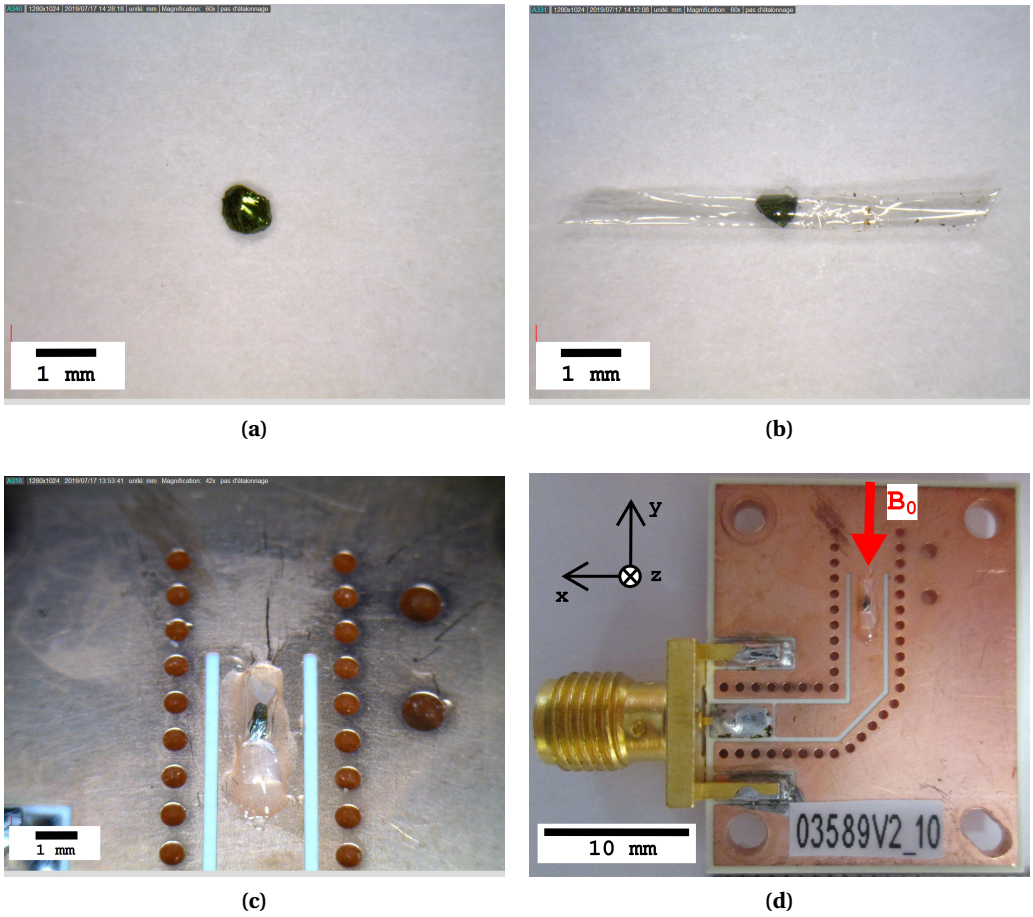

(a) (b)

(c) (d)

Figure 7.1 – 106 mT resonator sensor with EPR sample. (a) BDPA crystal. (b) Sample embedded into the shrink tube. (c) Sample glued on the PCB. (d) 3 GHz resonator with the BDPA sample.

is minimized (and limited only by the coupler directivity). At the magnetic resonance, the matched circuit is perturbed and a fraction of the input signal is transferred to the output of the hybrid coupler. After RF amplification, a Schottky diode is used as power detector, converting the RF signal into a LF signal. The EPR electronics includes an attenuator of 6 dB at the Schottky diode input in order to increase B_1 at the sensor while keeping the RF signal in the linear range of the Schottky diode (about -200 mV). A low noise amplifier with a gain $G_{\text{lf}} = 1000$ (60 dB) amplifies and a bandpass filter (1.5 Hz to 100 kHz) the LF signal of ± 10 V level for the input of the DAQ as shown in Fig. 7.2.
The devices used for the detection are shown in Tab. 7.1.

The detection chain is identical for the 36 mT and the 106 mT EPR sensors.

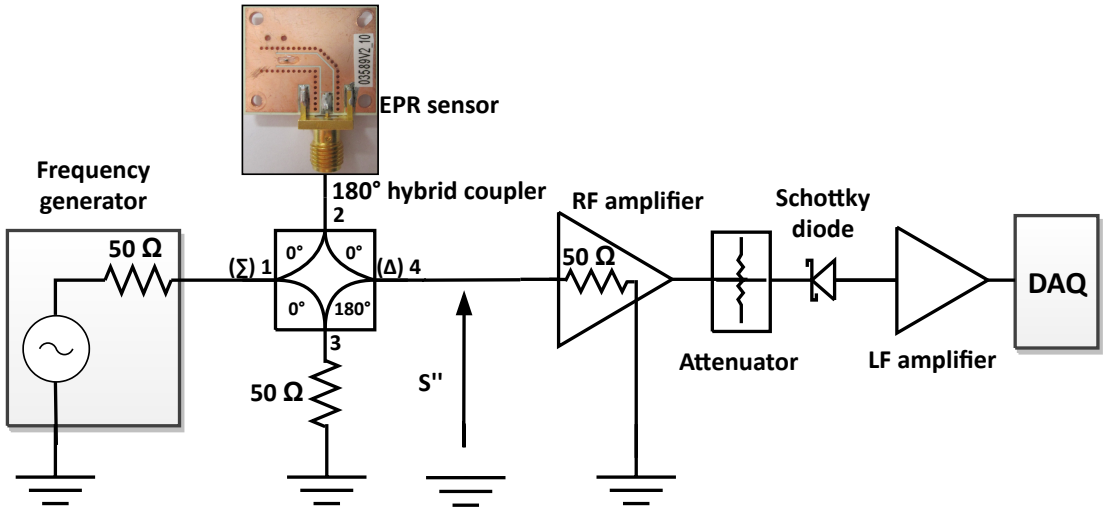

Figure 7.2 – Schematic layout of the EPR detection electronics for the resonator structures.

Table 7.1 – EPR resonator detection electronics components.

Components	Manufacturer	Model
Frequency Generator 0.0001-20 GHz	Anapico	APSIN20GHz
Hybrid coupler 180° 0.75-12.4 GHz	Cernex, Inc.	CHCU7120320T180
Attenuator 6 dB	Radiall	R411806124
Low frequency amplifier	FEMTO	DLPVA-100-B-D
50 Ω termination 0-12 GHz	Mini-Circuits	ANNE-50L+
RF amplifier 0.5-8 GHz gain 42 dB	Narda-MITEQ	AMF-4D-00500800-18-13P-HS-R
Schottky Diode	Agilent Technologies	8473B
DAQ	National Instruments	USB-6366

7.3 Resonator noise and signal characterisation

7.3.1 Theory

We present in this section the computation for an arbitrary resonator proposed by Dr. G. Boero [112] and reported in Ref. [111]. This model is compared with respect to the measurements performed on the sensor as shown in detail in Sec. 7.3.2.

Neglecting all losses in the connections, the rms value of EPR signal at the input of the RF amplifier in Fig. 7.2 can be written as [57]

$$S'' = \frac{1}{2}\chi'' \eta Q_u E, \tag{7.1}$$

where χ'' is the imaginary part of the magnetic susceptibility, η is the filling factor [57, 105], Q_u is the unloaded Q-factor of the resonator. The power available from the RF generator at the resonator is $P_w = E^2/4R_0$, where E is the rms value of the RF generator voltage, and R_0 is the

matched impedance of the resonator at resonance (which is also equal to the RF generator output impedance, the characteristic impedance of the connecting cables, and the input impedance of the RF amplifier). In our case, as in most of the EPR systems $R_0 = 50\,\Omega$. The previous equation can be written in a different form as follow. In resonance conditions

$$\chi'' = \frac{1}{2}\frac{\chi_0 \omega_0 T_2}{1+\gamma_e^2 B_1^2 T_1 T_2}, \tag{7.2}$$

where T_1 and T_2 are the sample relaxation times, χ_0 is the static magnetic susceptibility, ω_0 is the resonance angular frequency, and B_1 is the amplitude of the circularly polarized component of the RF excitation field precessing in the same direction as the magnetization. The unloaded Q-factor can be written as $Q_u = \Lambda^2 V_s \omega_0 / \mu_0 \eta$ [113], where V_s is the sample volume, and the resonator efficiency parameter is defined as $\Lambda = B_1/\sqrt{P_w}$. With these relations and assumption, the rms value of the EPR signal at the input of the RF preamplifier can be re-written as

$$S'' = \frac{1}{2}\frac{\gamma_e B_1 T_2}{1+\gamma_e^2 B_1^2 T_1 T_2}\omega_0 M_0 V_s \Lambda \sqrt{R_0}. \tag{7.3}$$

where the magnetization of the sample is $M_0 = (\chi_0 B_0/\mu_0)$, where μ_0 is the permeability of vacuum. The static magnetic susceptibility χ_0, for a spin 1/2 system and $\mu B_0 << k_B T$ where μ is the intrinsic magnetic moment, is given by

$$\chi_0 = \frac{\mu_0 n_s \gamma_e^2 \hbar^2}{4 k_B T} \tag{7.4}$$

where n_s is the spin density, $\hbar$ is the reduced Planck constant, k_B is the Boltzmann constant, and T is the sample temperature.
Neglecting all noise sources except the thermal noise of the impedance matched resonator, the noise spectral density (in $V/Hz^{1/2}$) at the input of the RF amplifier can be written as

$$n'' = \sqrt{4 k_B T R_0}. \tag{7.5}$$

The signal and the noise are conditioned through the detection electronics considering the attenuation, the amplification, and the additional noise sources we can obtain the signal and the noise at the input of the analog-to-digital converter of the DAQ system in Fig. 7.2 signal as follow. The signal at the DAQ input is:

$$S = S''(A_c A_h A_a A_d)(G_{rf} G_{lf}) \tag{7.6}$$

where the A coefficients are the attenuation factors, A_c is the contribution of the cables, A_h is the contribution of the hybrid coupler, A_a is the contribution of the attenuator, and A_d is the contribution of the Schottky diode. G_{rf} is the gain of the RF amplifier, and G_{lf} is the gain of the LF amplifier after the Schottky diode. The noise spectral density at the DAQ input is given by

$$n = G_{lf}\sqrt{(n')^2 + n_d^2 + n_a^2} \tag{7.7}$$

where n_d is the noise contribution from the diode, $n_\mathrm{a} = \sqrt{v_\mathrm{n}^2 + (R_\mathrm{n} i_\mathrm{n})^2}$ is the noise of the low frequency amplifier, v_n is the equivalent input voltage noise of the amplifier, R_n is the output diode impedance, i_n is the equivalent input current noise of the amplifier, and

$$n' = n'' G_\mathrm{rf} N_F A_\mathrm{a} A_\mathrm{d}, \tag{7.8}$$

is the noise contribution from the RF part of the detection electronics, where N_F is the noise figure of the RF amplifier. Finally, the rms value of the noise at the input of the DAQ system is

$$N = n\sqrt{\Delta f} \tag{7.9}$$

where $\sqrt{\Delta f}$ is the equivalent noise bandwidth at the input of the DAQ system.

7.3.2 Comparison with respect to the measurements

We measured the marker signal as shown in Fig. 7.3 under nominal operation conditions (0.6 T/s, 23 °C, no field gradient, B_0 // y-axis). We calculated the sensitivity of the sensor (in V/T) from the derivative of the marker signal, then determined its resolution. We recall that the resolution is defined as the noise spectral density over the sensitivity.

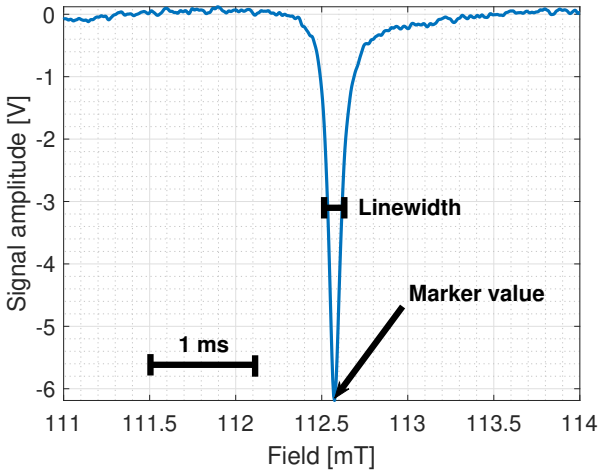

Figure 7.3 – Typical field marker signal with the 106 mT EPR sensor with the resonator structure for $\dot{B} = 0.6$ T/s.

After the LF amplifier we measured a sensitivity of $\delta = 90800$ V/T, and a noise spectral density of $N_\mathrm{sd} = 200\ \mu\mathrm{V/Hz^{1/2}}$ (i.e. 63 mV_{rms} with a bandwidth of 100 kHz) above the $1/f$ corner frequency of 20 kHz, hence the resolution is $\Xi = 2\ \mathrm{nT/Hz^{1/2}}$.

From Eq. (7.4), assuming $n_\mathrm{s} = 1.5 \times 10^{27}\ \mathrm{spin/m^3}$, $T = 296$ K, we obtain a static susceptibility $\chi_0 = 3.97 \times 10^{-5}$. Hence, for $B_0 = 111.4$ mT, the static magnetization is $M_0 = 3.52$ A/m. From Eq. (7.3) the signal at the input of the RF amplifier without losses in the connections is expected

to be S'' = 275 μV, where we have assumed $T_1 = T_2$ = 100 ns [114, 94], $\omega_0 = 1.9622 \times 10^{10}$ s^{-1}, $V_s = 920 \times 390 \times 450$ μm^3, and $\Lambda = 157$ μT/W$^{1/2}$ (considering $P_w = -5.86$ dBm, $R_0 = 50\,\Omega$, and $B_1 = 2.5$ μT obtained from simulations detailed in Sec. 5.2). From Eq. (7.6), assuming $A_c = 0.7$, $A_h = 0.6$, $A_a = 0.5$, $A_d = -0.7$, $G_{rf} = 126$, $G_{lf} = 1000$, the signal amplitude at the input of the data acquisition system is $S = -5.7$ V. This theoretical value is very close to the measured value of -6.2 V (see Fig. 7.3). The small difference is probably due to the difficulty in estimating accurately the sample volume by optical microscopy.

From Eq. (7.5), with T=296 K and R_0=50 Ω, the noise spectral density at the RF amplifier input n'' is about 0.9 nV/Hz$^{1/2}$. Considering $N_F = 1.5$, $v_n = 4$ nV/Hz$^{1/2}$, $i_n = 2$ pA/Hz$^{1/2}$, $R_n = 1.3$ kΩ, we obtain n'=60 nV/Hz$^{1/2}$ and n_a=5 nV/Hz$^{1/2}$. The diode noise spectral density is $n_d = 110$ nV/Hz$^{1/2}$, which is, despite the effective RF gain of about 42 dB, almost a factor two larger than the noise n' from the RF circuitry. Hence, the expected noise spectral density at input of the DAQ system is n=127 μV/Hz$^{1/2}$ and its rms value considering a noise equivalent bandwidth Δf=100 kHz is $N = 40$ mV$_{rms}$. This value is about 1.6 times lower than the measured noise, probably due a non negligible contribution of the RF signal generator amplitude noise. Overall, the measured signal, noise, and signal-to-noise ratio (SNR) are, within a factor of two, in agreement with the theoretically expected values.

7.4 Ramp rate effect

In order to determine the influence of the field ramp rate, we measured the position and the line width of the magnetic resonance signal as a function of $\dot{B}$. The line width is defined as the FWHM. The field marker is defined as the corresponding field at minimum value of the marker signal (the peak) as shown in Fig. 7.3.

Figure 7.4a shows the impact of $\dot{B}$ on the marker-field value. The measured marked field value is 111.408±0.007 mT up to 5 T/s (i.e., to an effective $\gamma/2\pi$ = 28.03 GHz/T for a frequency of 3.123 GHz), which corresponds to a relative variation of 1.3×10^{-4}. The measured relative variation is similar to the one measured with a YIG sample on a 3 GHz resonator as shown in Sec. 6.2. The error bars in Fig. 7.4a correspond to the standard deviation of the marker value over ten repeated magnetic cycles. The linewidth is 85 μT up to a ramp rate of 2.5 T/s. At $\dot{B} = 5$ T/s, the linewidth increases to 100 μT, as shown in Fig. 7.4b.

7.5 Gradient effect

We recall that the gradient effect is measured in the quadrupole bench detailed in Sec. 3.2. The sensor was step-wise positioned close to the magnetic axis where the field is null, therefore increasing the field inhomogeneity G/B_m ratio while the marker-field level remained the same.

As shown in Fig. 7.5a, the marker signal amplitude and line width are broadened by field gradients as expected. For gradients higher than 1.5 T/m (i.e., $G/B_m = 13$ m^{-1}), the signal

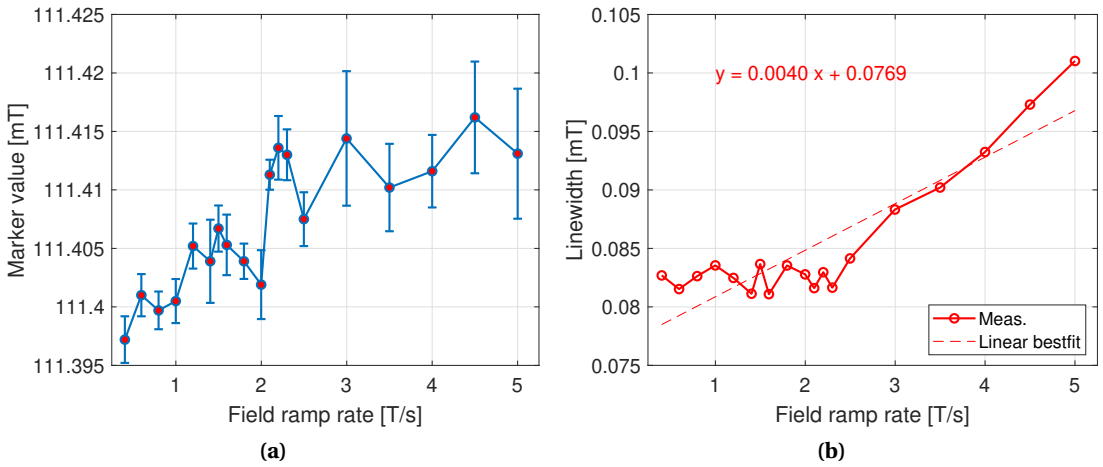

Figure 7.4 – Field ramp rate effect on the 106 mT EPR sensor.(a) Field value.(b) linewidth.

becomes difficult to detect with the current electronics. The SNR for slow ramp rates can be improved by reducing the filter bandwidth. We attribute the broadening of the signal to the field difference across the sample. With a homogeneity of 34 m^{-1} (i.e., 3.7 T/m at 0.11 T) we would expect, on a sample size of about 450 μm along the gradient direction, a linewidth of about 1.6 mT, in good agreement with the measured value of about 2.1 mT (which is about twenty times larger than the linewidth at zero gradient). The line width increases linearly from about 1.5 T/m by 0.5 mT/(T/m) as shown in Fig.7.5b.

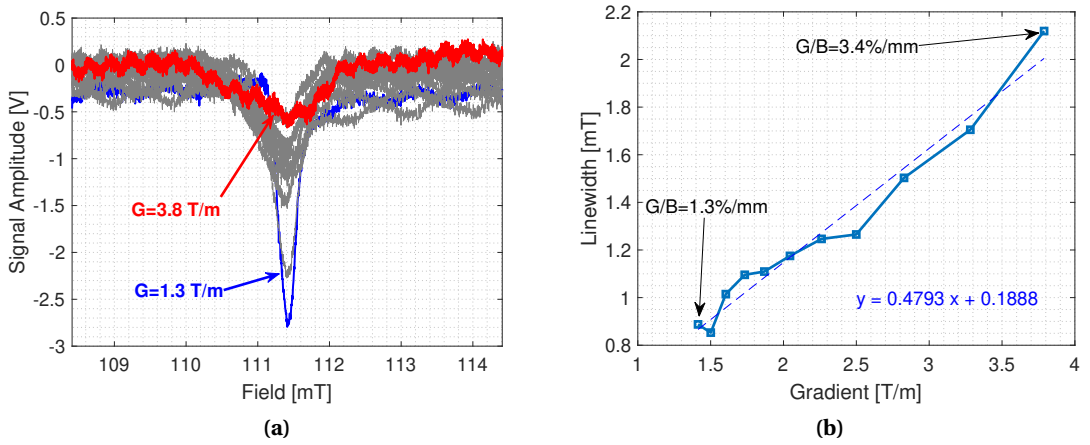

Figure 7.5 – Gradient effect on the EPR 106 mT sensor.(a) On the 106 mT EPR sensor marker signal. (b) On the 106 mT EPR sensor linewidth.

7.6 Effect of the field direction

We recall that the field direction sensitivity is the influence of the angular position of the sensor with respect to the magnetic field direction B_0 on the effective gyromagnetic ratio. We used

the dipole bench described in the Sec. 3.1.
Contrary to a not aligned YIG sample where the sensor sensitivity to the angle about the z-axis (according to the coordinate system in Fig. 7.1d) is $\psi = 433\ \mu\text{T}/°$ as shown in Sec. 6.4 the sensors with BDPA sample (i.e., resonator 1 and 3 GHz; oscillator 10 GHz and 20 GHz) are insensitive to any rotation within the measurement uncertainty and magnet field homogeneity.

As the effective γ is not impacted, the mechanical alignment and stability are not critical parameters to be considered.

7.7 Temperature effect

In order to measure the temperature sensitivity, we installed the sensor in the dipole calibration bench described in the Sec. 3.3 equipped with a Peltier module extension where the temperature and the magnetic field are well controlled and measured. Figure 7.6 shows the marker field value with respect to the temperature for the 3 GHz resonator. The measured temperature sensitivity is 7 μT/°C, independently on the BDPA crystal orientation with respect to the magnetic field. This temperature cross-sensitivity is much lower than the one observed for YIG sphere based sensors with the crystal axis in an arbitrary direction. Hence, the complex alignment required for the YIG spheres is not necessary for the BDPA based sensors. Nevertheless, when the sensors will be installed in environments where the temperature variation exceeds ±2.4 °C, the temperature cross-sensitivity will produce a field error of 17 μT. Hence, to comply with the required relative field stability of 1.5×10^{-4}, a temperature control system will be required.

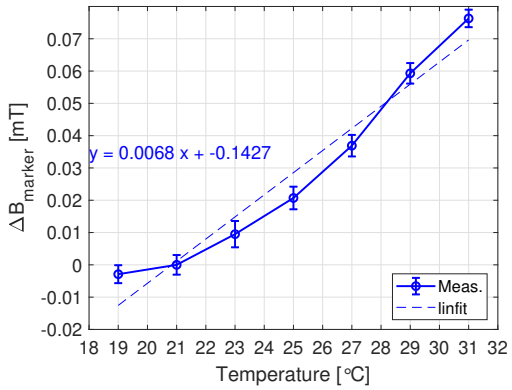

Figure 7.6 – Temperature sensitivity on 106 mT EPR sensor.

7.8 Summary of results

The Table 7.2 summarizes the main results obtained with both sensors. We measured lower gradient sensitivity by a factor three with the 36 mT EPR sensor because the sample size is smaller. The other parameters are more or less identical.

Table 7.2 – EPR resonator sensors summary.

Parameters	36 mT resonator	106 mT resonator
Operating frequency (MHz)	1078.9	3123
B_{m} (mT)	38.52	111.41
Linewidth (μT)	94	85
Effective γ (GHz/T)	28.01±0.01	28.03±0.01
Sample volume (μm^3)	63.0×10^6	161.5×10^6
$\dot{B}$ sensitivity (μT/(T/s))	4	4
Gradient sensitivity (μT/(T/m))	160	480
Maximum gradient (T/m)	1.2	1.5
Maximum field inhomogenity G/B_{m} (m^{-1})	31	13
Temperature sensitivity (μT/°C)	4.8	7
Field direction sensitivity ψ (μT/°)	<1	<1
Sensor sensitivity (V/T)	47450	90800
Noise floor (V/Hz$^{1/2}$)	0.26×10^{-3}	0.2×10^{-3}
Resolution (nT/Hz$^{1/2}$)	5.5	2.2
Bandwidth (kHz)	100	100
Integrated resolution ($\mu\mathrm{T}_{RMS}$)	1.73	0.70
SNR (-)	39	98

8 Characterisation of the EPR oscillator sensors

We present in this chapter the measurements preformed on the 360 mT and 710 mT sensors with paramagnetic sample mounted on the 10 GHz and 20 GHz oscillator structure respectively. Both oscillators are mounted on a single chip designed by Dr. G. Boero and Dr. A. V. Matheoud detailed in Ref. [115, 116, 117].

8.1 Oscillator chip

The 10 GHz and 20 GHz oscillator structures are realized on a single silicon chip having total area of about 3 mm^2, using a Complementary Metal Oxide Semiconductor (CMOS) integrated circuit technology. The 10 GHz oscillator consists of an integrated cross-coupled LC oscillator as shown in Fig. 8.1, providing a direct and fixed output frequency. A detailed description of the 10 GHz oscillator can be found in Ref. [115, 117]. The 20 GHz oscillator has two cross-coupled LC oscillators ($oscH$ and $oscL$), each of them is equipped with a pair of voltage controlled capacitors (varicaps), as shown in Fig. 8.2, operating in a range of ±1.8 V to vary the frequency from 18 to 21 GHz. A front-end mixer based on Gilbert cell topology [118] driven by a dedicated power supply module down-converts the output frequency to ±1.5 GHz. A differential output buffer circuit is added to drive 50 Ω characteristic impedance loads. The main parameters for both oscillator types are summarized in Table 8.1.

8.2 PCB design for the oscillators installation

The PCB design was developed for the 20 GHz oscillator requiring eight wire-bonding ports, therefore wire-bonding adaptation was performed to mount and operate the 10 GHz oscillator as it requires only four ports. The PCB laminate has a substrate thickness of 1.524 mm in Rogers™ 4350B and double-face conductor with a thickness of 17 μm in copper. The die is electrically connected either by Al wire bonding (10 GHz oscillator) or Au wire bonding (20 GHz oscillator). The Au wire-bonding pads on the PCB are Ni plated due to the aluminium

This chapter is reproduced with changes from [111].

Table 8.1 – Oscillators design parameters [116, 119].

Parameters	10 GHz osc.	20 GHz osc.
Coil outer diameter (μm)	270	180
Coil trace width (μm)	12	30
Coil resistance (Ω)	10	2.5
Coil inductance (nH)	2.3	0.391
Coil Q-factor (-)	14	20
Varactor min. capa. at -1.8 V (fF)	-	45
Varactor nom. capa. at 0 V (fF)	-	95
Varactor max. capa. at +1.8 V (fF)	-	123

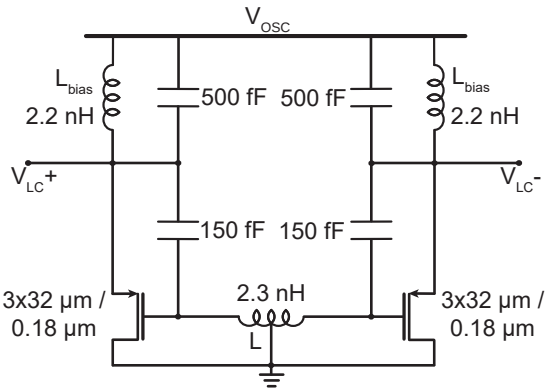

Figure 8.1 – Schematics of the fully integrated 10 GHz oscillator [119].

wedge wire bonding process at CERN [120]. The Ni thickness is about 3 μm to 6 μm, and the bonding pad size is about $800 \times 200\,\mu m^2$. The presence of Ni in the bonding pads produces a negligible perturbation to the homogeneity and absolute value of the magnetic field to be measured, as discussed in Sec. 8.9. The chip was fixed with thermoplastic conductive paste (Staystik®, Cookson Electronics) without encapsulation allowing the installation of the EPR sample on the top surface of the die. Non-ferromagnetic discrete components (in Fig. 8.4a) are used for the biasing and filtering of the power supply and signals as shown in Fig. 8.3. The mechanical interface is compatible with the one used for the resonator version.

8.3 Sample preparation

We selected a BDPA crystal with a size of $170 \times 110 \times 65\,\mu m^3$ for the 360 mT EPR sensor and $60 \times 40 \times 30\,\mu m^3$ for the 710 mT EPR sensor, optimized to provide the largest signal amplitude just below the strong coupling regime [105]. We mounted the sample at the center of the oscillator coil as shown in Fig. 8.4b and Fig. 8.4c. For size reason, we did not encapsulate the BDPA as for the resonator, we only protected it with silicone grease (high vacuum grease, Dow Corning) to avoid chemical reaction with the ambient air and minimize pollution by external

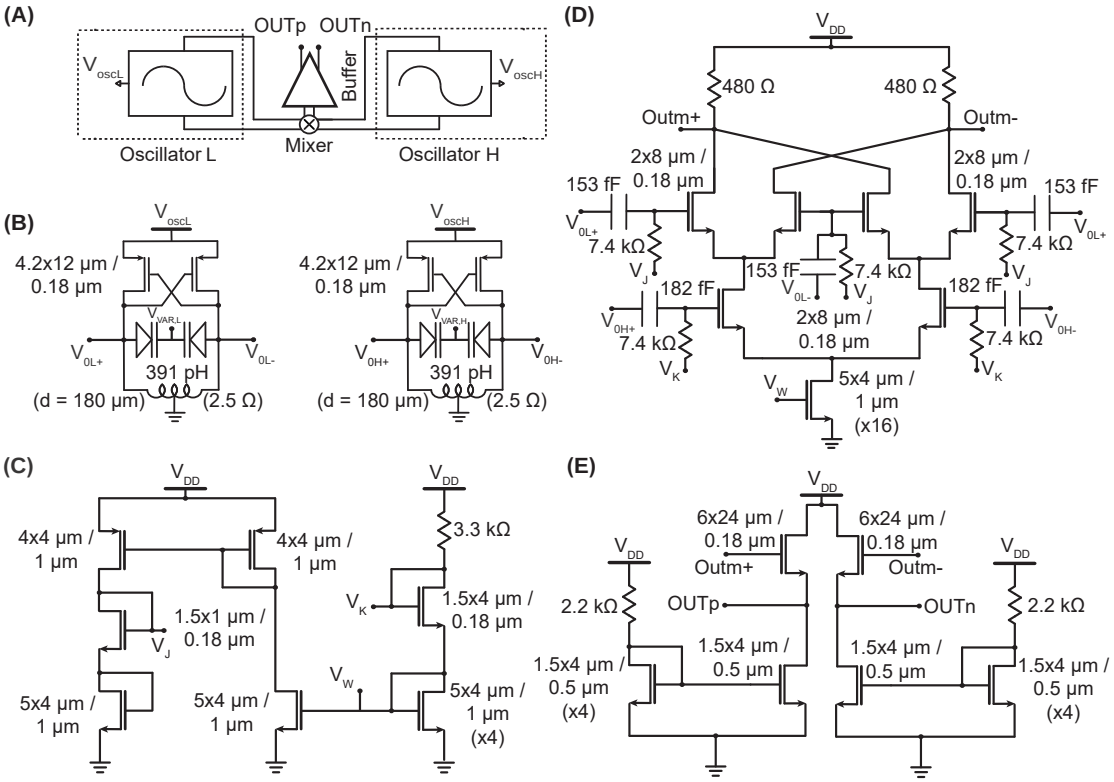

Figure 8.2 – Schematics of the fullly integrated 20 GHz oscillator [119]. (A) Block diagram. (B) Cross-coupled LC oscillator. (C) Mixer power supply module. (D) Front end integrated mixer. (E) Differential output buffer.

elements.

All the sample dimensions were measured with a Hirox RH-2000 digital microscope. For the length and width (xy-plane) the 2D pictures were used as shown in Fig. 8.4b and Fig. 8.4c, for the sample height (z-axis) a 3D reconstruction by shape-from-focus method (SFF) was used as shown in Fig. 8.5. The measurement volume error is considered less than 40% and overestimated as we performed a projection of the measured sample area along the measured height.

8.4 Detection electronics

The magnetic resonance signal of the oscillator is detected by a home-made dedicated phase-locked loop (PLL) originally designed by Dr. A. V. Matheoud (detailed in Ref. [117]) and adapted for a lock frequency range from 150 to 200 MHz as presented in the Appendix B.2 with a frequency noise of about 2 Hz/Hz$^{1/2}$. The PLL acts as frequency-to-voltage converter and has two output signals: a DC output with a low pass filter of 8 Hz (to measure the absolute value of the oscillator frequency and its slow variations) and an AC output with a band pass filter of 0.160-160 kHz (to measure fast variations of the oscillator frequency). The sensitivity of the

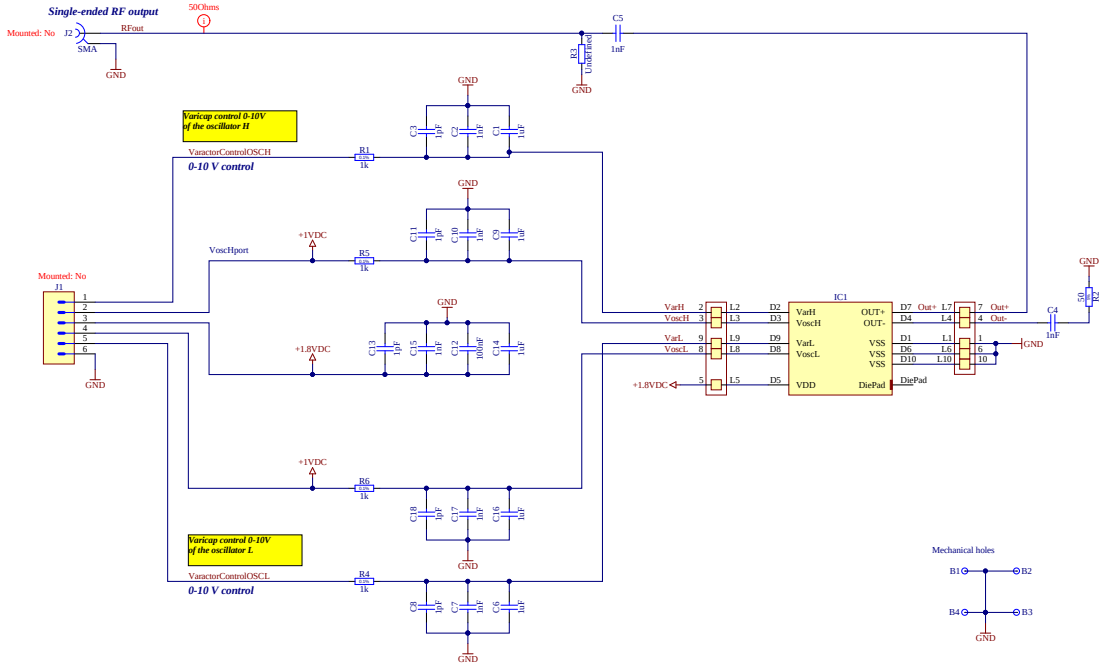

Figure 8.3 – PCB layout for the oscillator sensor.

DC and AC outputs is of about 49 and 67 nV/Hz, respectively (see Fig. 8.6a and Fig. 8.6b).

For the 10 GHz oscillator the RF output signal is down-converted with two mixer stages to a 175 MHz base-band frequency, as shown in Fig. 8.7. The first mixer (connectorized) stage down-converts the frequency from 10 GHz to 2.5 GHz, the second mixer (SMD) stage is embedded in a electronic board to down-convert the frequency from 2.5 GHz to 175 MHz. Filters and amplifiers are used for the signal conditioning between the different stages.
The electronic board (detailed in Appendix B) is composed of a carrier board in 3U Eurocard format as shown in Fig. 8.8a, which accepts mezzanine cards for oscillator as shown in Fig. 8.8b and later for the resonator. The carrier board is produced with standard PCB technology and includes the control and low frequency signal conditioning. For future developments, we added a local frequency generator of 0.5-6 GHz connected to the mezzanine board with an SMP connector. The mezzanine is designed for RF applications on a RF substrate (Rogers Corporation, RO4350B™), with impedance controlled traces and a EMI screen to limit electromagnetic interference from external sources and reduce electromagnetic pollution to the neighbouring boards of the B-Train chassis.

For the 20 GHz oscillator chip, the RF output frequency is up to 2 GHz due to the presence of two variable oscillators and an integrated mixer. The RF output signal is amplified by a low noise amplifier (Mini-circuits, ZX60-83LN-S+) and is connected to the electronic boards as shown in Fig. 8.8b. The mixer in the mezzanine card is used to downconvert the output frequency of the chip to the PLL optimal operating frequency (162 to 175 MHz).

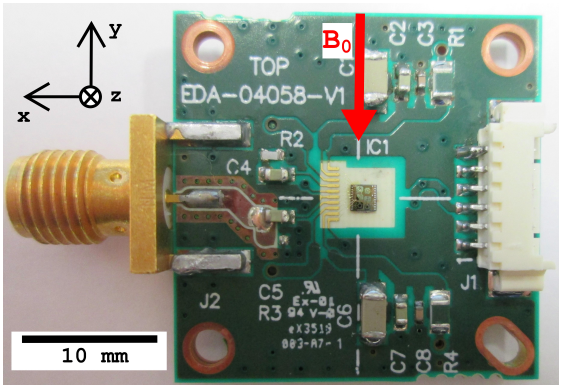

(a)

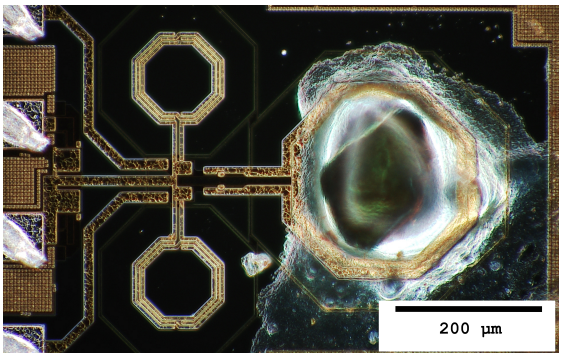

(b)

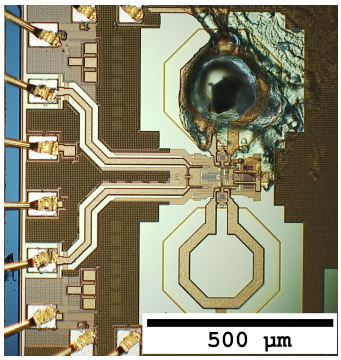

(c)

Figure 8.4 – Oscillator structures. (a) oscillator PCB. (b) BDPA sample installed in the center of the coil and embedded with vacuum grease.(c) BDPA sample installed in the center of the top coil of $oscH$ and covered with vacuum grease.

For the 20 GHz oscillator chip, the RF output frequency is up to 2 GHz due to the presence of two oscillators and an integrated mixer. The RF output signal is amplified by a low noise amplifier (Mini-circuits, ZX60-83LN-S+) and is connected to the electronic boards as shown in Fig. 8.8b. The mixer in the mezzanine card is used to downconvert the output frequency of the chip to the PLL optimal operating frequency (162 to 175 MHz).

The devices used for the detection are shown in Tab.8.2.

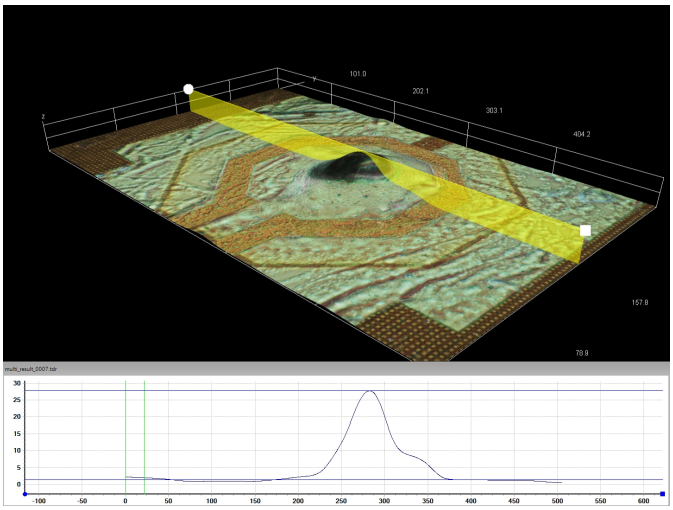

Figure 8.5 – 3D BDPA sample view reconstruction for the 20 GHz oscillator sensor. On the bottom, the thickness profile corresponds to the yellow section in the 3D view.

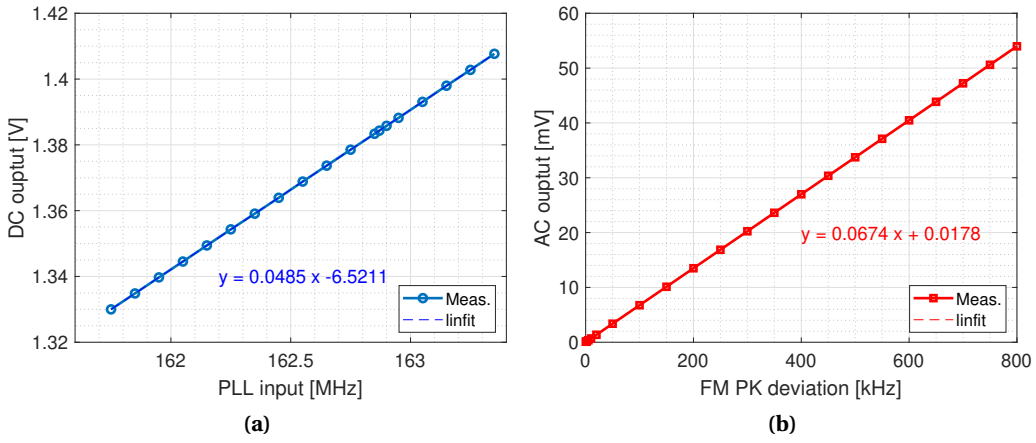

(a) **(b)**

Figure 8.6 – PLL outputs sensitivity. (a) The DC output has a sensitivity of about 49 nV/Hz. (b) The AC output measured with a frequency modulation (FM) of 1 kHz carrier frequency has a sensitivity of 67 nV/Hz.

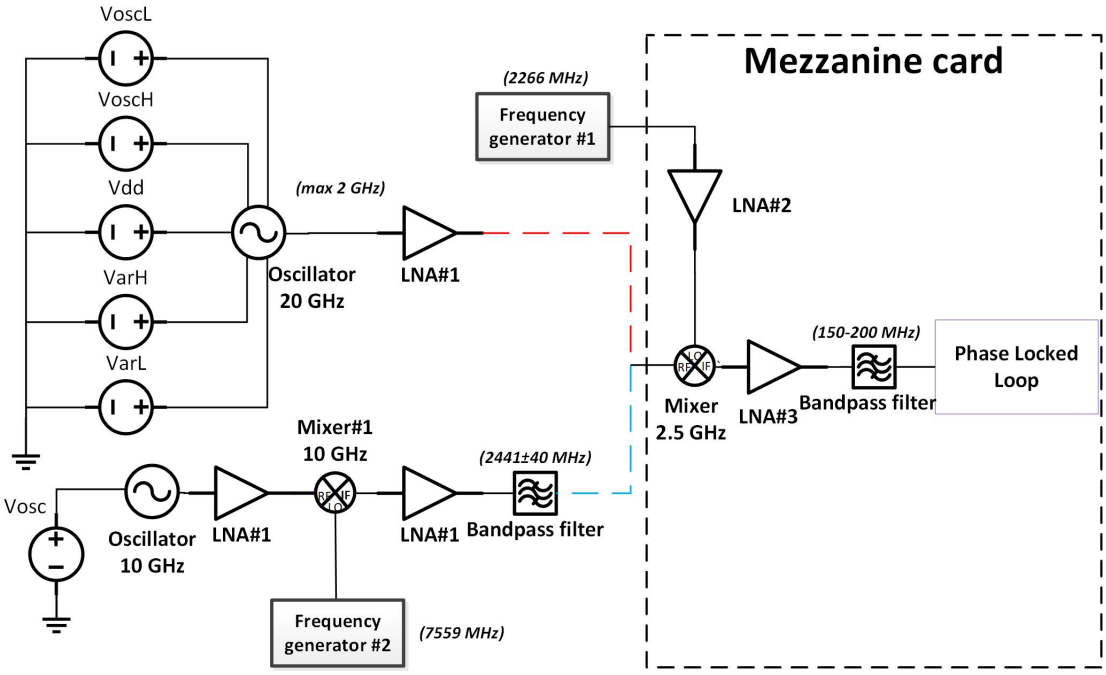

Figure 8.7 – EPR oscillators detection electronics. The 10 GHz and 20 GHz are measured using the same electronic board (mezzanine card). *Vosc* is the power supply for the 10 GHz oscillator. *Vdd* is the power supply for the 20 GHz oscillator auxiliary circuits. *VoscL* and *VoscH* are the power supplies for the lower and higher frequency oscillators, respectively. *VarL* and *VarH* are the voltage source for the lower and higher frequency oscillators variable capacitor, respectively.

Table 8.2 – EPR oscillator detection electronics components. The first part is common for both oscillator structures. The second part is the specific components for the 10 GHz oscillators. The third part is the specific components for the 20 GHz oscillators.

Components	Manufacturer	Model
Frequency Generator#1	TTi	TGR6000
Mixer#2 5-2500 MHz	MACOM	MAMX-007238-CM25MH
RF amplifier#1 500-8000 MHz +21 dB	Mini-circuits	ZX60-83LN-S+
RF amplifier#2 100-10000 MHz +12 dB	Guerrilla	GRF2003
RF amplifier#3 DC-3000 MHz +13 dB	Infineon	BGA420
Bandpass filter 150-200 MHz	CERN	EDA-03593-V2
PLL	CERN/EPFL	-
Power supply *Vosc, Vdd*	FONTAINE	ST-40C
Frequency Generator#2	Anapico	APSIN20GHz
Bandpass filter 2441 MHz BW=83.5 MHz	Crystek	CBPFS-2441
Mixer#1 3700-10000 MHz	Mini-Circuits	ZX05-14-S+
Power supply *VoscL, VoscH*	YOKOGAMA	GS 200
Power supply *VarL,VarH*	ANALOGIC	AN 3100

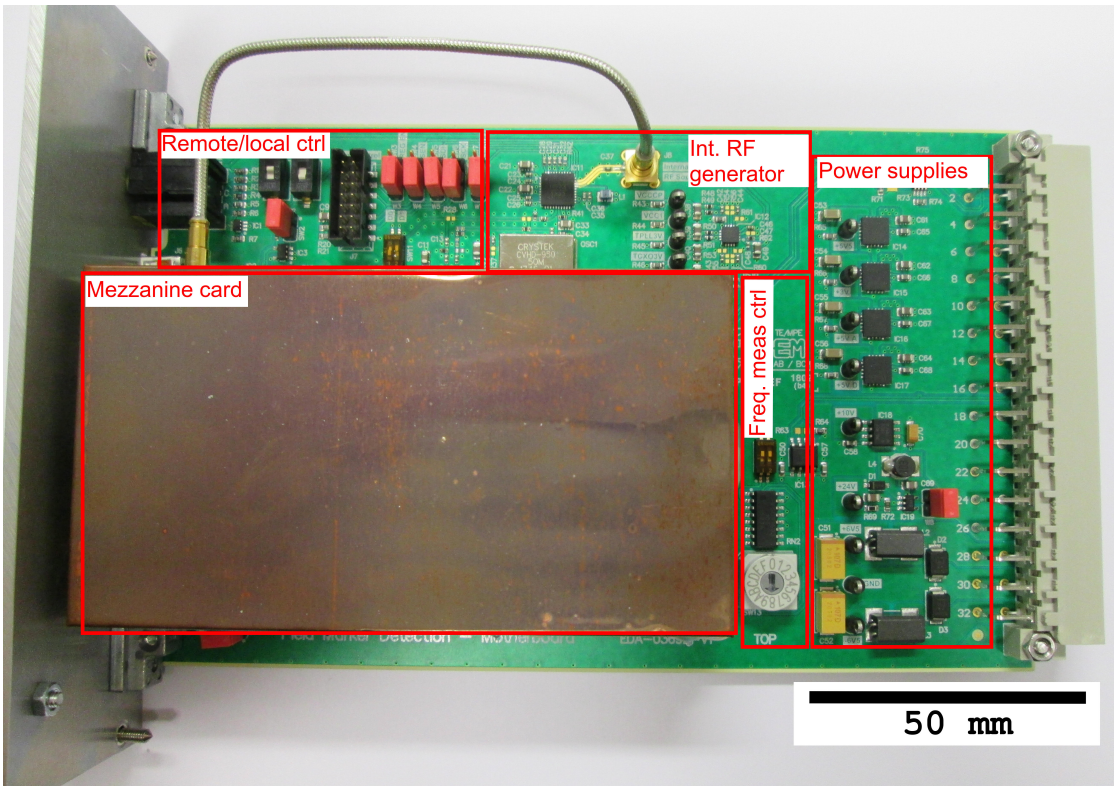

(a)

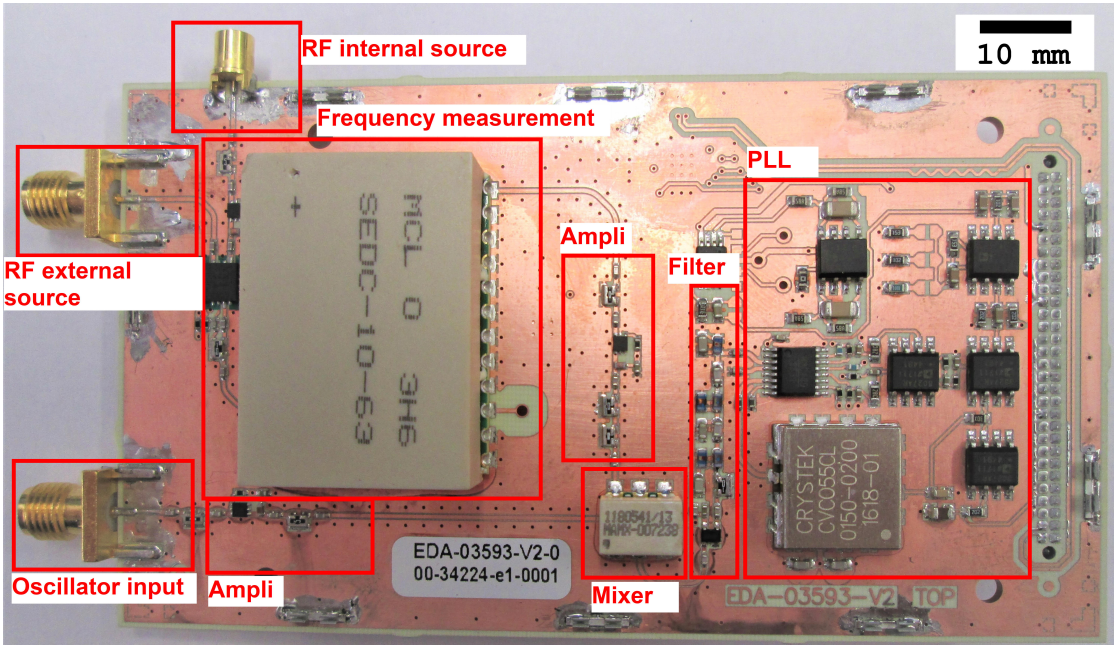

(b)

Figure 8.8 – Oscillator detection electronics board. (a) Carrier board with the mounted mezzanine card. (b) Mezzanine card with the EMI protection removed, where the main functions are illustrated.

8.5 Noise spectral density analysis

The 10 GHz oscillator has the corner frequency at 30 kHz for a noise floor of 3 Hz/Hz$^{1/2}$. The noise peaks at 200 Hz, 400 Hz, 66 kHz and 130 kHz are induced by the first stage down-converter RF generator (ANAPICO).

The noise spectral density of 20 GHz oscillator is almost an order of magnitude larger than the 10 GHz oscillator as show in Fig. 8.9. The two cross-coupled oscillators, the power supply stage, the mixer stage and the voltage source of the varicaps are all contributing to the overall noise. Therefore, a higher noise with respect to a single LC oscillator is expected. The corner frequency of the 20 GHz oscillator is at 100 kHz with a noise floor at 35 Hz/Hz$^{1/2}$.

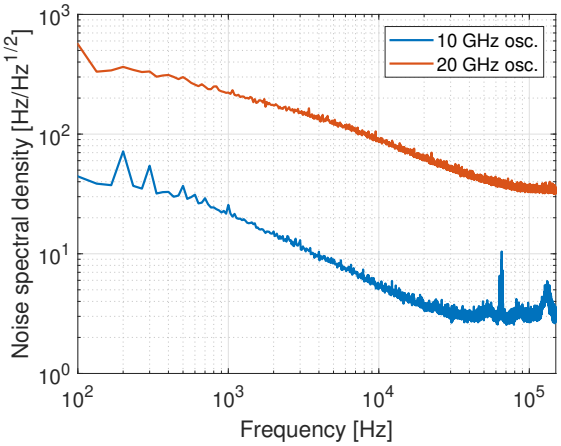

Figure 8.9 – Noise spectral density of the oscillators.

8.6 Oscillator noise and signal computation

8.6.1 Theory

The oscillation frequency of an oscillator coupled with an ensemble of electron spins can be writing as [121, 105]

$$\omega_{\mathrm{LC}\chi} \cong \frac{\omega_{\mathrm{LC}}}{\sqrt{1+\eta\chi'}} \tag{8.1}$$

where

$$\chi' = -\frac{1}{2}\frac{(\omega_{\mathrm{LC}\chi}-\gamma_e B_0)\,T_2^2}{1+(\omega_{\mathrm{LC}\chi}-\gamma_e B_0)^2\,T_2^2+\gamma_e^2 B_1^2 T_1 T_2}\gamma_e B_0 \chi_0, \tag{8.2}$$

ω_{LC} is the unperturbed oscillation frequency (i.e., far away from the magnetic resonance). Due to the correlation of $\omega_{\mathrm{LC}\chi}$ through χ' in both side of the equation (8.1), $\omega_{\mathrm{LC}\chi}$ is obtained by the determination of the roots of the function [105]

$$F(\omega_{\mathrm{LC}\chi}, B_0) = \omega_{\mathrm{LC}\chi} - \frac{\omega_{\mathrm{LC}}}{\sqrt{1+\eta\chi'}} = 0 \tag{8.3}$$

by solving numerically with increment of B_0 and starting far below the magnetic resonance peak. Among the three solutions (two complex, one real), the signal amplitude $\Delta f_{LC\chi} = (\omega_{LC\chi} - \omega_{LC})/2\pi$ is computed from the the peak-to-peak value of the real solution.
The noise of an LC oscillator dominated by the thermal noise of the coil resistance can be written as [121]

$$N_{fLC} = \frac{1}{2\pi}\sqrt{\frac{k_B T R_c \omega_{LC}^2 \Delta f}{V_0^2}} \tag{8.4}$$

where R_c is the coil resistance and V_0 the oscillator voltage amplitude.

8.6.2 Comparison with respect to the measurements

We determined the sensitivity with the method described in Sec. 7.3.2. We measured a sensitivity of 31.7 GHz/T for the 10 GHz sensor, and a noise spectral density of 3 Hz/Hz$^{1/2}$ above the $1/f$ corner frequency of 30 kHz , hence the resolution is 0.095 nT/Hz$^{1/2}$ corresponding to the best performance obtained among the proposed sensors. Considering the bandwidth from 0.160 kHz to 160 kHz, the noise is about 1.2 kHz, giving a resolution of about 40 nT.

Assuming $\eta = 4 \times 10^{-3}$, $\omega_{LC} = 6.353 \times 10^{10}\text{s}^{-1}$, $T_1 = T_2 = 100$ ns, $\chi_0 = 3.97 \times 10^{-5}$ and $B_1 = 80\,\mu$T we obtain, from Eq. (8.3, $\Delta f_{LC\chi} = 2.1$ MHz. The measured signal amplitude is about a factor two lower (i.e, 1.1 MHz) than the computed value, probably due to the uncertainty in the estimation of the the filling factor value. The computed noise from Eq. (8.4) at the same oscillation frequency is $N_{fLC} = 0.9$ kHz (i.e, 2.3 Hz/Hz$^{1/2}$) considering $T = 296$ K, $R_c = 10\,\Omega$, $\Delta f = 160$ kHz and $V_0 = 0.9$ V, which is less than a factor two lower than the measured value.
The measured signal amplitude for the 20 GHz oscillator sensor is also approximately a factor of two smaller than the computed value (the measured amplitude is about 0.8 MHz, whereas the computed amplitude is $\Delta f_{LC\chi} = 1.8$ MHz assuming $\eta = 1 \times 10^{-3}$, $\omega_{LC} = 1.26 \times 10^{11}\text{s}^{-1}$, $T_1 = T_2 = 100$ ns, $\chi_0 = 3.97 \times 10^{-5}$ and $B_1 = 80\,\mu$T). However, the measured noise (i.e, $Nf_{LC} = 14$ kHz, 35 Hz/Hz$^{1/2}$) is about an order of magnitude larger than the computed value (i.e, $\sqrt{2}N_{fLC} = 1.3$ kHz for two oscillators, 3.2 Hz/Hz$^{1/2}$) considering $T = 296$ K, $R_c = 2.5\,\Omega$, $\Delta f = 160$ kHz and $V_0 = 0.9$ V and neglecting all phase noise contributions from the oscillator cross-coupled transistor and the integrated mixer. Due to the uncertainties on the value of these parameters, this moderate disagreement is not unexpected.

8.7 20 GHz oscillator specific measurements

The 20 GHz oscillator is equipped with varicaps to change the operating frequency.
The *varH* varicap is integrated in the higher oscillator *oscH* where the BDPA sample is placed, whereas the *varH* is integrated in the lower oscillator *oscL*, as shown in Fig. 8.4c. In Figure 8.10a we present the relative frequency shift with respect to the applied voltage measured with a frequency counter (TTi, TF930). A variation of the varicap voltage of ±1 V allows obtaining a frequency variation of about ±1.8 GHz (see Fig. 8.10a). The approximately linear region is

between ±0.3 V. When both varicap voltages are set to zero, the oscillator *oscL* has a frequency of 204 MHz higher than the oscillator *oscH*. The field marker can be changed from 660 mT to 720 mT, that is, 18.5 GHz to 20.2 GHz as shown in Fig. 8.10b. This lower frequency range compared to the results presented in Fig.8.10a is due to the limitation of the *varL* voltage for keeping constant the input frequency of 165.5 MHz at the input of the PLL (i.e., 1.37 V).

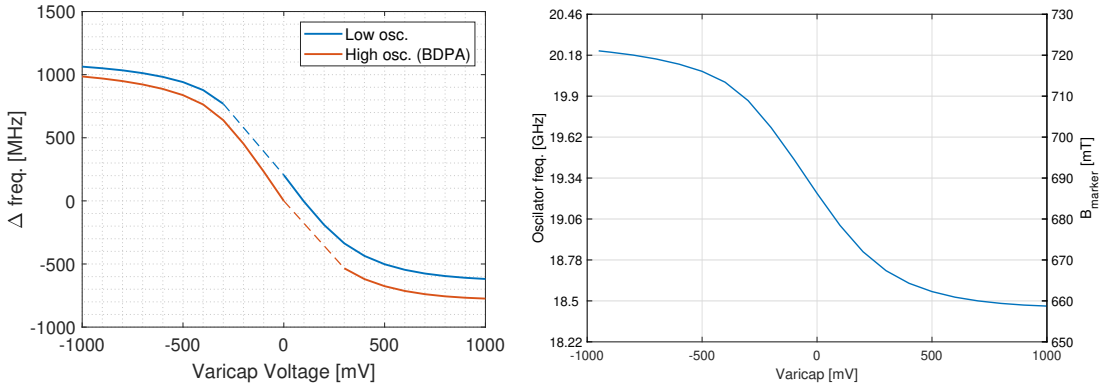

(a) **(b)**

Figure 8.10 – 20 GHz oscillator varicap tuning.(a) The variable capacitor of the low oscillator (in blue), the variable capacitor of the high oscillator (in red). The dash line part of the curve corresponds to the not measurable range of the oscillator frequency. (b). The 20 GHz oscillator field marker tuning capacity. On the left axis, the oscillation frequency determined by theoretical $\gamma_e/2\pi$. On the right axis the measured field marker value.

8.8 Oscillators performance summary

The key features of the 10 GHz and 20 GHz oscillators are summarized in Table 8.3. The maximum supply voltage is 1.8 V, but the largest SNR is obtained for a supply voltage of about 0.9 V This is due to the dependencies of the signal on microwave excitation field B_1 (see Eq. 8.2), of the frequency thermal noise (see Eq. 8.4) and frequency $1/f$ noise on the oscillation amplitude V_0. We have not found a convincing analytical expression to describe the dependence of frequency $1/f$ noise on V_0 (and the transistor parameters), especially close to the start-up conditions. However, experimentally we have systematically observed that the largest SNR for measurements performed in a frequency bandwidth strongly affected by the $1/f$ noise is obtained for an oscillation voltage just above the start-up condition. For larger supply voltages, the $1/f$ noise increase is larger than the decrease in the thermal noise. Additionally, due to the larger B_1, the signal amplitude can also decrease due to saturation (see Eq. 8.2).

Table 8.3 – Oscillators performance summary.

Parameters	10 GHz osc.	20 GHz osc.
Supply voltage (V)	0.9	1.8
oscH and *oscL* voltage (V)	-	0.894
varL voltage (V)	-	-0.429
varH voltage (V)	-	-0.408
Supply current (mA)	6.18	5.6
oscH and *oscL* current (mA)	-	7.1
varH and *varL* current (mA)	-	0
Total power (mW)	5.6	16.4
Oscillation freq. (MHz)	10111.37	20000 [1]
oscL rest freq. [2] (MHz)	-	19437 [1]
oscH rest freq. [2] (MHz)	-	19232 [1]
Oscillators freq. difference (MHz)	-	204.58
Freq. error after power ON [3] (kHz)	25	500
Field. error after power ON [3] (μT)	1	18
Freq. stabilisation time (min)	60	120
Freq. variation after stab. (kHz)	10	50
Freq. variation after stab. (μT)	0.4	1.8
Noise floor(Hz/Hz$^{1/2}$)	3	35

[1] The 20 GHz oscillator has no direct frequency output. As a consequence, the oscillation frequency cannot be measured. The reported oscillation frequency is computed measuring the magnetic field assuming an effective $\gamma = \gamma_{\mathrm{BDPA}} = 28.02$ GHz/T (as reported in Ref. [95]).

[2] The rest oscillator frequency is measured with *VarL*=*VarH*=0 V.

[3] The power ON time is about 10 min, it corresponds to the power supply warming time to deliver stable power.

8.9 Ramp rate effect

The oscillator frequency variation as a function of the applied magnetic field has a dispersive shape [121] as shown in Fig. 8.11. For this reason, we define the resonance linewidth as the distance in field between the maximum and the minimum of the signal (i.e., the peak-to-peak distance).

For the 10 GHz oscillator, the marker signal is affected by the ramp rate within 361.005±0.005 mT (i.e., an effective $\gamma/2\pi = 28.01$ GHz/T for a frequency of 10.111 GHz comparable to the BDPA gyromagnetic ratio within the measurement system uncertainty) as shown in Fig. 8.12a.

For both the 10 GHz and the 20 GHz sensors the linewidth variation is within ±20 μT, as shown in Fig.8.12a and 8.12c. However, a significant change of the field marker position (about 88 μT/(T/s)) was measured for the 20 GHz oscillator (see Fig. 8.12c). A much smaller change (about 2.3 μT/(T/s) was observed also for the 10 GHz. This effect is presumably due to the

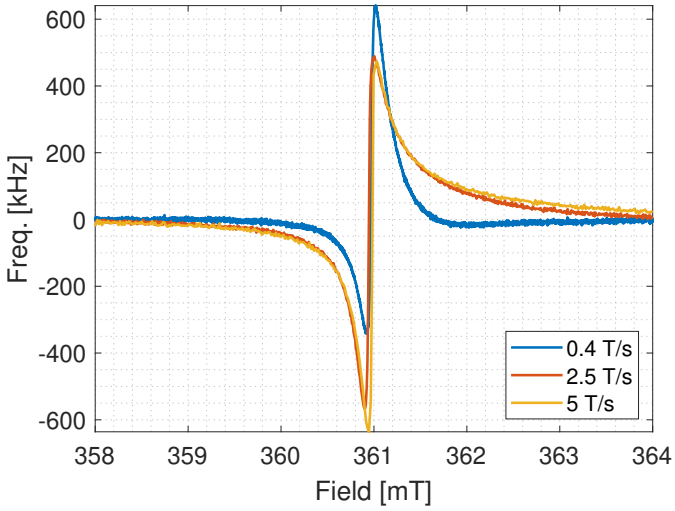

Figure 8.11 – 10 GHz sensor signal from the AC output for three field ramp rate of 0.4 T/s (blue curve), 2.5 T/s (red curve) and 5 T/s (yellow curve).

induced electromotive forces that change the varicap tuning voltage and the supply voltage of the oscillators ($oscL$ and $oscH$), which determine a variation of varicap capacitance and of the effective capacitance of the integrated cross-coupled transistors, and finally, of the oscillation frequency. The effect is significantly smaller for the 10 GHz oscillator probably because it has no varicaps.

However, we measured a variation of the oscillation frequency (Fig. 8.13c) due to the induced electromotive forces proportional to the field ramp rate (Fig. 8.13b) of 65.7 kHz/(T/s) (i.e, 2.3 μT/(T/s)) as shown in Fig. 8.13d. On the DC output, at high ramp rate, the EPR signal is attenuated as shown in Fig. 8.13c due to the low pass filter of 8 Hz but presents on the AC ouptut as shown in Fig. 8.11.

Figure 8.13c shows also no effect of the field strength on the oscillation frequency in static field conditions (i.e., before the field ramp with $B_0 = -50$ mT and after the ramp with $B_0 = 392$ mT). This indicates that the Ni layer on the bounding pads does not affect the field around the oscillator area.

8.10 Gradient effect

For the 10 GHz oscillator we measured a broadening of the line width by 39 μT/(T/m) (see Fig. 8.14b), while no measurable effect is observed for the 20 GHz oscillator. We measured a reduction of the amplitude (in Fig 8.14a) by 77 kHz/(T/m) for the 10 GHz oscillator and 52 kHz/(T/m) for the 20 GHz oscillator. The line broadening and signal reduction for the 10 GHz and 20 GHz oscillators appears at much higher gradient with respect to the 3 GHz resonator. This behaviour is consistent with the size of the employed samples, which are of 450 μm (for the 3 GHz resonator), 170 μm (for the 10 GHz oscillator), and 60 μm (for the 20

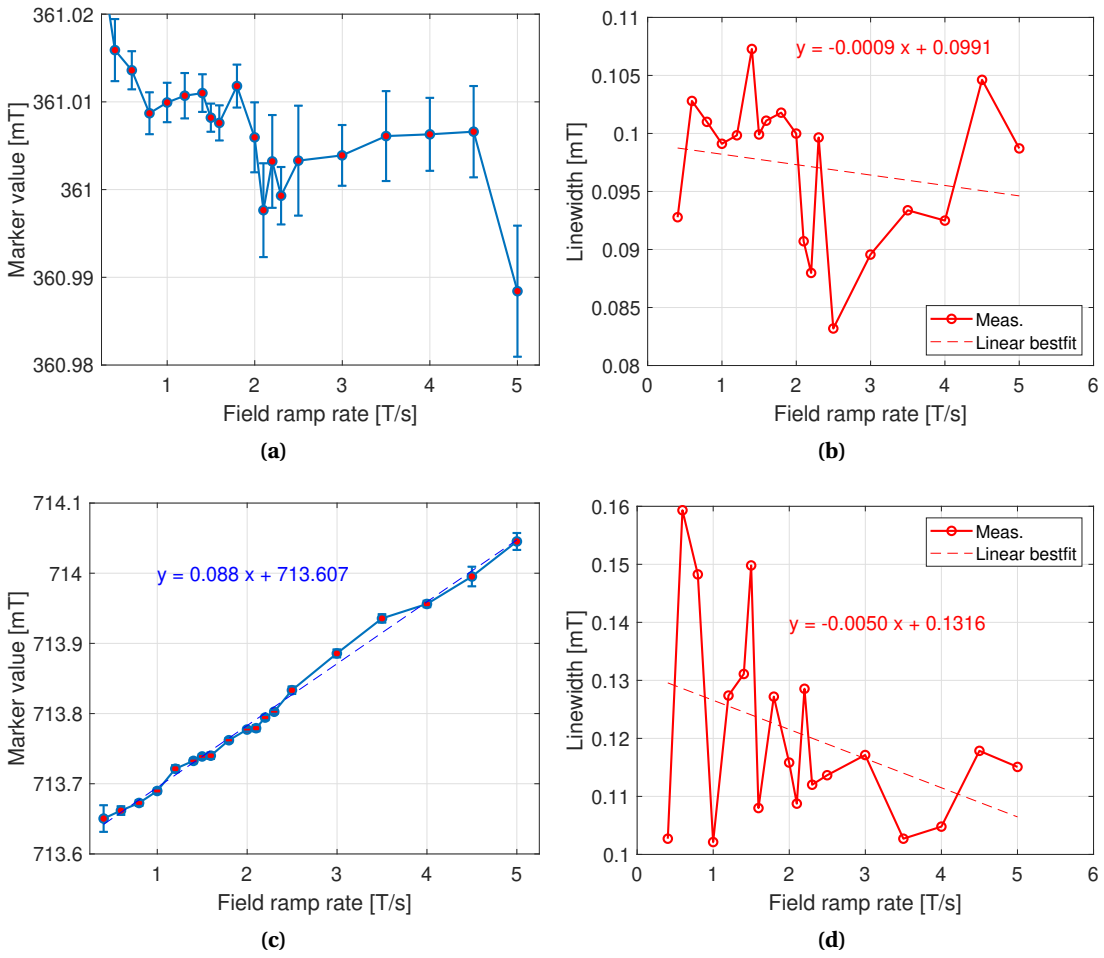

Figure 8.12 – Field ramp rate effect on the 10 and 20 GHz oscillators. (a) Field value for the 10 GHz sensor. (b) Linewidth for the 360 mT EPR sensor. (c) Field value for the 20 GHz sensor. (d) Linewidth for the 710 mT EPR sensor.

GHz oscillator).

Considering a minimum SNR=10 dB (i.e., an amplitude ratio of a factor three) and a frequency bandwidth of 160 kHz, the marker signal for the 10 GHz and 20 GHz sensors can be measured up to a gradient of about 12 T/m.

8.11 Summary of results

The Table 8.4 summarizes the main results obtained with the two oscillator sensor types.

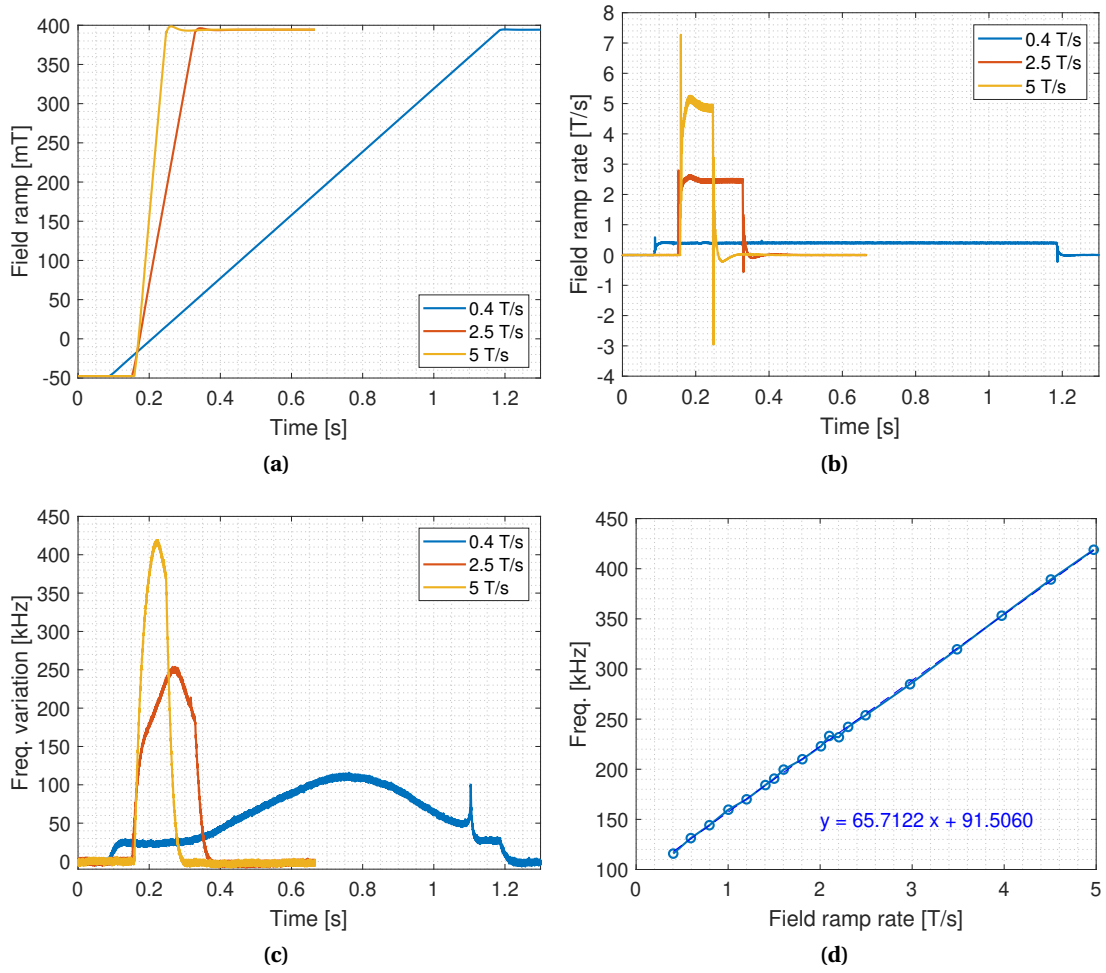

Figure 8.13 – Oscillator sensor ramp rate effect on the DC output for three field ramp rate of 0.4 T/s (blue curve), 2.5 T/s (red curve) and 5 T/s (yellow curve). (a) The field ramp profile. (b) The field variation $\dot{B}$. (c) The PLL DC output. (d) The correlation between the oscillation frequency versus the Bdot.

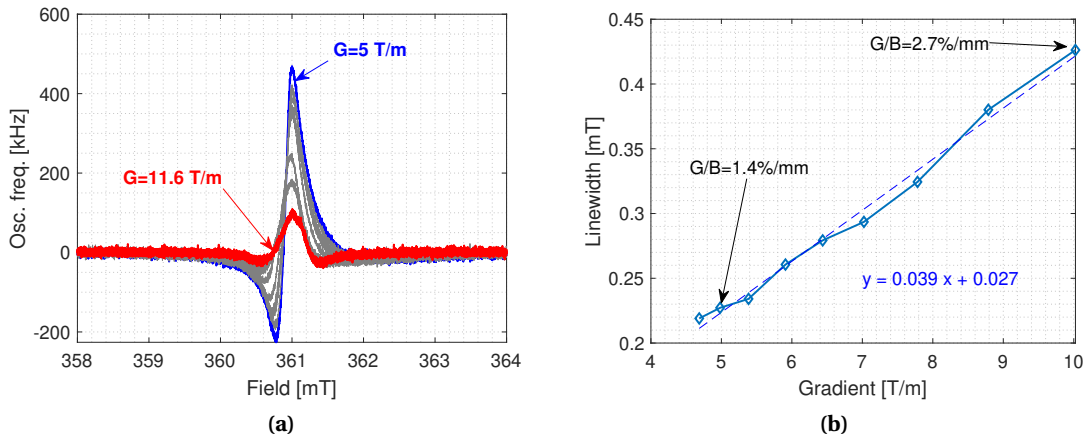

Figure 8.14 – Gradient effect EPR oscillator sensor. (a) On the 360 mT EPR sensor marker signal. (b) On the 360 mT EPR sensor linewidth.

Table 8.4 – EPR oscillator sensors summary.

Parameters	360 mT oscillator	710 mT Oscillator
Operating frequency (MHz)	10111.37	20000 [1]
B_m (mT)	361.01	713.65
B_m tuning range (mT)	-	660-720
Linewidth (μT)	97	121
Effective γ (GHz/T)	28.01±0.01	28.02 [1]
Sample volume (μm^3)	1.2×10^6	0.07×10^6
$\dot{B}$ sensitivity (μT/(T/s))	0	88
Gradient sensitivity (μT/(T/m))	39	0
Maximum gradient (T/m)	12	>12
Maximum field inhomogenity G/B_m (m^{-1})	25	at least 17
Field direction sensitivity ψ (μT/°)	<1	<1
Sensor sensitivity (Hz/T)	31.7×10^9	17.2×10^9
Noise floor ($Hz/Hz^{1/2}$)	3	35
Resolution ($nT/Hz^{1/2}$)	0.095	2
Bandwidth (kHz)	160	160
Integrated resolution (μT_{RMS})	0.04	0.8
SNR (-)	267	32

[1] The 20 GHz oscillator has no direct frequency output. As a consequence, the oscillation frequency and the effective γ cannot be measured. The reported oscillation frequency is computed measuring the magnetic field with an NMR magnetometer and an induction coil (see Sec. 3.1) and assuming an effective $\gamma = \gamma_{BDPA} = 28.02$ GHz/T (as reported in Ref. [95])

Part III

Experimental validation of the FMR sensors during the operation of particle accelerators

9 Case study on the PS accelerator

In this research, we used the PS reference magnet to validate the performance of the 36 mT FMR sensor.

9.1 The PS B-Train system

The PS is a strong-focussing combined-function synchrotron with a circumference of 628 m. It operates at CERN since 1959 and accelerates particles from 1.4 GeV (2 GeV in 2021) up to 26 GeV, when receiving proton the beam from the PSB. The PS accelerates also heavy ions (typically Pb^{+54}) from the LEIR at 0.072 GeV/nucleon to 5.9 GeV/nucleon. Due to its central position in the CERN's accelerator complex (as shown in Fig. 1.1) and its energy covering range, the PS has the highest variety of beam user requests. For this reason, the field performance (i.e., B-Train system) and its operation constraints are the highest.

The ring is composed of hundred main bending magnets called "Main Unit" (MU). One supplementary unit is installed outside the radiation protection bunker. This magnet (MU-101) is used as reference for the magnetic field measurements. Each magnet weights 33 tons, 5 m long and produces a main dipole field of 1.26 T and a main quadrupole field of ±60 T/m with 5500 A for a 26 GeV extraction plateau. One magnet unit is composed of ten steel blocks of 417 mm long of *open* and *closed* types as shown in Fig.9.1a, five blocks are assembled in focusing side (F-side), and five blocks in defocusing side (D-side). Therefore, the integrated quadrupole field is almost zero, while having a focusing effect of the beam.
Four types of magnet configurations, *R* (35 in the machine), *S* (15 in the machine), *T* (35 in the machine), *U* (15 in the machine) are installed in the accelerator. They alternate the F and D side placed inside the closed orbit (called "*inside*" units) for the *U* and *T* and outside the closed orbit (called "*outside*" units) for the *R* and *S* with respect to the accelerator center as shown in Fig. 9.1b. A typical accelerator lattice section is shown in Fig. 9.1c.

Each magnet unit is equipped with 6 coil excitation circuits as shown in Fig. 9.2.

- **One main coil circuit** used to produce the main dipole and main quadrupole compo-

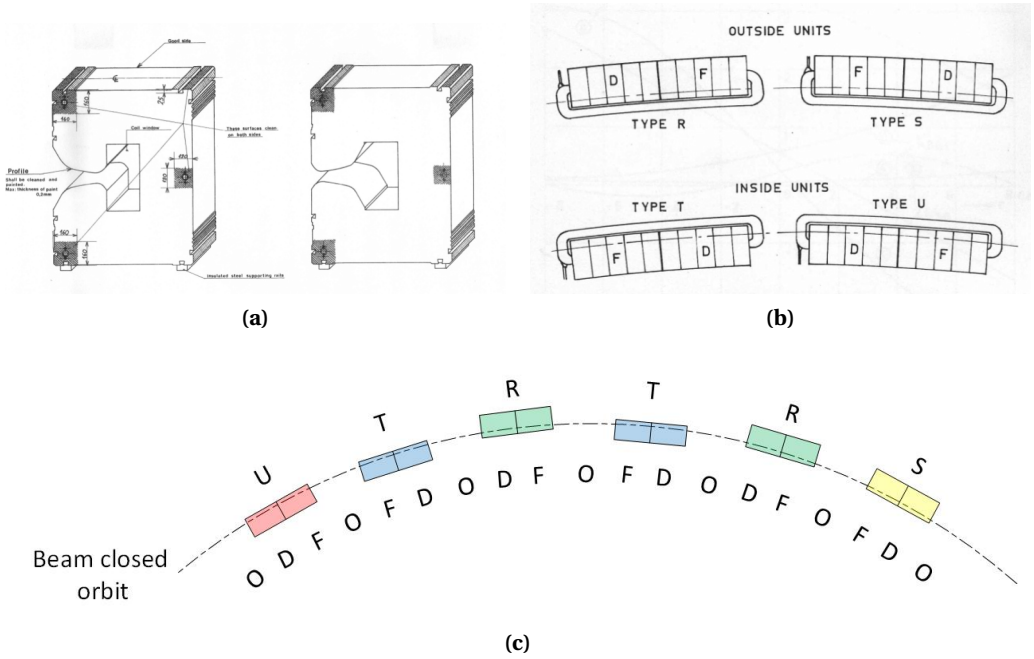

(a) (b) (c)

Figure 9.1 – PS main unit magnet [122, 123].(a) PS magnet *open* and *closed* blocks.(b) PS magnet unit types. (c) PS magnet lattice with the pattern is "FOFDOD" which alternate the difference magnet type from the left to the right of one of the machine section:U-T-R-T-R-S.

nents;

- **One figure-of-eight-loop circuit (F8L)** used to unbalance the main quadrupole component between the two half-units [124]; and
- **four pole-face windings circuits (PFW)** used to produce large quadrupole, sextupole and octupole components to adjust the *tune* and *chromaticity* impacted by the magnetic field saturation when reaching the extraction region. The four circuits are called "Defocusing Wide", "Defocusing Narrow", "Focusing Wide" and "Defocusing Narrow" [125].

As previously mentioned, the main field produced by these magnets is a combination of a dipole and a quadruple as shown in fig.9.3. It implies a strong non-uniform field by about 4.6 m^{-1} in the horizontal direction.
A high gradient, a accuracy of about 5×10^{-4} and a reproducibility of about $\leq 5 \times 10^{-5}$ at injection limits the choice of possible field sensors. The legacy B-Train marker sensors (i.e., the peaking strips) were used more that 40 years without any reported problem on the sensors itself [127]. However, the power supplies, electronics and controls had common and expected failures. The peaking strip measures the field at 4.98 mT, an upgrade was developed for reaching 40 mT but never used in operation.
As detailed in Ref. [47], for several reasons such as fabrication, controls and field marker levels, the ESR became the privileged solution for replacing the peaking strips in the framework of PS B-Train consolidation for the high luminosity injector upgrade. We recall that prototypes of FMR sensor based on YIG filter were used successfully (between 2015 to 2018). The field

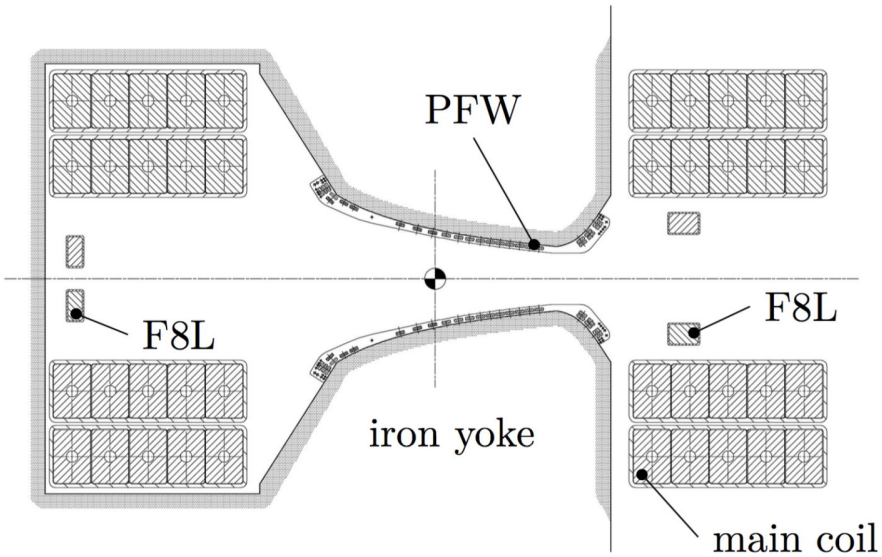

Figure 9.2 – PS excitation coil circuits [123, 126] of a closed unit.

marker level was at 49.5 mT and ensured the highest field reproducibility before the injection level (68.5 mT for the heavy ion $^{208}Pb^{54+}$ and 101.4 mT for the proton). Nevertheless, for the heavy ion beams we measured field instabilities on the injection plateau caused by enabling of the power converter field regulation loop (the converter in voltage-regulated before the field marker). Therefore, we decided to use a lower field marker level. The 36 mT ESR sensor is a trade-off between the proton and ion injection levels.

9.2 Reproducibility measurements of the 36 mT FMR sensor

The measurement of the reproducibility was performed by comparing the FMR sensor to the legacy sensors.
We installed two calibrated 36 mT FMR sensors in the PS reference magnet (MU-101) as shown in Fig. 9.4, in the forth block of the F-side and in the forth block of the D-side. They were positioned on the closed orbit by mechanical references. Due to the accelerators complex operation constraints, we did not use the FMR sensors in the online B-Train system, but we connected them to an offline system identical to the operational system. We used triggers of the operational YIG filters and peaking strips markers (The legacy B-Train system markers) for the comparison. The legacy markers were fully validated during operation with beam and show a reproducibility better than 5 μT. For measuring the reproducibility, we used the operational induction coils $D3$ and $F3$, via a buffer amplifier, previously installed and calibrated in the magnet.
The field variation ΔB measured by $D3$ and $F3$ is taken as a reference, where the initial value ($\Delta B = 0$ T) corresponds to the average field over the total number of measurements.

The measurements were performed on cycles called "*EAST*" as shown in Fig. 9.5 due to its

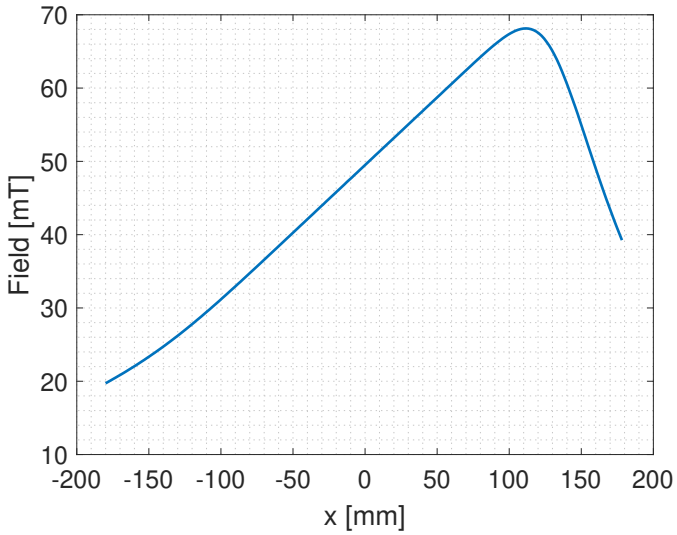

Figure 9.3 – PS magnetic field profile of a closed unit at the legacy FMR field marker (YIG filter) level of 49.5 mT, $x = 0$ mm is the beam closed orbit. The maximum field corresponds to the position where the magnet aperture is minimum as shown in Fig. 9.2.

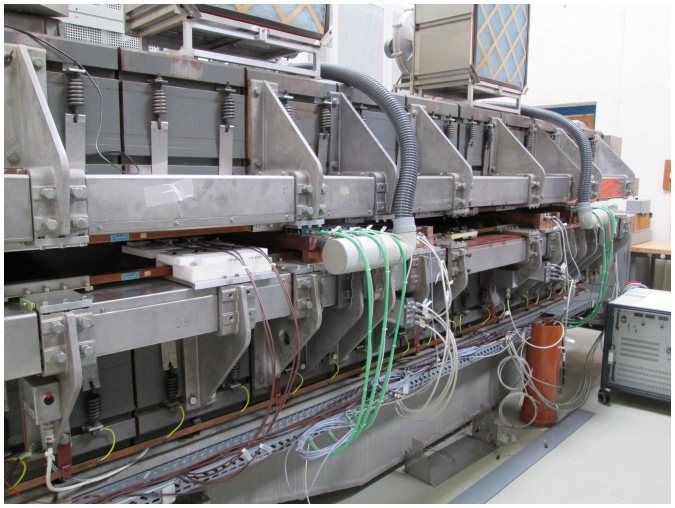

Figure 9.4 – PS reference magnet MU101 is a T-type unit, the D-side, on the foreground, is composed of five open blocks and the F-side, on the background, is composed of five closed blocks, the FMR sensor are installed inside the blocks #4 3rd trail on the close orbit and on the mid-plane of the magnet gap. The peaking strips are installed on the blocks #3 with its cooling system for an operation at 40 mT and the induction coils on the blocks #2.

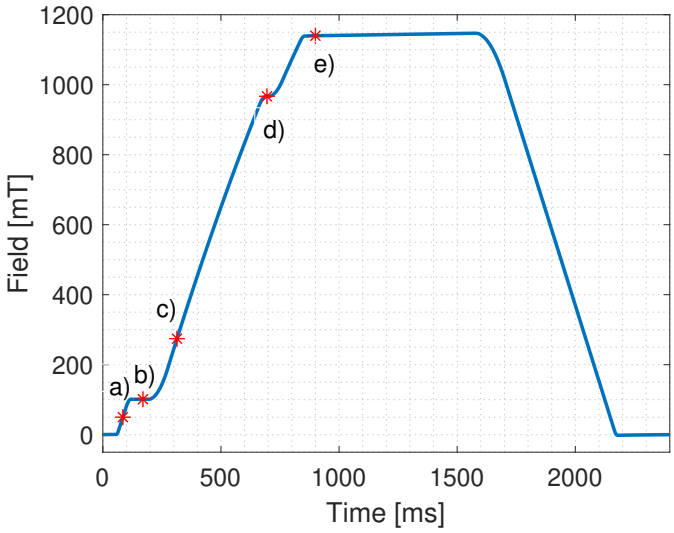

Figure 9.5 – PS reproducibility cycle on *EAST* (proton beam), a) is the resonator sensor marker time at roughly 80 ms equivalent to a marker field of 36 mT. b) is the beam injection time at 170 ms (101.35 mT) and the RF feedback loops activation, c) is the relativistic gamma transition (i.e., non-relativist to relativist particle transition) time at 314 ms (274 mT), d) is the first "fast" extraction time at 695 ms (967 mT, that is, 19.4 GeV) for the n-ToF experiments and e) is the second "slow" extraction time at 900 ms (1140 mT, that is, 23 GeV) for the east experimental area.

large occurrence rate during the measurement period. This cycle has two beam recipients, a side beam is sent to the *n-ToF* target by a first extraction, while in a second extraction, the main beam is sent to the east experimental area (in Fig. 1.1). Figure 9.6 shows two typical supercycles with the different position and occurrence of the *EAST* cycles. We define as $N-1$, the pulsing cycle just before the *EAST* cycle, and $N-2$ the pulsing cycle two occurrences before the *EAST* cycle.

The fluctuation of the magnetic history caused by previous cycles have a relevant influence on the field value. Those cycles affect the measured field value before the marker by a variation of 7.8 mT, as shown in Fig. 9.7a. Six subsets of marker values can be determined from Fig. 9.7a, which correspond to the $N-1$ cycle type. The hysteresis of the $N-1$ cycle and its remanent field after the ramp down affect the field variation. For a given $N-1$ cycle, ΔB decreases typically to 0.2 mT. This remaining difference is due to the $N-2$ cycle fluctuation. Its effect is particularly visible on the cycle called "*ZERO*". This cycle is used to fill empty basic period slots (of 1.2 s) in the supercycle when the experiments do not need beam, and maintain the power converter capacitors bank pre-loaded. The *ZERO* cycle has a flattop at only 50.86 mT. The measured field variation of this cycle is 0.77 mT, as shown in the Fig. 9.7b. As the maximum field flattop of the *ZERO* cycle is far from the saturation, the magnetic history is almost unchanged. Therefore the dominant effect of the field variation is due to the $N-2$ cycle.
Therefore, for the reproducibility measurement we considered only the cycles with the same $N-1$ and $N-2$ cycles. The magnetic history effect from the third previous cycle ($N-3$) are

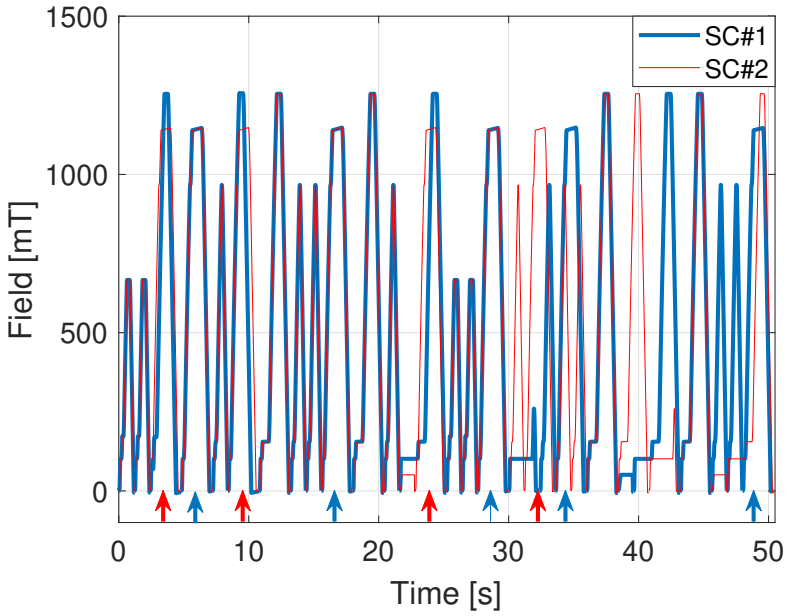

Figure 9.6 – Two PS supercycle examples in blue and in red, the arrows point the *EAST* cycles in the sequence. The number, position and therefore its previous magnetic cycle are different.

considered negligible, except for special operation conditions such as two or more *ZERO* cycles before *EAST* cycles. In addition, few cycles were excluded such as the $N = 1087$ and $N = 1644$ (in Fig. 9.7a) due to other operation features.
In the aftermath, from a total cycle number of 2676 only a subset of 1188 was kept to perform the reproducibility analysis. This population was large enough for statistical computation.

As shown in Fig. 9.8, the 36 mT FMR sensor reproducibility for a total of 1188 cycles is very close to a Gaussian with a standard deviation of $\sigma_{B_{\mathrm{m}}^{\mathrm{D}}} = 4.2\ \mu$T and $\sigma_{B_{\mathrm{m}}^{\mathrm{F}}} = 5.2\ \mu$T for the D-side and F-side, respectively. This corresponds to a relative reproducibility of 5×10^{-5} at injection, which is within the PS requirement. We measured similar differences with the YIG filter and the peaking strips. The larger reproducibility on the F-side $\sigma_{B_{\mathrm{m}}^{\mathrm{F}}}$ is caused by a field distribution change due to a different operation of the PFW correction circuits between the D-side and F-side.
We performed the same measurements on other four cycle types. The results show that the reproducibility is comparable within 0.6 μT.

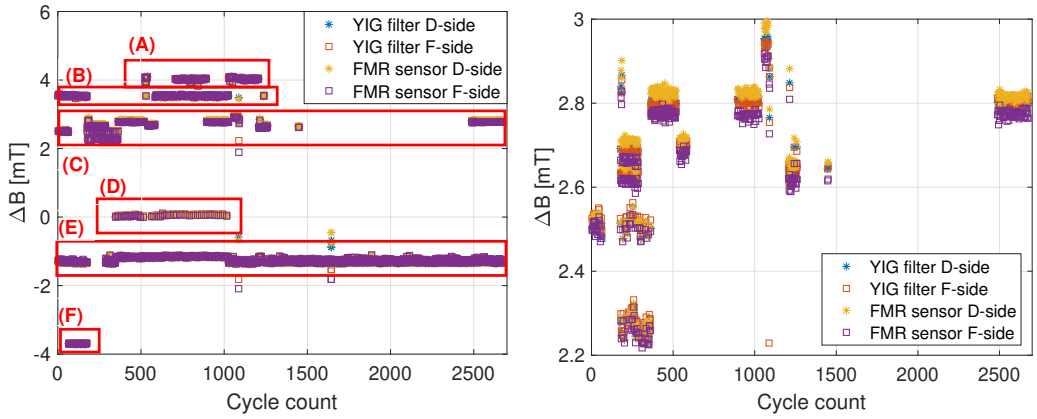

Figure 9.7 – PS field markers trigger. (a) for the YIG filter and 36 mT FMR sensor on the two magnet sides. The different groups represented by red rectangles correspond to the first previous $(N-1)$ cycle. The (A) group is *LHC_INDIV* cycles, (B) *MTE* cycles, (C) *ZERO* cycles, (D) *EAST* cycles, (E) *TOF* cycles and (F) *LHC_ION* cycles.(b) Zoom-in on the *ZERO* cycle values (C).

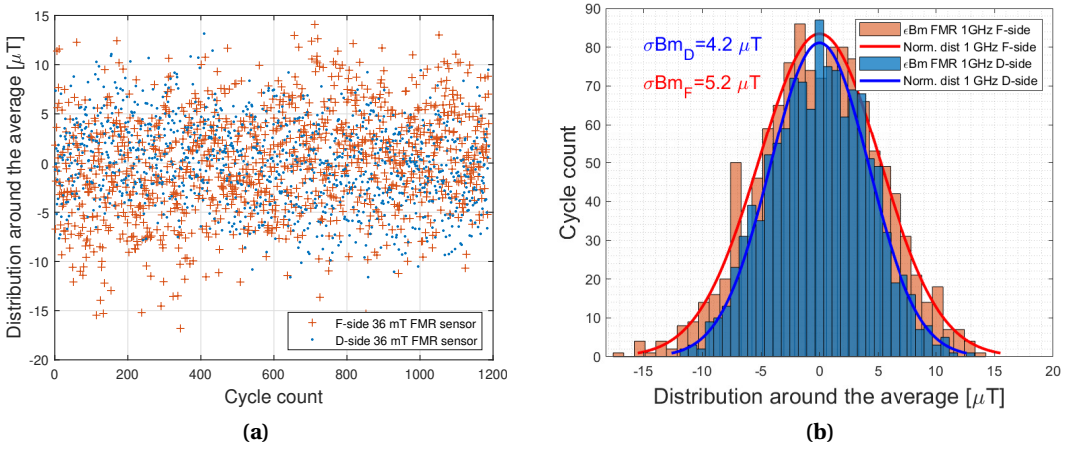

Figure 9.8 – PS 36mT FMR marker reproducibility over 1188 *EAST* cycles. (a) The cycle sequence. (b) The distribution.

10 Case study on the LEIR accelerator

We used the LEIR accelerator to validate the performance of the 106 mT FMR sensor and the B-Train system in operational conditions.

10.1 The LEIR B-Train system

The LEIR is a synchrotron with a circumference of 78 m in operation at CERN since 2005, when it replaced the older ring Low-Energy Antiproton Ring (LEAR) re-using most of its components. The LEIR is designed for beams of heavy, highly ionized species such as $^{208}Pb^{54+}$, which is accelerated from 4.2 MeV/nucleon to 72.2 MeV/nucleon, $^{40}Ar^{11+}$ (used in 2015) and $^{129}Xe^{39+}$ (used in 2017) [130]. The ring includes four main 6.4 m long, 90° bending magnets, each weighing 60 tons and composed of 6 steel blocks of different lengths. These magnets produce a dipole field of 1.15 T at 3300 A for the 72.2 MeV/nucleon extraction plateau.

Contrarily to all other B-train systems in operation at CERN, the LEIR machine does not have a dedicated reference main bending magnet for the field measurement (the only other exception is the AD, where however the measurement is not required). As a result, the sensors can only be installed in the ring dipoles (Fig. 10.1). The legacy system was based on one operational and one spare induction coil installed in the BHN30 and BHN20 dipoles respectively, tightly wedged between the vacuum chamber and the bottom magnet pole. No field marker was included to provide the integration constant for the coil voltage, which made the legacy B-train blind to magnetic hysteresis effects. The coil inside the BHN20 developed shortly after installation an electrical fault, which was never repaired since that would have required opening up the whole magnet.

Therefore, after a detailed study involving operation, vacuum, handling and magnet teams, it was decided to include in the new system a new set of coils and field markers located in the accessible fringe field region of the magnets. This choice lowers considerably the cost of installation and ensures easy maintainability of the system in the long term, at the risk of a

This chapter is reproduced with changes from [128, 129].

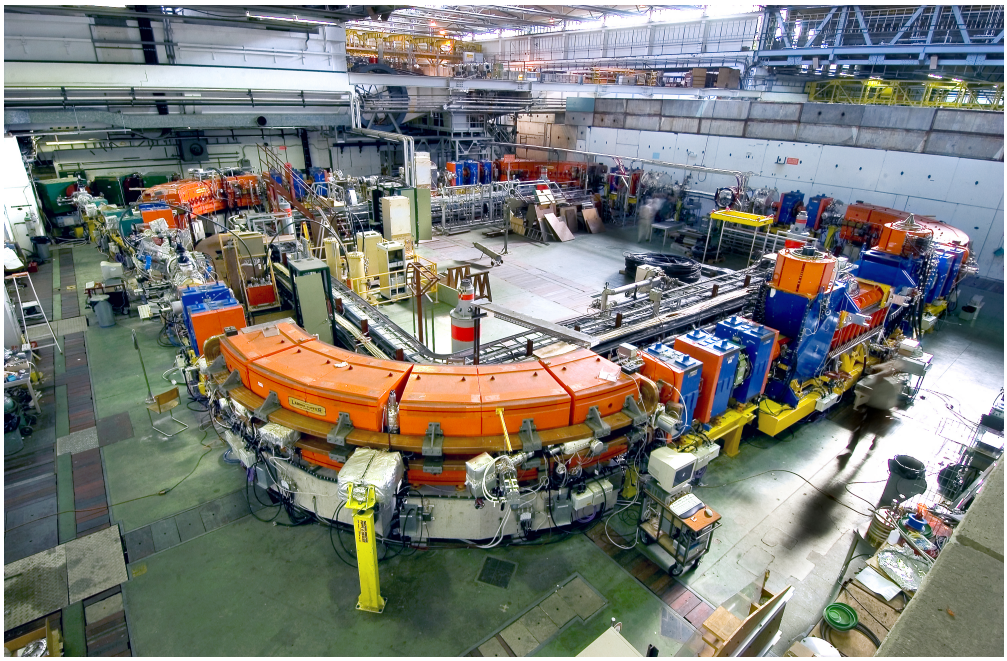

Figure 10.1 – LEIR accelerator [131] where the orange magnets are the main bending dipoles (BHN10 in the foreground and BHN30 in the background).

slight degradation of measurement accuracy due to non-linear effects.

Two identical assemblies including one induction coil and two field markers have been installed in BHN20 and BHN30 on the mid-plane of the gap, in the outer region just outside the vacuum chamber and the surrounding bake-out insulation, as shown in Fig. 10.2. Only one of the field markers has been used for operation, the other being a hot spare. The position of the sensors was optimized on the basis of the results of a static Opera™ FE simulation, shown in Fig. 10.3). They have been mounted at a radial distance respect to the closed orbit $x \approx 200$ mm, where the ratio between the field at extraction and injection (Fig. 10.3b) is approximately equal to the ratio at $x = 0$ mm. In this region the radial gradient is, in relative terms, about 10 m^{-1} at all field levels.

The induction coils are 102 mm long, have an effective area of 0.60367 m^2 and are positioned tangentially to the ring circumference. At both ends of each coil there is a 106 mT FMR sensor. The nominal working point of the markers is 106 mT, with a gradient of 1.2 T/m. According to FE calculations, this corresponds to 252 mT at the closed orbit, that is, approximately 20 mT lower than the nominal injection field for the beam used in the tests, that is 272.1 mT. These settings ensure that the FMR resonance is crossed at a dB/dt adequate to generate a strong detectable signal, while at the same being as temporally close as possible to beam injection, when the highest possible field measurement accuracy is required.

Due to their external placement, the magnetic sensors are exposed to the temperature fluctuations in the ring hall, which is in a surface building without air conditioning. The observed

fluctuations can be very large, up to 15°C in a single day and 15 °C from winter to summer. For this reason, a temperature regulation system (shown in Fig. 10.2b and in Fig. 10.2c) was installed to keep the assembly at 35±0.1 °C, which based on calibration tests should ensure marked field errors within ±4 μT.

The B-Train electronics racks are installed outside the concrete walls of the bunker with the cable distance to the sensors of about 40 m. Therefore we modified sightly the detection architecture as shown in Sec. 6.1 by placing the 180° hybrid coupler close to the 106 mT FMR resonator and adding an RF amplifier of 21 dB (ZX60-83LN-S+, Mini-Circuits) on the returned line.

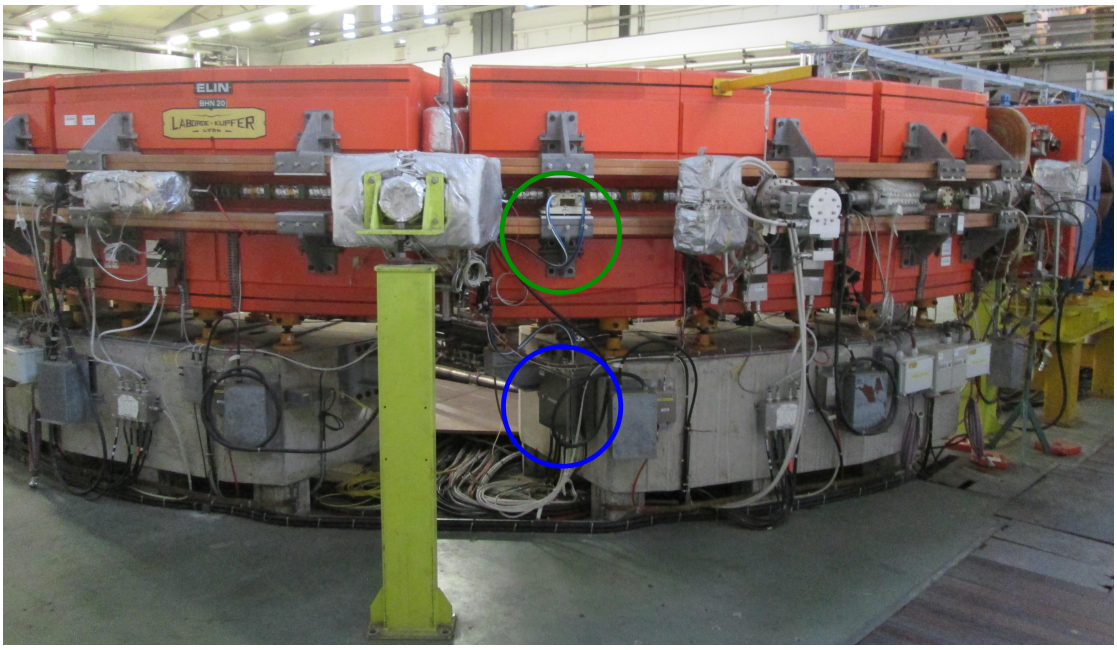

(a)

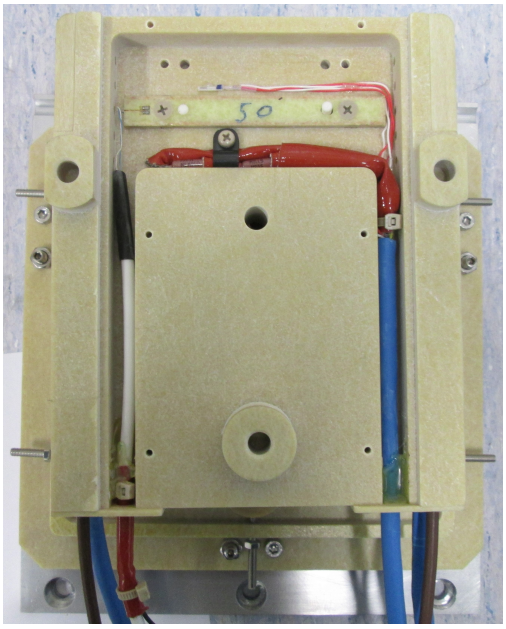

(b)

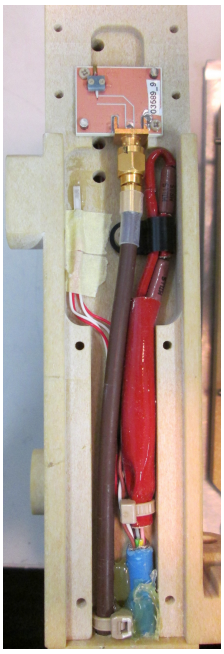

(c)

Figure 10.2 – LEIR B-Train sensors.(a) The new B-Train sensors installed on the BHN20 (spare) and BHN30 (operational) magnets in front of the block#4. It includes the sensors support placed on the side of the vacuum pipe (the green circle) and and the front-end RF equipment box placed below the magnet (the blue circle). (b) The induction coil on top of the sensor support (with cover removed). (c) FMR markers on each side of the sensor support (with covers removed). Close to each sensor, a heating resistor and a PT100 temperature sensor are installed for the temperature regulation.

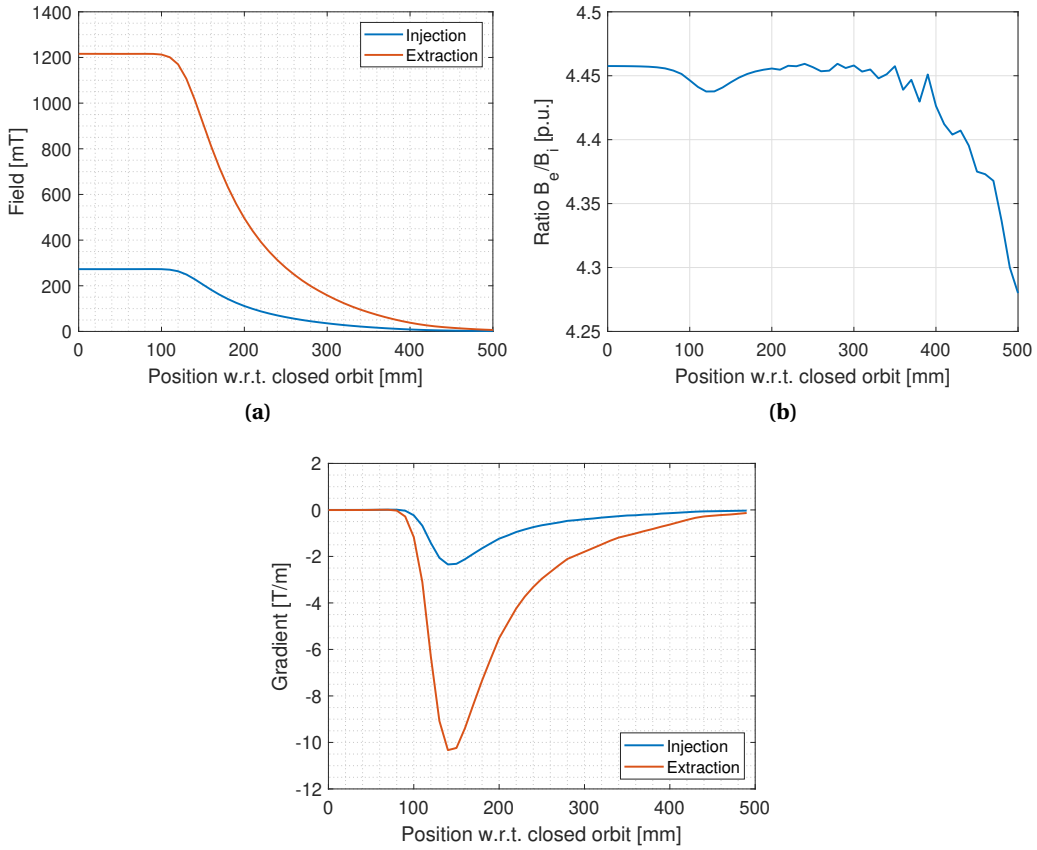

Figure 10.3 – FE simulation of LEIR main dipole.(a) Vertical field vs. outwards radial distance from the beam closed orbit, at injection (blue curve) and at extraction (red curve).(b) Ratio between the field at extraction and at injection. (c) Radial gradient vs. outwards radial distance from the beam closed orbit, at injection (blue curve) and at extraction (red curve).

10.2 Preliminary B-train comparison

Some preliminary tests were carried out during the summer of 2018 to compare directly the performance of the old and new B-trains:

- On the operational cycle called "*EARLY*" (12 June 2018): field measurements, measurements of the radial beam position and the frequency correction of the RF radial loop, beam intensity measurements

- On a clone of the cycle "*NOMINAL*" (08 August 2018): tomoscope measurements

Since the two B-train systems are independent they can run simultaneously, which allows a continuous comparison of the respective outputs. These were fed alternately to the LLRF and the beam current transformer controls in order to evaluate any possible impact on beam behaviour.

10.2.1 Measured field

The two field measurements are shown as a function of time in Fig. 10.4a, while their difference $\Delta B = B_{\text{new}} - B_{\text{legacy}}$ is shown in Fig. 10.4b. The peak difference is about −1.3 mT (i.e. about 10^{-3} of the peak field) and is observed at the time of maximum $\frac{dB}{dt}$ on the ramp-up. This suggests that the difference is mainly due to edge eddy currents being closer to the new sensor location than the center of the gap, where the legacy coil is installed. A zoomed-in comparison of the two B-trains at injection is given in Fig. 10.4c, which clearly shows how the switch to White Rabbit distribution improves the integrated resolution from ±10 μT to ±0.2 μT. The 50 μT offset between the two curves is due to the absence of a field marker in the legacy system, leading to a calibration error.

The correlation of new to legacy B-train is plotted in Fig. 10.4d and is given by the following linear relationship

$$B_{\text{new}} = 0.9997 \times B_{\text{legacy}} - 0.94 \text{ mT} \tag{10.1}$$

with a RMS residual of about 50 μT, well above measurement noise. While the large offset difference is fully expected, due to the lack of a field marker in the legacy system, the correlation factor inferior to one suggests that the gain of the acquisition chain new B-train is underestimated and should be adjusted accordingly.

The transfer function of the dipole magnet, that is, the ratio between the field measured by the new B-train and excitation current, is represented in Fig. 10.5. On the up-ramp, instead of the common high-field drop due to saturation, we can observe a uniform decrease of about −0.8% between injection and extraction. This decrease, observed in other strongly curved magnets (such as ELENA's bending dipoles [5]), may be attributed to a combination of factors including error on the gain and offset of the measured field, or a staggered onset of saturation in different parts of the magnets.

10.2.2 Radial Position

The impact of the new B-train on the overall beam performance is best evaluated via the mean radial position and the frequency correction contribution of the radial loop, shown in Fig. 10.6a and 10.6b. The largest frequency correction is about −2.0 kHz at 1300 ms into the cycle, which corresponds to a field error of −1.7 mT at 800 mT. This is about four times as high as the correction with the legacy B-train, however it remains well within the nominal capability of the radial loop, that is, ± 5 kHz. A few milliseconds before extraction the frequency correction drops in magnitude down to 500 Hz, which corresponds to 0.5 mT at 1150 mT.

Despite the field error, the mean radial position appears substantially more stable with the new B-train, with a systematic difference of 0.2 mm and the RMS noise level dropping from 0.37 to 0.10 mm, in all likelihood due to the improved resolution of the new B-train. Overall,

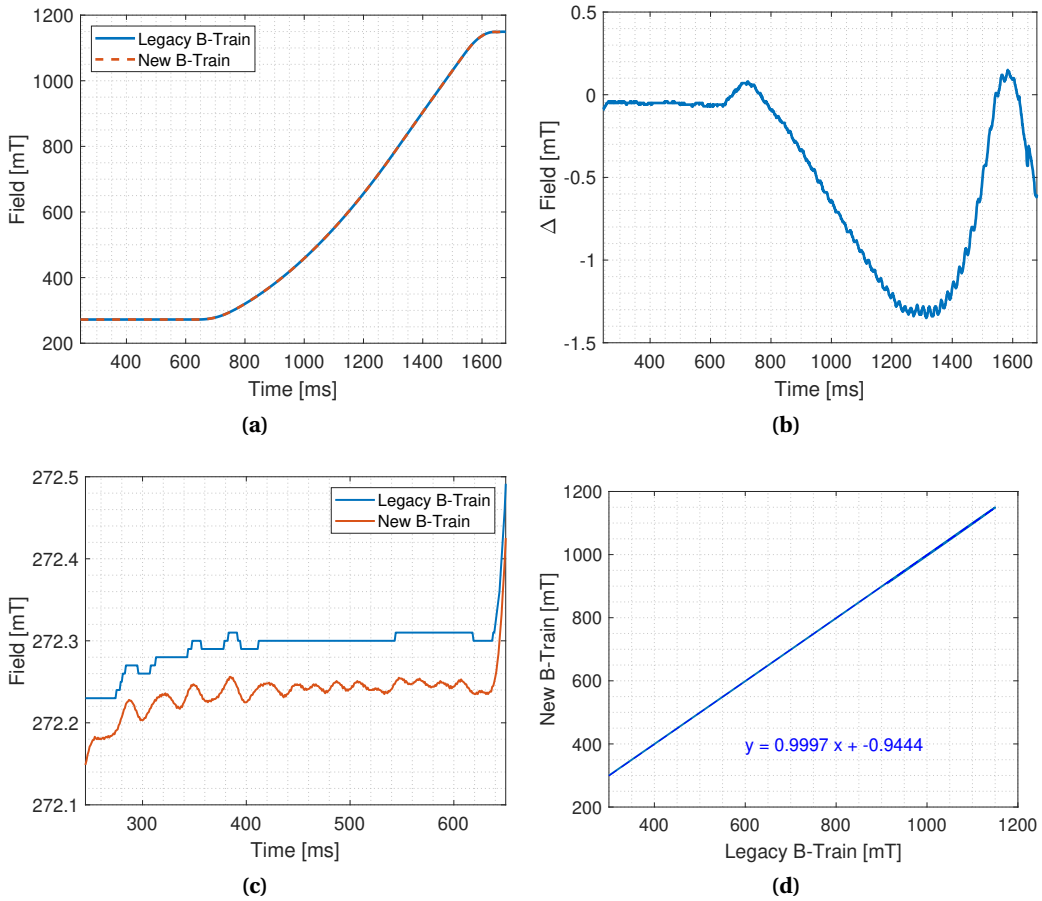

Figure 10.4 – LEIR B-Train systems difference on *EARLY* cycle.(a) The legacy system in solid line and the new B-Train field in dash line. (b) The difference between the new B-field and the legacy B-field.(c) Zoom-in of the field at injection for both B-Train system.(d) Correlation new versus legacy B-Train field.

the mean radial position remains well within ± 1 mm.

10.2.3 Beam intensity

The number of circulating particles with the legacy and the new B-train are shown in Fig. 10.7. The difference during injection is less than 10%, which is consistent with routinely observed fluctuations due to Linac3 intensity and beam losses. This measurement also validates transmission of the new WR B-train to the beam current transformer control system, which uses it to compute particle numbers previously shown in Eq. (1.7).

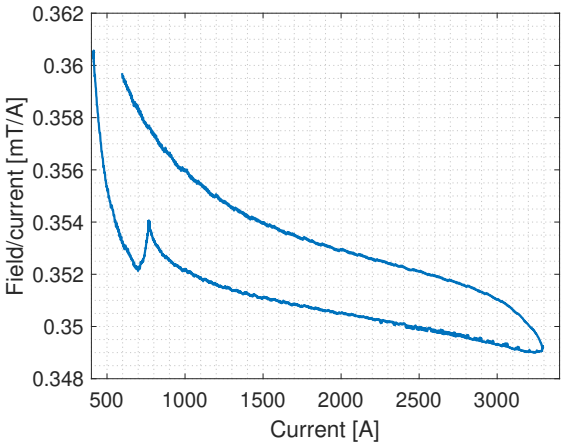

Figure 10.5 – LEIR main magnet (BHN30) transfer function.

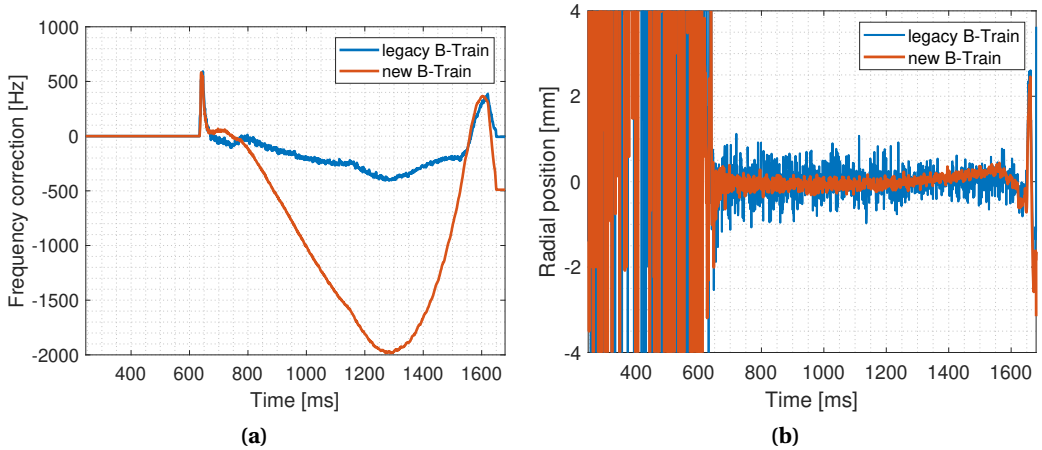

Figure 10.6 – LEIR beam radial effect on *EARLY* cycle.(a) RF radial loop contribution.(b) Beam radial position.

10.2.4 Beam profiles

Finally, the tomoscope Figure 10.8 shows beam phase space profiles measured on a *NOMINAL* cycle at extraction on 08 Aug. 2018 with the tomoscope with the legacy and the new B-Train. No appreciable impact of the new B-Train on the structure of the beam can be detected.

10.3 Reliability run results

A reliability run including a total of 68286 cycles was performed from August to December 2018, in order to validate on a statistical basis the sensors, electronics, controls and transmission parts of the B-Train system for the post Long Shutdown #2 (LS2) period of operation. The dedicated cycle used was a clone the operational *EARLY* cycle shown in Fig. 10.9. The accumulated number of cycles is plotted in Fig. 10.10, where one can see a pause between

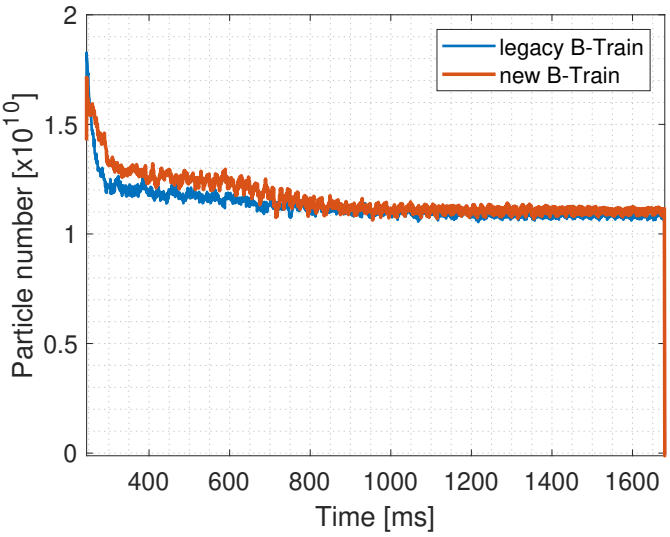

Figure 10.7 – LEIR particle count from the beam current transformer.

early September and mid-October that was due due to various operational constraints. Such a long run was possible thanks to a sufficient number of available machine development slots and, crucially, to the possibility of switching between the legacy and new B-Train systems on the fly using the Pulse-to-Pulse Modulation (PPM) function, which allows setting independent configuration parameters to each cycle type.

Whenever the super-cycle sequence allowed, a special calibration cycle without beam was inserted to carry out offset and gain correction of the PCIe integrator by applying a sequence of reference voltages (i.e., -8.75 V, 0 V and +8.75 V) to its input.

The overall stability of the new B-Train system was satisfactory throughout the run. A summary of the comparison between the old and the new B-train, including both the new operational and spare chains, is given in Table 10.1. The differences and stability of the three systems are discussed in detail in the sections below.

10.3.1 Stability at injection

On the *EARLY* cycle, injection begins at $t_{\text{inj}} = 245$ ms into the cycle, when the magnetic field attains a nominal value of 272.1 mT. The field measured by the new operational B-Train at $t = t_{\text{inj}}$ over the whole set of cycles is plotted in Fig. 10.11a, which shows an overall peak-to-peak variation of about 300 μT and a reproducibility of 40 μT, well within the tolerance of the machine. The reproducibility of the legacy and new spare B-train are closely comparable, being respectively 30 and 52 μT.

The air temperature in proximity of the magnet gap is plotted in Fig. 10.11b alongside the temperature of the B-Train electronic racks. The temperature variations are higher on the racks, which are close to the hall door, hence more exposed to the external environment. The

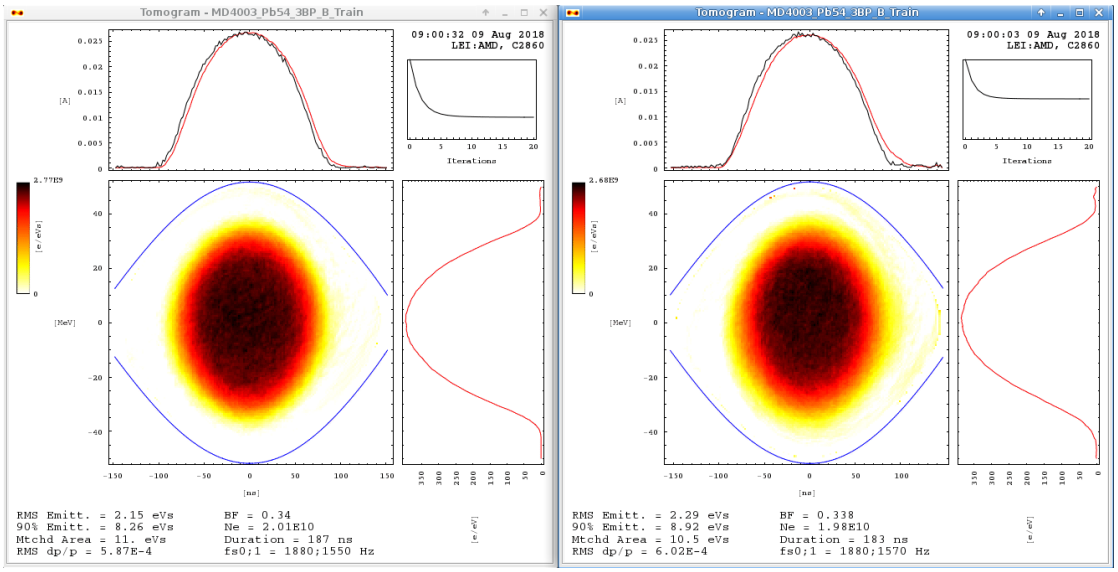

Figure 10.8 – LEIR tomoscope legacy versus new B-Train. LLRF feedback from: legacy system (left) and new operational system (right).

measured field is strongly correlated to the gap temperature, via a mechanism that is not clear at the moment. The correlation is especially evident in the well-visible daily periodic fluctuations, which correspond to sequences of about 2500 cycles. This temperature effect at beam injection is not visible with the legacy B-Train, since the system was started with a preset software marker. The correlation of field and temperature is show in Fig. 10.11c. The correlation coefficient is 19 μT/°C (or, in relative terms, 70 ppm/°C), in contrast with the value of −10 ppm/°C that would be expected from the thermal expansion of the magnet gap. This excludes any possible thermal effect on the geometry of the magnet, which at any rate could not follow such rapid variations due to its large mass. The correlation is much stronger with the gap temperature than with the temperature measured in the acquisition racks. This excludes any thermal effects on the acquisition electronics (which actually are corrected by the regular calibrations). We recall that the sensor assembly is thermally stabilized, which excludes a direct influence of ambient temperature on the readings. A possible error source may be related to small thermally-induced deformations of the sensor support, for example any rotation around the radial direction, to which the FMR sensor is extremely sensitive ($\psi = 368$ μT/° as shown in Sec. 6.4). Whatever the cause, if temperature correlation is subtracted from the data, the residual is essentially random noise with a standard deviation of 38 μT, that is, 1.41×10^{-4} relative to peak field (see the histogram in Fig. 10.11d).

A subset of the test data has been analysed separately to derive indications on the reproducibility of the FMR marker, as well as the correlation to the correction applied by the radial RF loop. The subset includes 1515 cycles within a narrow temperature range i.e. 24.3 ± 0.5 °C, in order to eliminate as much as possible the influence of thermal effects (this particular temperature was chosen to obtain a large subset). The field measured by the new operational B-Train at injection and the relative histogram are represented in Fig. 10.12b. The standard deviation is

Table 10.1 – LEIR B-Train field summary for the legacy and the new systems, both the operational and the spare. A lower number of cycles applies to the spare new system, due to development work going on in parallel with the tests. T_{mag} is the temperature of the BHN30 magnet, B^L is the field measured by the legacy system, B^N and B^S are the field measured by the new operational and spare system, and the subscripts i and e denote injection and extraction time.

Parameters	N. of cycles	Mean	Min.	Max.	Range	St. dev.
T_{mag} (°C)	68286	24.2	16.9	29.0	12.1	2.5
$B^L{}_i$	68285	272.20	272.16	272.28	0.12	0.03
$B^N{}_i$ (mT)	68286	272.1036	271.9480	272.2510	0.3030	0.0397
$B^S{}_i$ (mT)	36272	272.1151	271.9810	272.2380	0.2570	0.0524
$B^L{}_e$ (mT)	68285	1149.39	1148.78	1150.27	1.49	0.39
$B^N{}_e$ (mT)	68286	1148.6851	1142.4530	1149.6160	7.1630	0.3697
$B^S{}_e$ (mT)	36273	1148.5021	1142.4370	1148.7710	6.3340	0.1303
$B^S{}_i - B^N{}_i$ (mT)	36272	0.0023	-0.1560	0.1340	0.2900	0.0655
$B^S{}_e - B^N{}_e$ (mT)	36273	-0.3622	-1.0810	0.2420	1.3230	0.5227
$B^N{}_i - B^L{}_i$ (mT)	68285	-0.0978	-0.2550	0.0260	0.2810	0.0430
$B^N{}_e - B^L{}_e$ (mT)	68285	-0.7057	-1.3700	-0.0850	1.2850	0.2355

15.6 μT (σ_B = 57 ppm), which can be considered as an upper bound for the reproducibility of the FMR marker, neglecting excitation current ripple, timing jitter, mechanical vibrations and other perturbations.

10.3.2 Stability at extraction

At extraction (B = 1.149 T at t = 1680 ms), the average difference between the new operational and the legacy B-Train is about 600 μT. Based on the measured correlation (Fig. 10.4d), this can be attributed to a combination of gain and offset error. In particular, the fixed offset of the legacy system may be a significant source of error, due to magnetic hysteresis effects being ignored. The stability of the two systems is 370 μT and 390 μT respectively, that is, one order of magnitude worse than at injection. The stability may be affected by the following error sources:

- **integrator drift**: this is normally the dominant error source in induction coil measurements [40]. After each periodic recalibration, the voltage offset is expected to have a zero average and vary randomly, independently for each acquisition channel. The similarity between the stability of the two systems suggests therefore the presence of a different, underlying systematic cause.
- **timing jitter**: this is typically well below one microsecond, and since the mean ramp rate is about 1 T/s this leads to negligible field errors < 1 μT.
- **current ripple**: a zoom-in of the excitation current on the injection plateau is plotted in Fig. 10.13. The measured standard deviation is 0.1 A which, taking into account the transfer function i.e. 354 μT/A, corresponds to an uncertainty equal to 35 μT. This value,

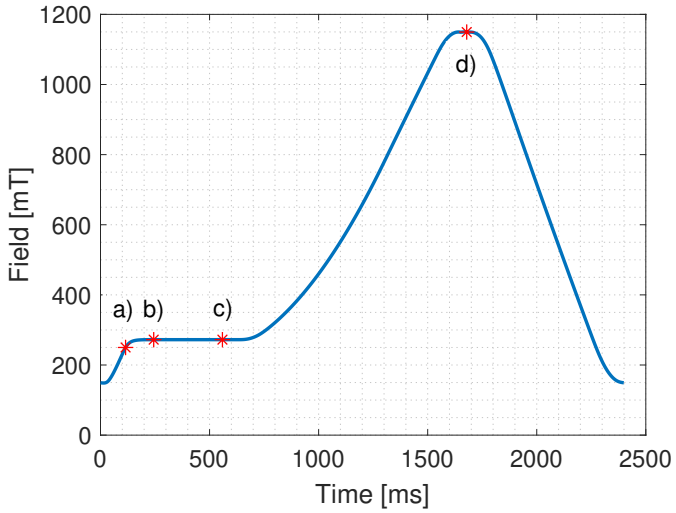

Figure 10.9 – LEIR *EARLY* cycle clone used for the reliability run, a) is the resonator sensor marker at t=116 ms. b) is the beam injection at t=245 ms, B=272.1 mT, c) is the LLRF feedback loops closure at t=560 ms and d) is the beam extraction at t=1680 ms, B=1.149 T.

which is already very low, is in all likelihood overestimated because of the low resolution of the current measurement.

- **magnet gap temperature**: this appears indeed to be the dominant factor, as can be derived from Fig. 10.14.

The measurements shown were taken by feeding alternately the new operational and the legacy B-Train to the RF on two different days, during which the thermal excursion was comparable, respectively about 6 °C and 4 °C. The new B-train shows a greater variability, due to its finer resolution. Some of the wider, abrupt variations (e.g. after 100 cycles and 1400 cycles) are an artifact due an integration re-calibration error that it in the process if being corrected.

Both B-trains exhibit a clear positive correlation with the temperature, respectively about 50 μT/°C and 25 μT/°C. The relative correlation coefficient for the new B-Train is 44 ppm/ °C, which is comparable to the coefficient at injection. This suggests that the same underlying mechanism (i.e. thermal deformation of the sensor support) may be responsible. The impact on the legacy B-Train is lower, but the cause is less clear: in fact, the measuring coil is supposed to be in thermal equilibrium with the iron yoke, rather than the surrounding air. Unlike the new B-Train, however, the legacy acquisition electronics is installed next to the LEIR control room in an open rack, hence is exposed to variable ambient conditions.

The RF radial loop correction is shown in Fig. 10.14e and 10.14f. The average value is about -1.5 kHz and -0.9 kHz for the new and legacy B-Trains respectively. Since the radial loop correction depends upon many beam parameters beside the magnetic field, the equivalent field differences i.e. -1.5 mT and -0.9 mT, can be considered in absolute value as an upper bound for the field measurement error.

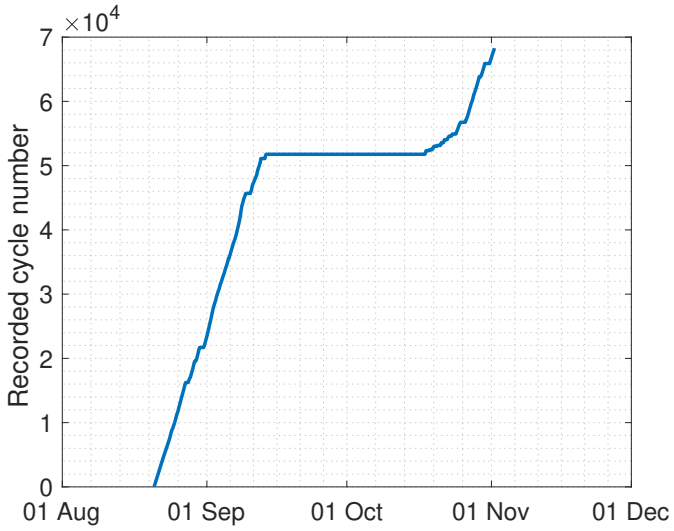

Figure 10.10 – LEIR Cumulated reliability run cycle count.

The frequency correction is also positively correlated with the gap temperature, and the correlation coefficients for the new and legacy B-train are respectively 50 Hz/°C and 75 Hz/°C. The equivalent coefficient in terms of field error for the new B-train is 50 μT/°C, which coincides precisely with the observed correlation. Such correspondence supports the hypothesis that the temperature does not affect at all the magnetic field, but only the measurement. The systematic component of this error could therefore be compensated by subtracting from the measurements the linear temperature contribution. The equivalent coefficient for the legacy B-train is 75 μT/°C, which is instead three times as high as the coefficient of the measured field. This may be linked to the initial offset of the legacy measurement, which may contain some temperature dependency which is not included in the measurements because of the fixed offset applied.

Table 10.2 – LEIR difference between B-Train sources during one day.

	B-Train source to the LLRF	
	Legacy	New
Temperature variation BHN30 (°C)	4.77±0.18	5.15±0.11
Field variation (mT)	0.1±0.01	0.192±0.015
Radial loop contribution average (Hz)	-900±20	-1550±50

10.3.3 LEIR reliability run conclusion

The results of the reliability run show that the new LEIR B-Train system is an effective replacement of the legacy system, which will be decommissioned before the 2021 run. Among many others, the new system offers three key improvements:

- two new, easily accessible measurement coils, preventing the risk associated with the

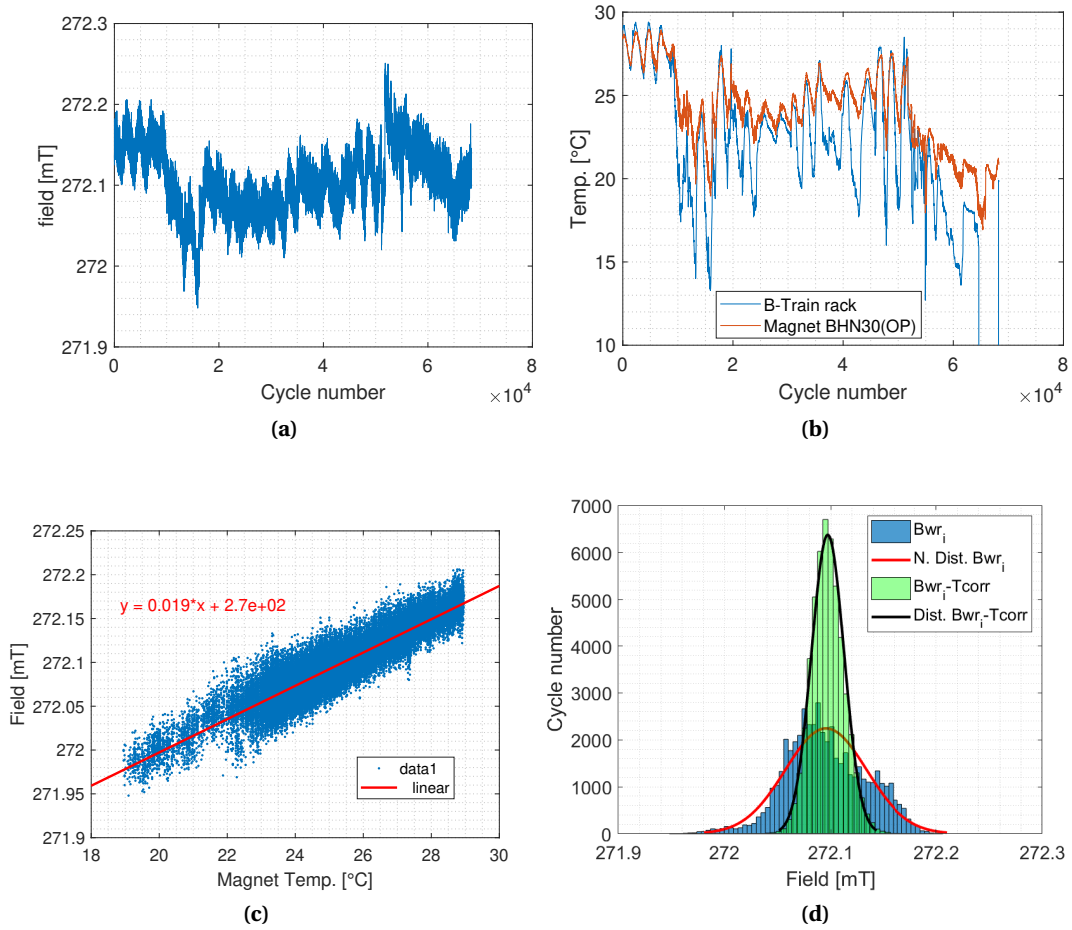

Figure 10.11 – LEIR field stability at injection. (a) Field value at injection for all cycles. (b) temperature in the B-Train rack (blue) and the magnet close to the B-Train sensors (red). (c) Correlation between the temperature and the injection field. (d) Distribution of the field at injection: raw data (blue), residual of the linear correlation (green). The bin size is about 10 μT. The continuous curves represent the best-fitting Gaussian.

only surviving legacy coil

- introduction of field markers to track magnetic hysteresis effects
- improved the integrated resolution from 10 μT to 0.2 μT

On the down-side, the location of the sensors in the fringe field region exposes them to effects linked to eddy currents, saturation and temperature. A peak error of 1.7 mT, as derived by the amplitude of the radial loop correction neglecting any other possible contribution, is observed in the middle of the up-ramp. This error is within the correction capabilities of the radial loop (with a margin higher than a factor two), and does not degrade appreciably the quality of the beam. If necessary it could be substantially reduced by adjusting the calibration of the new system so as to minimize the peak difference with respect to the legacy B-train, rather than the RMS average. Additional mitigation strategies, such as the subtraction in real-time of a correction proportional to $\dot{B}$, could be built in a future revision of the acquisition system.

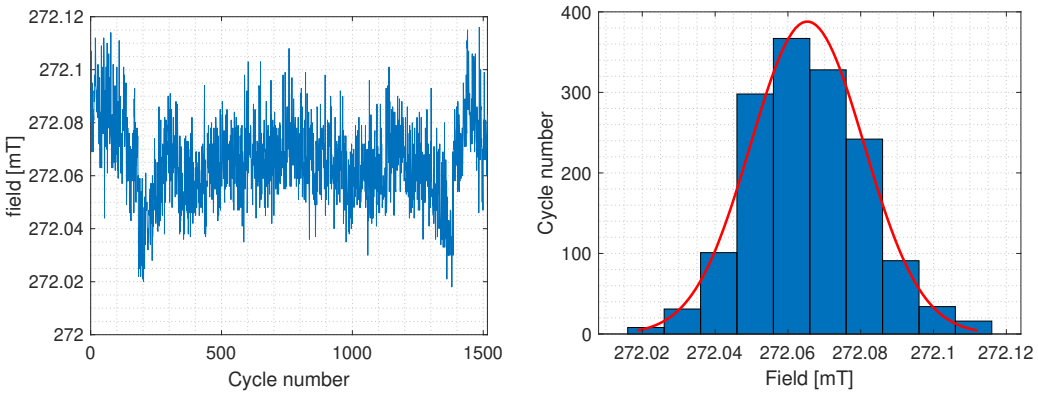

Figure 10.12 – LEIR field stability at injection and 24.3°C. (a) Field at injection with a temperature of 24.3 °C for 1515 cycles. (b) The corresponding distribution with a bin size by about 10 μT, the red curve is its Gaussian best-fit.

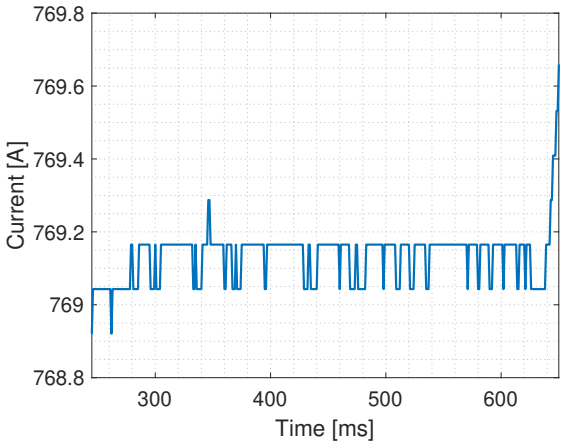

Figure 10.13 – LEIR current at injection *EARLY* cycle.

The stability of the new B-train at injection and extraction is 40 μT and 370 μT respectively, very closely comparable to that of the legacy system. Temperature has been established to play a major role, which is hardly surprising since the LEIR ring and the surrounding area are the most exposed to changing ambient conditions, among all five measured B-train systems. Even if the mechanism by which the temperature affects the measurement is not fully clarified, real-time numerical compensation may be investigated as a way to improve the stability, by more than a factor two in both cases.

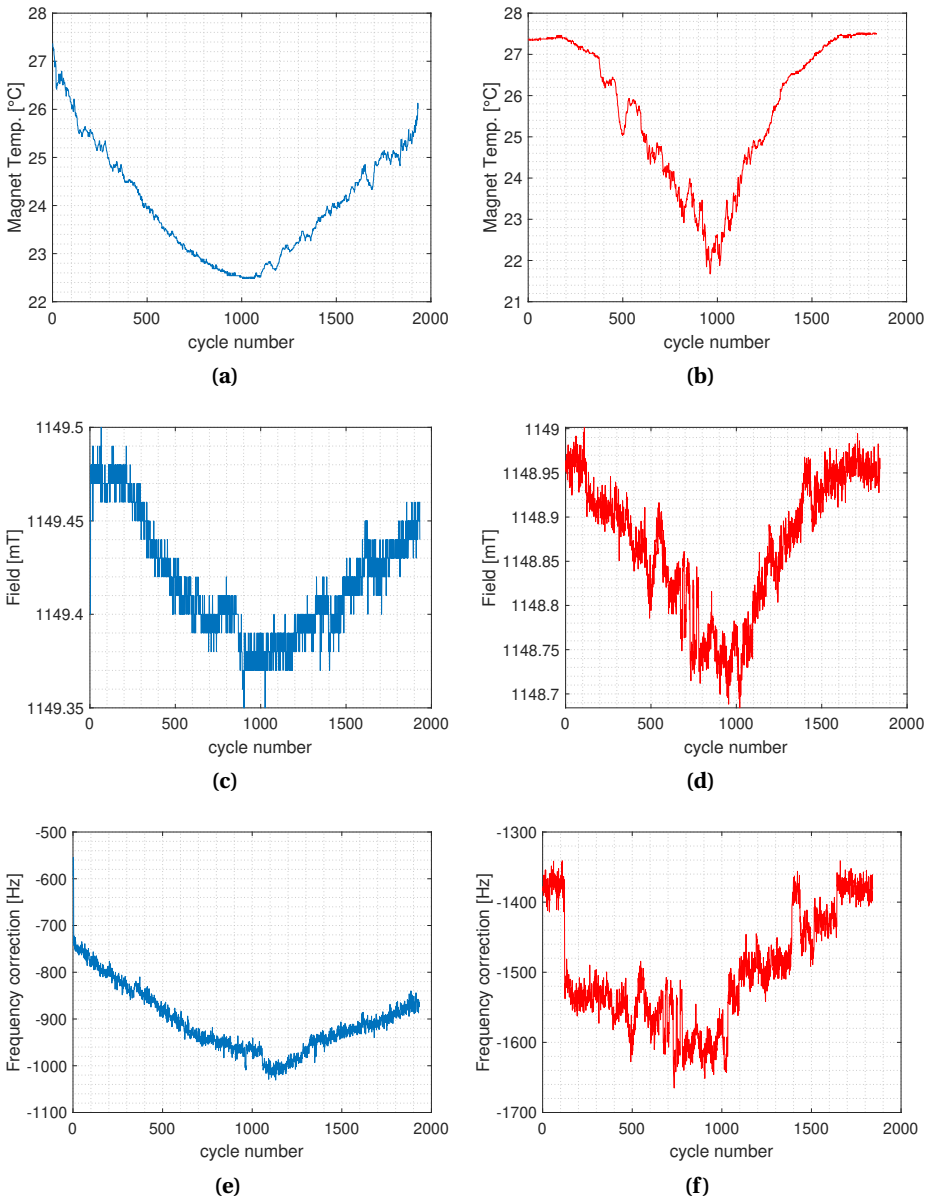

Figure 10.14 – LEIR reliability run radial loop legacy versus new B-train at extraction during one day(Ĩ930 cycles). The blue curves (left) are measurements taken the 28-29th August 2018 with the legacy B-Train system as source for the LLRF. The red curves (right) are measurements taken the 11-12th September 2018 with the new B-Train system as source for the LLRF. (a) and (b) are the temperatures of the BHN30 magnet. (c) and (d) are the B-fields. (e) and (f) are the LLRF radial loop contributions.

Conclusion and perspectives

In this thesis, we have presented the design, development, operation and performance of four time-transient magnetic field sensors based on electron spin resonance. These sensors operate over a wide range of field marker values, from 36 mT to 710 mT.

In particular, resonator topologies for operating frequencies below 10 GHz have been developed. Their performance has been shown to reach a resolution of about 0.5 nT/Hz$^{1/2}$ corresponding to a field marker reproducibility better than 5.2 μT with ferrimagnetic samples (GaYIG). The same structures have been characterized with paramagnetic samples (BDPA), as well. A parametric model of the co-planar waveguide structure has been implemented in view of future applications at different field marker levels. This approach, based on standard RF PCB technology, allows the end user to master all steps of the manufacturing process and leads to much higher performance and flexibility, in comparison with earlier attempts based on commercially available solutions (i.e., YIG filters).

Moreover, a topology based on CMOS integrated oscillators has been employed for operating frequencies above 10 GHz. A resolution of 0.1 nT/Hz$^{1/2}$, which is the best among all proposed sensors, has been reached for a marker field level of 360 mT. The down-scaling effect of the integrated LC oscillator has enabled field measurements at (i) higher levels up to 720 mT with the variable 20 GHz integrated LC oscillator, (ii) ramp rates up to 5 T/s and (iii) spatial gradients up 12 T/m, corresponding to an non-uniformity up to 25 m^{-1}. The lowest field gradient sensitivity has been obtained by reducing the sample size by an order of magnitude with respect to the resonator structures. The performance and the architecture of the 20 GHz oscillator highlight the possibility of measurements at even higher fields by a using similar design at 28 GHz (about 1 T) and 50 GHz (about 1.8 T) [117].

The research presented in this work has shown that the use of paramagnetic samples reduce the temperature sensitivity by a significant factor, up to five, and makes the sensor insensitive to misalignment with respect to the field direction. Moreover, the analytical signal and noise prediction for the co-planar waveguide resonator with BDPA has been validated by experimental measurements. The computed signal amplitude matches within 10%, while the noise is comparable within a factor two. Therefore, the analytical approach can be confidently applied to the design of future field marker sensors and their detection electronics.

In the framework of the LHC injector upgrade at CERN, it has been validated experimentally that the FMR resonator sensors fulfil the tight performance requirements in the PS and LEIR accelerators. From 2021, the two solutions proposed in this thesis will be used as operational markers for the PS, LEIR and PSB. From 2022, after reliability run phases, the EPR sensors could be used as operational devices.

On the basis of these encouraging results, further developments could be envisaged to meet upcoming accelerator operation requirements. First of all, the long-term maintainability of the EPR sensors could be easily improved by means of fully embedded and remote-controlled detection electronics. Furthermore, there is still considerable scope for optimising the bandwidth of the EPR sensors, to improve the SNR in strong field gradients such as those found in the fringe field of otherwise inaccessible reference magnets. Operational flexibility could be improved by means of tuneable resonator structures for field marker adjustment by about ± 5 mT around the nominal working point.

Finally, the EPR sensors developed as field markers could be applied in the more general context of static field magnetometry, by equipping them with modulation coils and appropriate detection electronics.

A Sensors summary table

The design and performance of the six markers are summarized in Tab. A.1.

Table A.1 – Field markers summary table.

Parameters	FMR 1 GHz Resonator	FMR 3 GHz Resonator	EPR 1 GHz Resonator	EPR 3 GHz Resonator	EPR 10 GHz Oscillator	EPR 20 GHz Oscillator
Architecture	discrete LC circuit	PCB waveguide	discrete LC circuit	PCB waveguide	OSCAM2 CMOS chip	OSCAM2 CMOS chip
PCB CERN ref.	EDA-03586-V1-0	EDA-03589-V1-0	EDA-03586-V2-0	EDA-03589-V2-0	EDA-04058-V1-0	EDA-04058-V1-0
PCB size width × length (mm)	20 × 20	20 × 25	20 × 20	20 × 25	25 × 25	25 × 25
Sample material	GaYIG	GaYIG	BDPA	BDPA	BDPA	BDPA
Sample fixation	screw+Araldite	screw+Araldite	shrink tube + Araldite	shrink tube + Araldite	Vacuum grease	Vacuum grease
Detection card	-	-	-	-	EDA-03692-V1-0	EDA-03692-V1-0
Operating frequency (MHz)	1109	3050	1078.9	3123	10111.37	20000 [1]
B_m (mT)	35.9	106.3	38.52	111.41	361.01	713.65
B_m tuning range (mT)	-	-	-	-	-	660-720
Linewidth (μT)	320	370	94	85	97	121
Effective γ (GHz/T)	28.29	28.69	28.01±0.01	28.03±0.01	28.01±0.01	28.02 [1]
Sample volume (μm^3)	14.1×10^3	14.3×10^3	63×10^6	160×10^6	1.2×10^6	0.07×10^6
$\dot{B}$ sensitivity (μT/(T/s))	<3	<3	4	4	<3	90
Gradient sensitivity (μT/(T/m))	-56	-	160	480	39	<10
Maximum gradient (T/m)	1.2	1.5	1.2	1.5	12	12
Maximum field inhomogeneity (m^{-1})	31	13	31	13	25	17
Temperature sensitivity (μT/°C)	3.6	2.2	4.8	7	-	-
Field direction sensitivity ψ (μT/°)	433	368	<1	<1	<1	<1
Resonator sensor sensitivity (V/T)	4256	2286	47450	90800	-	-
Resonator noise floor (V/Hz$^{1/2}$)	3.2×10^{-6}	3×10^{-6}	0.26×10^{-3}	0.2×10^{-3}	-	-
Oscillator sensor sensitivity (Hz/T)	-	-	-	-	31.7×10^9	17.2×10^9
Oscillator noise floor (Hz/Hz$^{1/2}$)	-	-	-	-	3	35
Resolution (nT/Hz$^{1/2}$)	0.7	1.3	5.5	2.2	0.095	2
Bandwidth (kHz)	150	150	100	100	160	160
Integrated resolution (μT_{RMS})	0.3	0.5	1.7	0.70	0.04	0.8
SNR (-)	1620	750	40	100	270	30

[1] The 20 GHz oscillator has no direct frequency output. As a consequence, the oscillation frequency cannot be measured. The reported oscillation frequency is computed measuring the magnetic field assuming an effective $\gamma = \gamma_{BDPA} = 28.02$ GHz/T (as reported in Ref. [95]).

B Oscillator detection board

The detection board used for the oscillators in Sec. 8.4 is the conditioning element of the EPR oscillator sensor. We designed the board with Altium™. This board is a 3U Eurocard format with a 8TE front panel fully compatible with the B-Train electronic crate. The board is composed of a carrier card (ref. EDA-03692) detailed in App. B.1, which allows mounting three types of mezzanine card for the YIG filter sensors (ref. EDA-03595), resonator sensors (ref. EDA-03596) and oscillator sensors (ref. EDA-03593).

B.1 Carrier card

The PCB for the carrier is a four layer laminates of Roger 4350B (0.25 mm)/FR4(0.92 mm)/Roger 4350B (0.25 mm) substrates thickness, with 35 μm copper thickness and nickel-gold plating with thickness of 3 μm and 0.1 μm, respectively. The top and bottom layers are dedicated to the signals, while the inner layers are used for the power and ground planes.

The implemented functions inside the carrier board are shown in Fig. B.1 and listed below:

- **The power supplies (Fig. B.2)** provide the required voltage source levels and power to all the circuits. This module is composed of four TPS7A4700RGWT to deliver 3 V, 2 × 5 V and 5.5 V. One HMC1060LP3E is installed to supply the RF generator with high stable voltage source. A step-up regulator (LT1930ES5#PBF) combined with a 10 V reference source (REF102AU), a potentiometer and two operational amplifiers (AD8676BRMZ) are used to provide a controlled reference voltage from 3 to 24 V for oscillator variable capacitor. Nevertheless, this voltage source was not used in case of the discussed 20 GHz oscillators[1].
- **The RF generator (Fig. B.3)** generates frequency from 25 to 6000 MHz with power between 0 to 9 dBm by a Analog Device HMC833LP6GE fractional-N PLL with integrated VCO, controlled via SPI by the B-Train SPEC card. The RF generator is clocked by a VCXO (Crystek CVHD-950) with a low phase noise of -155 dBc/Hz at 10 kHz itself driven by a

[1] It required bipolar lower voltage control (±1.8 V) and four controlled sources. Therefore, standalone reference voltage sources were privileged as detailed in Table 8.2.

PLL (HMC1031MS8E) where the input frequency come from the CERN master timing system via the CTRI card at 10 MHz.

- **The control interface (Fig. B.4)** is composed of several modules for the frequency measurement (Fig.B.4a) where the configuration for the frequency divider and LVDS transmission (by a SN65LVDS100DGK) through a HDMI connector are implemented. The RF generator is controlled via a SPI either by a local interface (via the demonstration board connected to a computer) or by remote control to the B-Train SPEC board through the HDMI connector as shown in Fig.B.4b. Finally, a mechanical switch is used to select the internal RF generator or an external generator.
- **The locking detection (Fig. B.3)** uses the DC output of the oscillator detection's PLL (on the mezzanine board) to generate a TTL signal when the PLL is locked (i.e., between 0.5 to 2.5 V) corresponding to the optimal locking range. This ensures a correct detection of the EPR signal. The TTL signal is delivered to the front panel and to the B-Train SPEC card through the HDMI connector.
- **The front panel user interface (Fig. B.6)** is where most of the connectors, LED and information are available. Only the RF connectors are fixed on the mezzanine board.
- **The ESR signal conditioning front end (Fig. B.7)** provides the signal in differential mode (via two AD8676BRMZ), with amplification and filtering capability for the B-Train crate. A buffer stage with a the single ended output is used for diagnostic purpose on the front panel.

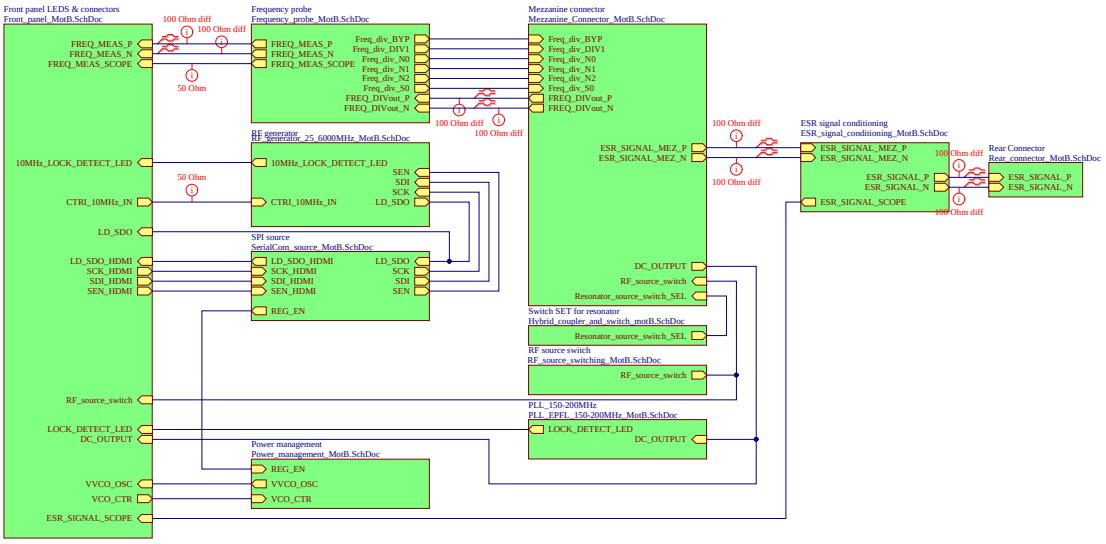

Figure B.1 – Carrier card functions layout.

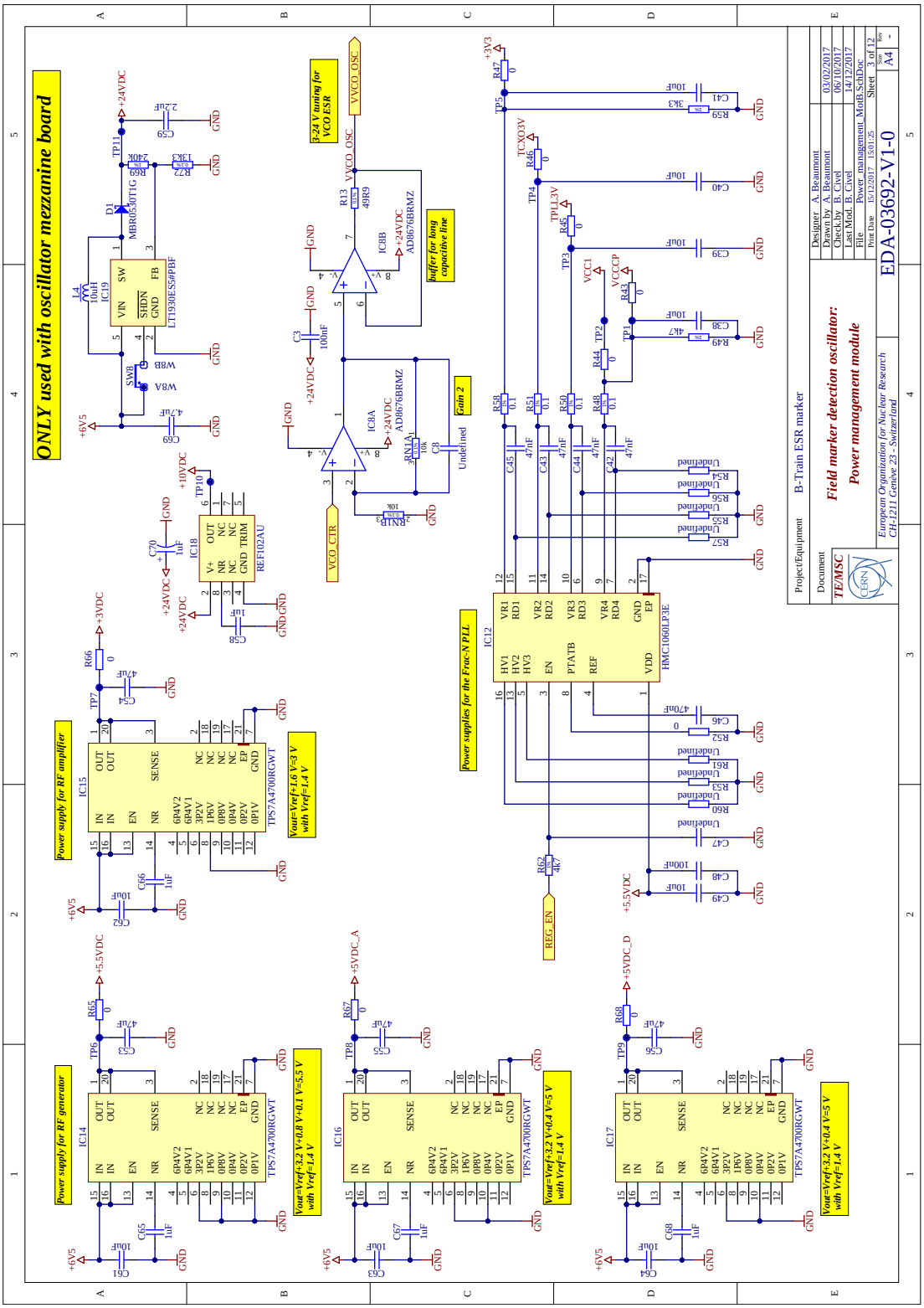

Figure B.2 – Carrier card power supply module.

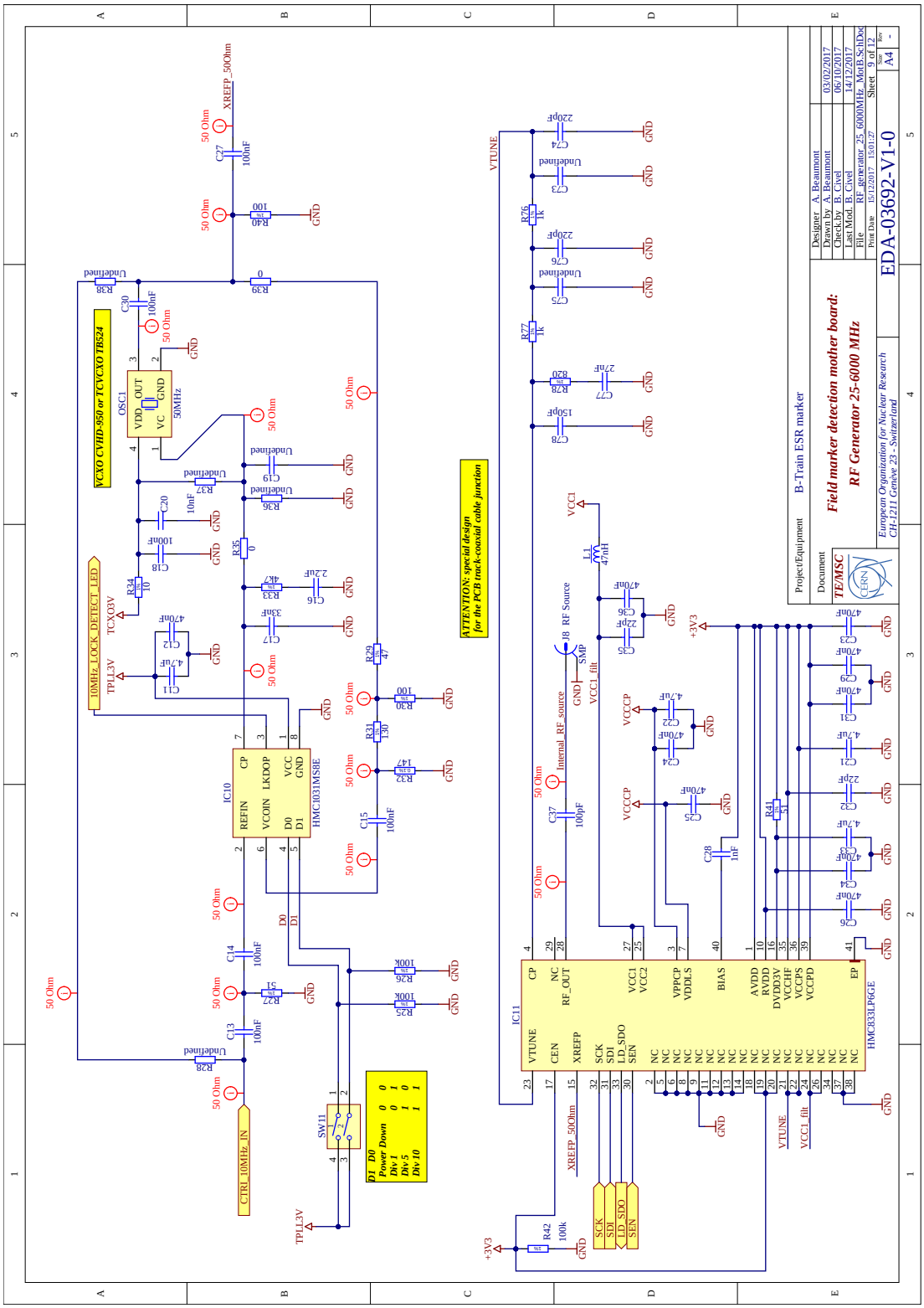

Figure B.3 – Carrier card RF generator module.

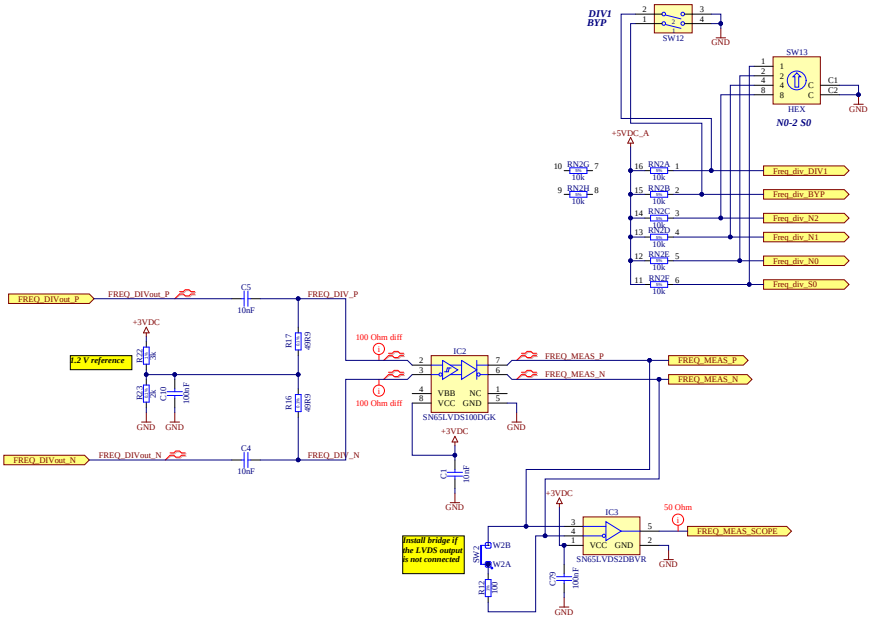

(a)

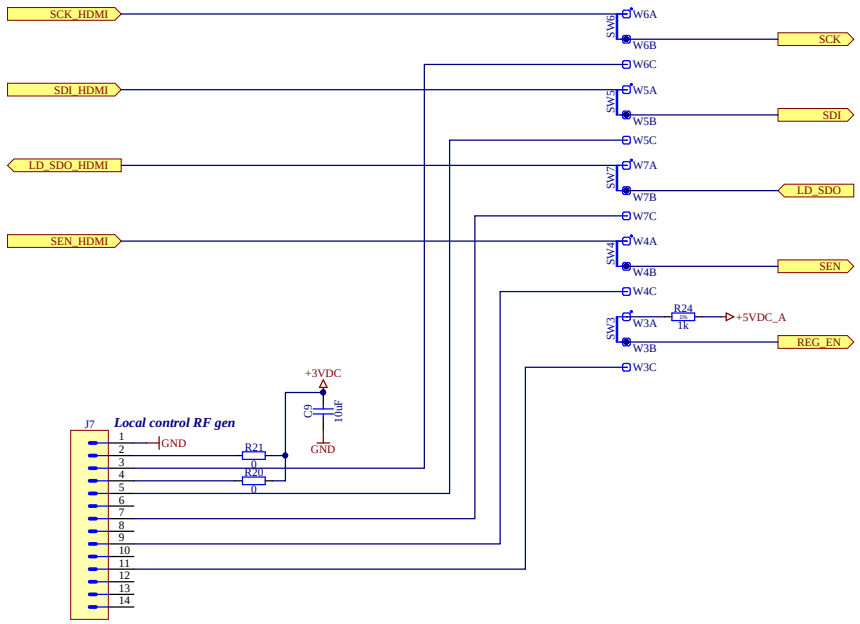

(b)

Figure B.4 – Carrier card controls. (a) Frequency measurements control. (b) RF generator control interface.

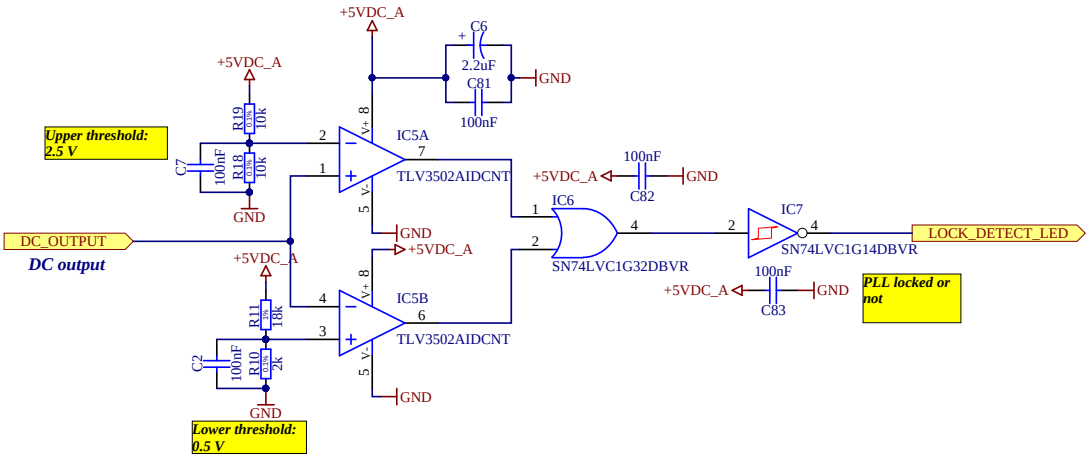

Figure B.5 – Carrier card PLL locking detection.

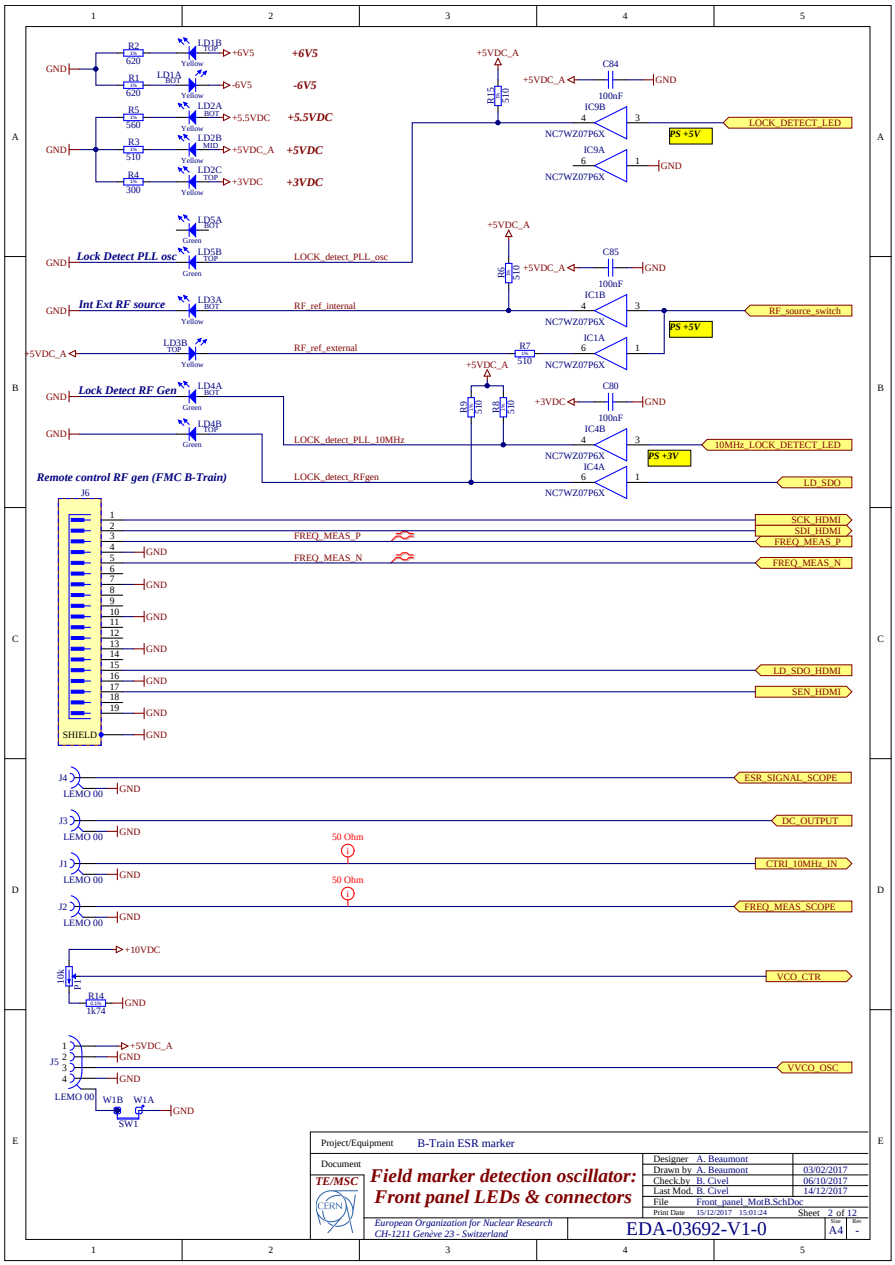

(a)

(b)

Figure B.6 – Carrier card front panel. (a) Front panel layout. (b) Front panel picture.

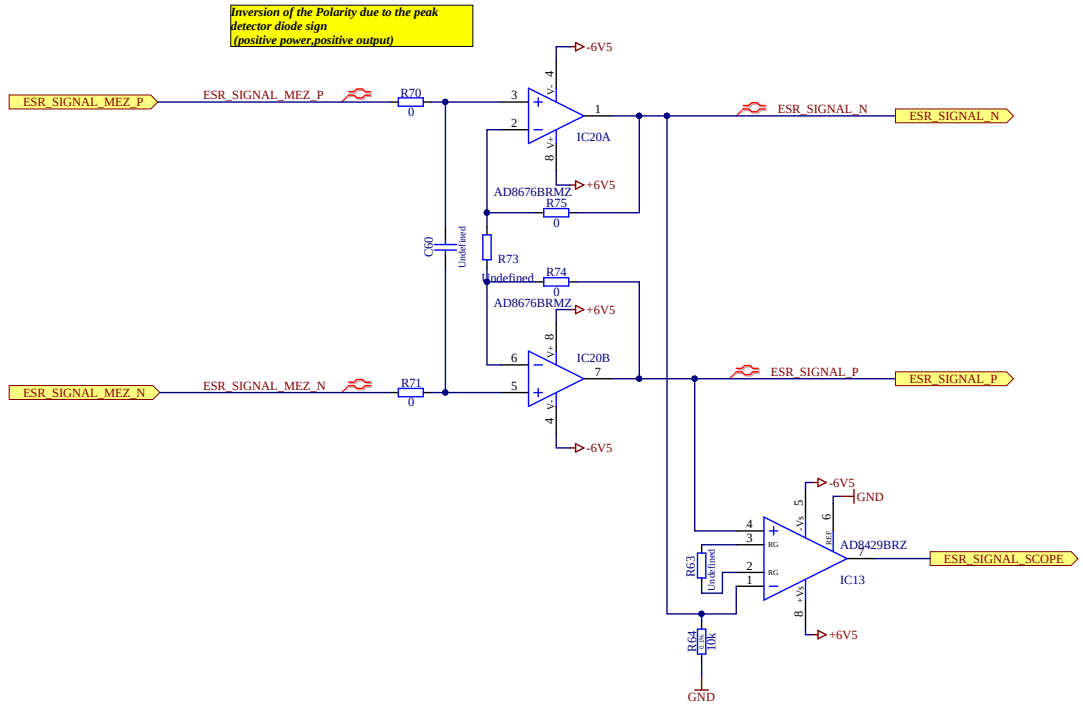

Figure B.7 – Carrier card EPR signal conditioning.

B.2 Mezzanine card for oscillator sensors

The PCB of the oscillator mezzanine card is a double layer laminate of Roger 4350B (1.524 mm thickness) with 35 μm copper thickness and a copper passived plating. The top layer of the PCB is protected with an EMI cover (Holland Shielding, 1500-100-55-15).The wall thickness of the cover is 0.18 mm. We installed this protection to limit electromagnetic interference from external sources and reduce the interference to the neighbourhood boards of the B-Train chassis. The internal wall of the screen is covered by a microwave absorber layer (Laird, 21109145) to avoid reflection inside the enclosure part. All the traces are impedance controlled with a characteristic impedance of 50 Ω. The components have different operating frequency range, but we selected them such that the sensor covering range is from 100 to 6000 MHz. The card has the following functions as presented in Fig. B.8 and described below:

- **The RF source switch (Fig. B.9)** selects the internal source (25- 6000 MHz generator) or an external RF generator by a SP2T RF switch (IDT, F2933NBGP). Attenuators of 5 dB and 10 dB combined with a RF amplifier of 12 dB (Guerrilla RF, GRF2003) are used to adjust the power from the different sources to the input stage.
- **The frequency probe (Fig. B.10)** is used to measure the frequency either of the source or of the oscillator. This verification is required for a long term operation to ensure the correct measured value of the marker (i.e, the $\gamma/2\pi$ determined by calibration). The measurement is performed by a directional coupler (Mini-Circuits®,SEDC-10-63+) combined with a divider by eight (AD, HMC363S8GE) stage. The fixed divider is followed by a programmable divider from 1 to 17 (AD, HMC705LP4E). At maximum RF input frequency (i.e., 6000 MHz) the output divided frequency is 50 MHz. This signal is then delived via LVDS to a frequency counter implemented in the FPGA of the B-Train SPEC card. The RF amplifiers of 12 dB (Guerrilla RF, GRF2003) and the attenuators are used to adapted the power level for the divider inputs.
- **The amplifier and mixer stages (Fig. B.11)** amplify (Guerrilla RF, GRF2003) and down-convert via a mixer (MACOM, MAMX-007238-CM25MH) the oscillator sensor frequency to the operating range of the PLL.
- **The 5th order band pass filter from 150 to 200 MHz (Fig. B.12)** was designed with the Circuit Design module of Ansys Electronics Desktop™. In addition to the filtering parameters, we design the filter in order to have a characteristic impedance of 50 Ω on its input and ouput. The filter has a flat insertion loss of -1.1 dB and a return loss of -30 dB from 150 to 200 MHz. The layout and components are shown in Fig. B.12a and the simulation results are presented in a Fig. B.12b.
- **The phase looked loop (PLL) (Fig. B.13)** was originally designed by Dr. A. V. Matheoud and detailed in Ref. [117]. We adapted the locking range to the operating frequency from 150 to 200 MHz, in particular, to the mezzanine card constraints. The PLL is composed of a phase-frequency detector (Hittite microwave corp, HMC439QS16GE) which compares the oscillator sensor phase to a reference VCO phase (Crystek, CVC055CL-0150-0200). This low phase noise VCO is driven by the output of the phase-frequency detector through a second order active filter. At the filter output a buffer drives the VCO, the

AC and the DC outputs of the PLL. The DC output has a low pass filter of 8 Hz. The differential AC output is amplified by an adjusting gain of 2, 16 or 151. A low pass filter of 160 kHz and a high pass filter of 160 Hz reduce the bandwidth of the marker signal.

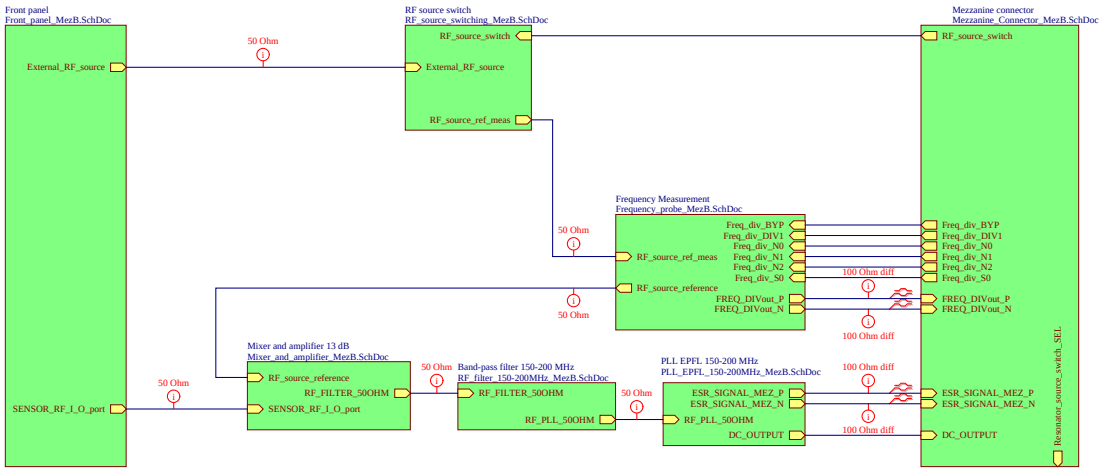

Figure B.8 – Mezzanine Detection functions layout.

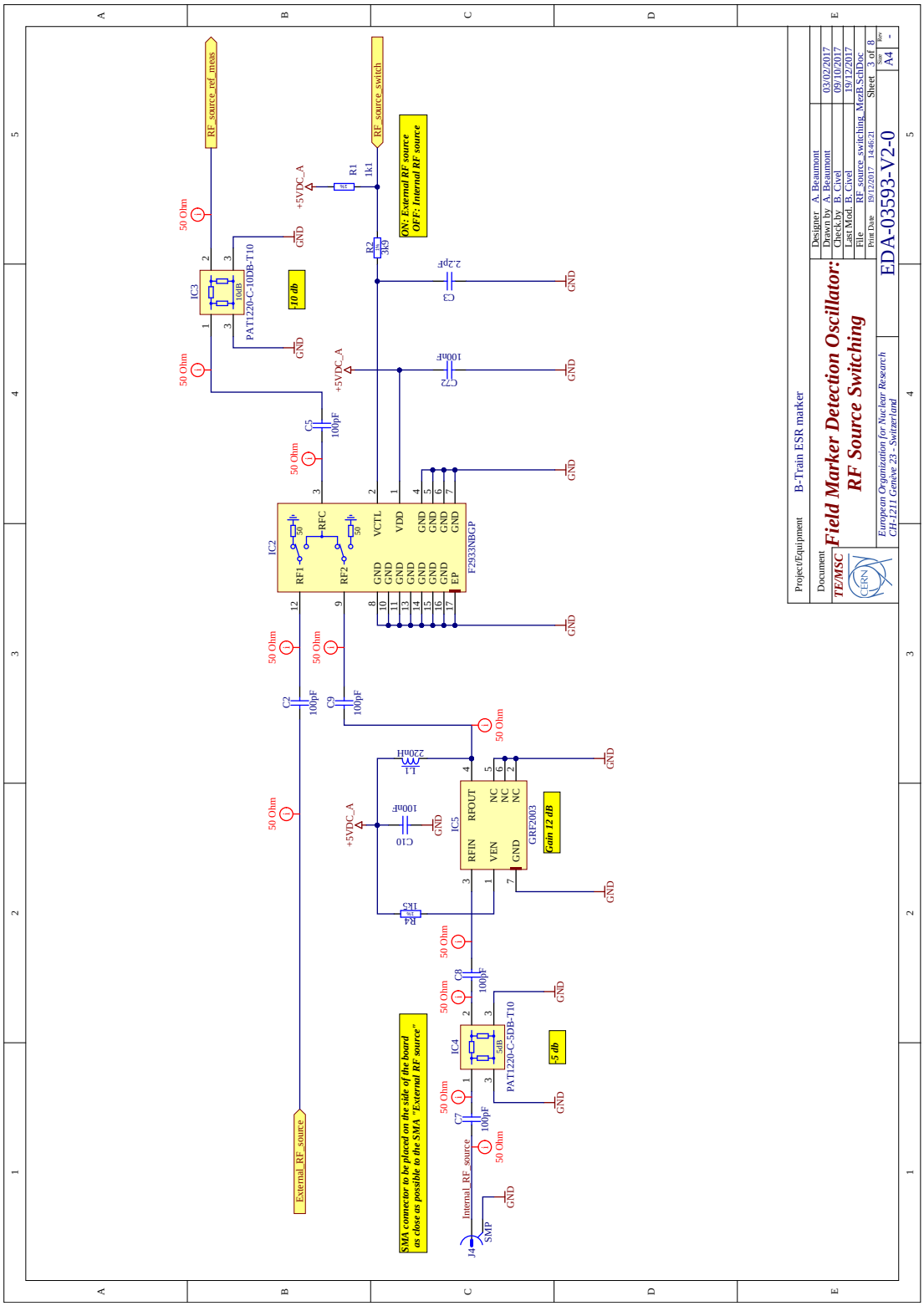

Figure B.9 – Mezzanine card RF source selection.

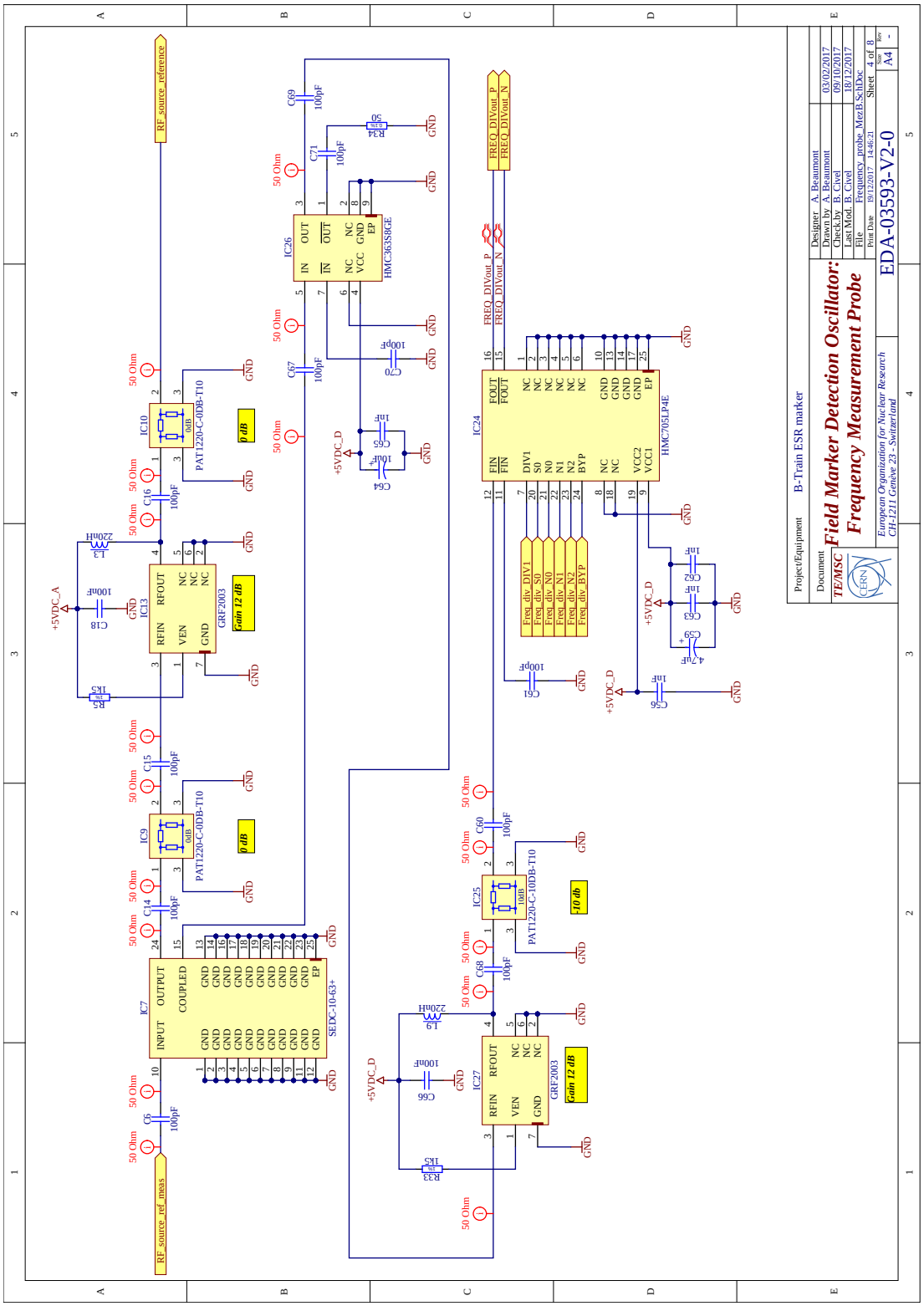

Figure B.10 – Mezzanine card frequency probe.

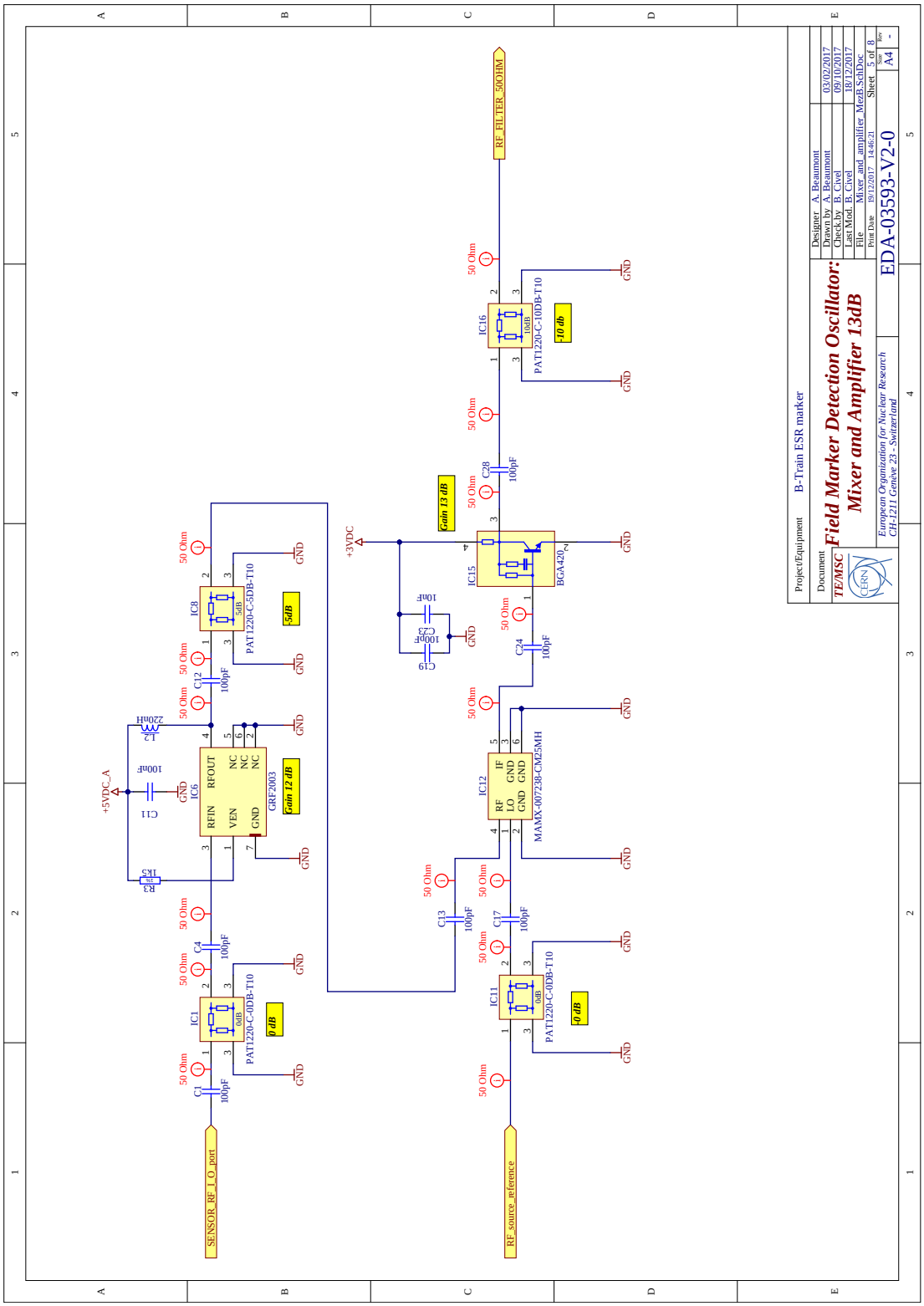

Figure B.11 – Mezzanine card amplifier and mixer stages.

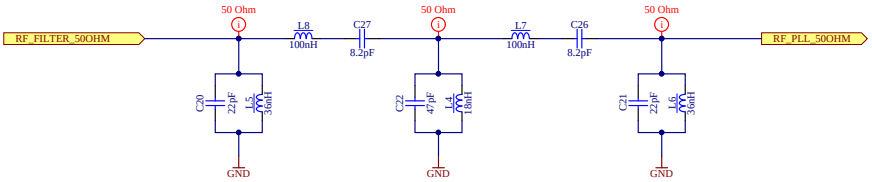

(a)

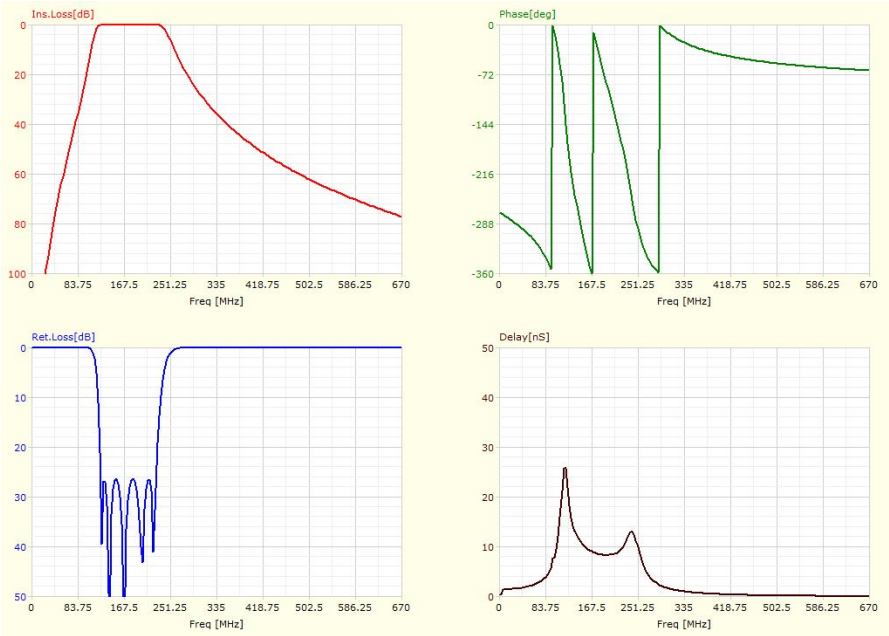

(b)

Figure B.12 – Mezzanine card 150 to 200 MHz filter. (a) The layout and components. (b) The simulation results including the insertion and return losses, the phase variation and the signal delay.

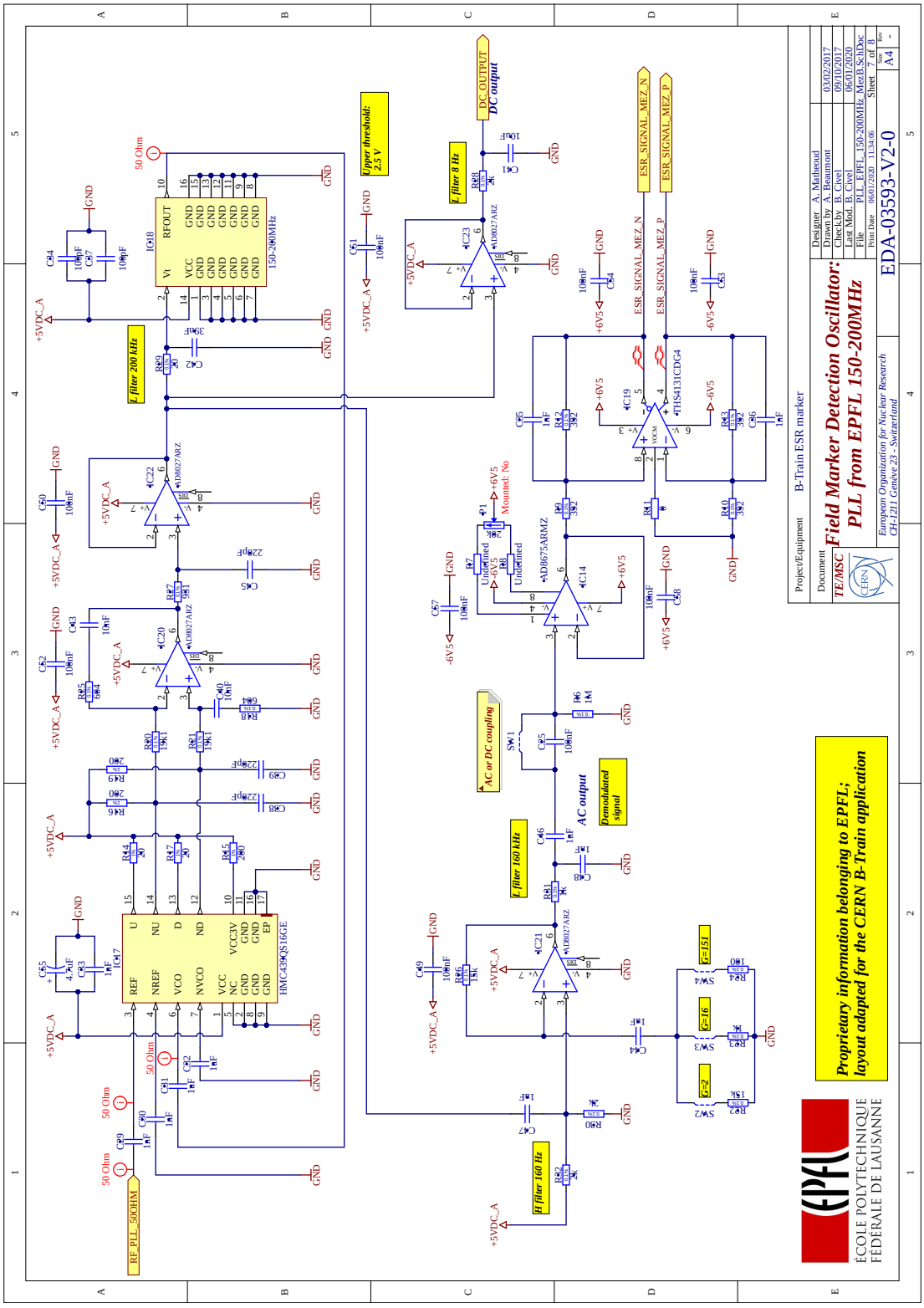

Figure B.13 – Mezzanine card PLL [117].

C Phase detection of the ESR signal

Dr. G. Boero proposed an alternative technique to the standard amplitude detection of the ESR sensors, by using the phase detection [132]. This method is well adapted to sensors using transmission line structures. In normal operation, almost all the RF power arrived to the receiver (excluding component and cables insertion losses), therefore the signal amplitude is too large for a Schottky diode input. At large amplitude, the diode works in non-linear and saturation regime. An attenuator can be used to reduce the amplitude to the linear regime of the diode, but it attenuates in the same proportion the magnetic resonance signal.
We tested this detection method on a GCPW transmission line with GaYIG ferrimagnetic sample as shown in Fig. C.1.

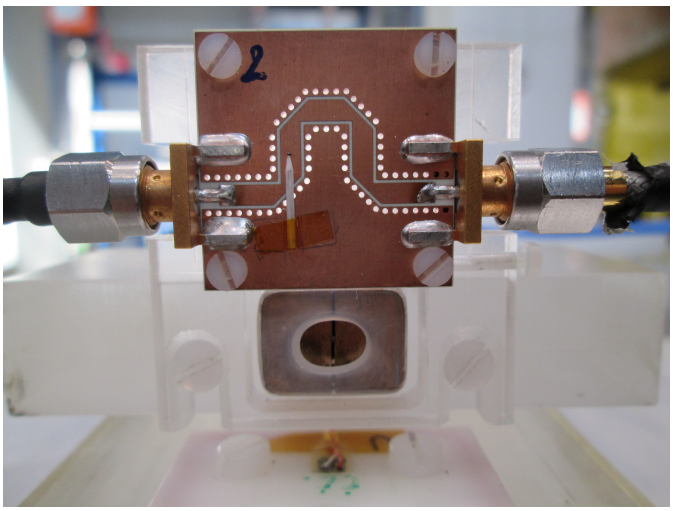

Figure C.1 – Transmission line sensor mounted with GaYIG (M_s = 36 mT that is 1 GHz).

C.1 Proposed layout

The detection principle is composed of a mixer that combines two RF signals out of phase (i.e., 90°). One signal directly arrives to the mixer, the other passes through the sensor. A low

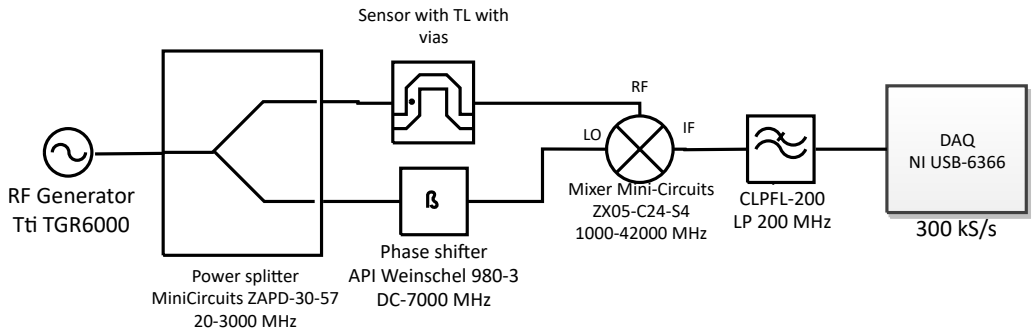

(a)

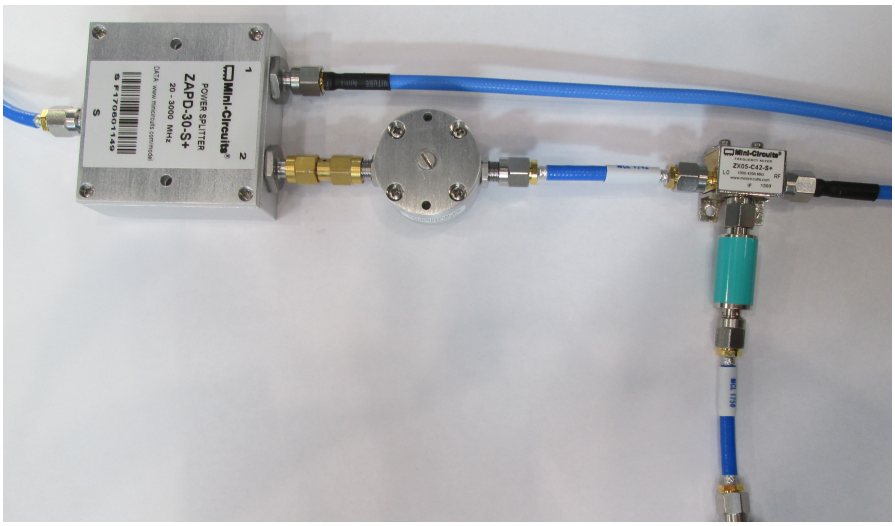

(b)

Figure C.2 – Phase Shift detection. (a) Phase detection layout. (b) RF components for the phase detection, from the left to the right: power splitter, phase shifter, mixer and low pass filter.

pass filter is used to extract only the DC component, which is then acquire by a DAQ. A power splitter is used to provide the same RF frequency at the mixer inputs (RF and LO). A tunable phase shifter is used to adjust the phase $\beta = \pi/2$ so that the DC component is almost zero outside the magnetic resonance. The phase shifter compensates the phase error due to the connectors, the different cable lengths and RF elements that can introduce phase shift. The implemented layout with the elements are in presented in Fig. C.2.

Figure C.3 shows a simulation of the output signal when the two input signals are in-or-out of phase and corresponds to:

- Outside magnetic resonance, the signals are adjusted to be 90° out of phase such that the mixer output DC component is zero as shown in Fig. C.3a.
- At the magnetic resonance, the phase mismatch created by the FMR sample produces a non-zero DC component (in Fig. C.3b).

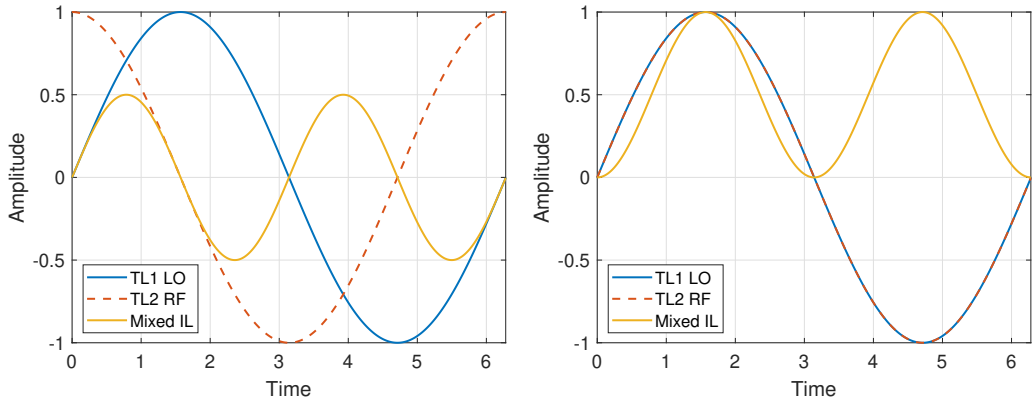

Figure C.3 – Simulation of phase shift with a mixer with two sinusoidal signals $\sin(\omega t + \beta)$,*TL1* is the reference transmission line connected to the local oscillator input (LO) of the mixer with $\beta = 0$. *TL2* is the transmission line sensor connected to the RF input of the mixer and *Mixed IL* is the intermediate frequency (IF) output of the mixer. (a) The two sinusoidal signal are 90° out of phase (*TL2* with $\beta = \pi/2$), no DC component is at the mixer IF output. (b) The two sinusoidal signal are in phase (*TL2* with $\beta = 0$), the DC component is maximum and equal to half of the amplitude of *TL2*.

The phase shifter is connected to the local oscillator (LO) input of the mixer. The transmission line sensor is connected to the RF input of the mixer. The low pass filter is connected at the Intermediate Frequency (IF) output of the mixer. We selected a low pass (LP) filter at 200 MHz with a characteristic impedance of 50 Ω.

We used the dipole calibration magnet (detailed in Sec.3.1), with a field ramp rate of 0.4 T/s (i.e., a current ramp rate of 460 A/s). The magnetic cycle was from -48 mT to 395 mT (i.e., a current from – 55 A to 450 A). We set the RF source power to +7 dBm, that is, the optimal working range of the mixer. The power at the sensor line was also set to +7 dBm. We tested different attenuators value at the sensor input (6 or 10 dB), but the SNR and shape of the output signal was not affected. Due to the limited operating range of phase shifter, the set frequency levels were chosen so that the DC signal at the mixer output was close to zero. Afterwards, a fine adjustment with the trim screw of the phase shifter was use to cancel the DC offset within ±500 μV. Nevertheless, we observed a drift of the DC component voltage by about 100 μV/min. The transmission line sensor is broadband from DC to 3 GHz (Return loss < −20 dB and insertion loss > −5 dB),therefore we measured the marker signal at several frequencies close to 1 GHz, 1.5 GHz, 2 GHz, 2.5 GHz and 3 GHz.

C.2 Measurement results

The FMR magnetic resonance is detected as shown in Fig. C.4d. However, we measured a crosstalk[1] between the magnetic resonance signal and the induction coil signal, as shown in Fig. C.4b and in Fig. C.4c. Both signals have an identical shape and ripple. We attribute this effect to the coaxial cables of the sensor. Those create a loop in the magnet aperture that induces electromotive forces at the mixer input during the field ramp, which propagates along with the signal through out the detection electronics. The magnetic resonance signal amplitude at 997 MHz is the smallest by 90.3 μV (in Fig. C.4d), since it reaches the low boundary of the GaYIG magnetization saturation.

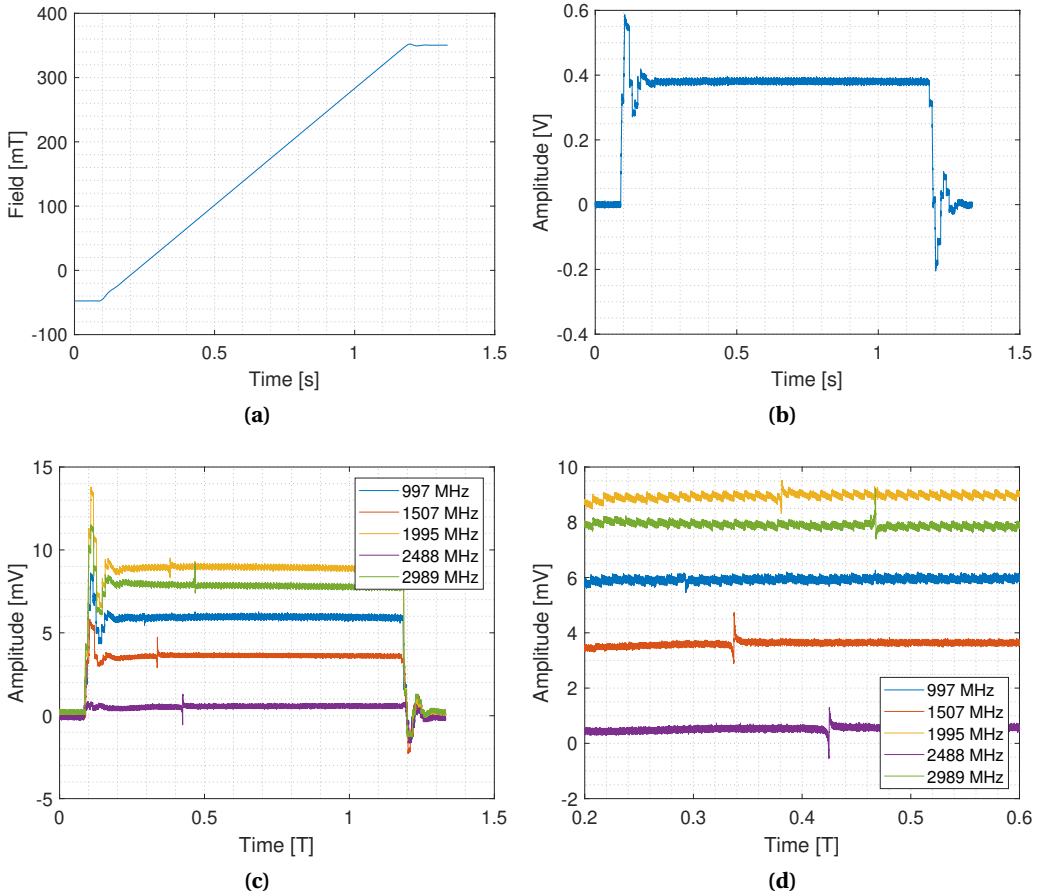

Figure C.4 – Phase detection results. (a) The field profile. (a) The search coil signal. (c) The marker signal at different frequencies. (d) Zoomed view at the marker signal.

By considering the highest signal amplitude with a frequency of 2488 MHz (in Fig.C.5, the peak-to-peak value is 1.85 mV for a noise of 0.19 mV (i.e., SNR=10).

Figure C.6 shows the measured field marker level and its corresponding gyromagnetic ratio.

[1]The DAQ channels crosstalk is not considered as it is non-multiplexed channels and many measurements performed in the past proved that there is no crosstalk between channels with the NI-6366 DAQ.

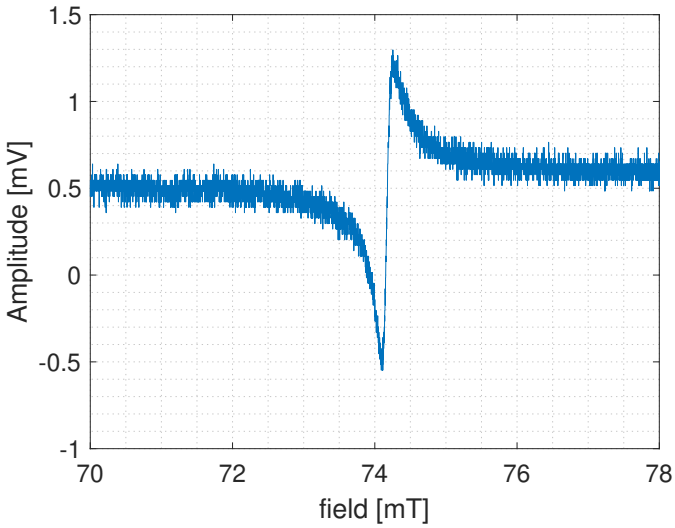

Figure C.5 – Marker signal with phase detection at 2488 MHz that is 87 mT.

The transmission line sensor is able to measure the field over a wide frequency range. The gyromagnetic ratio variation is about 1.5% and non-linear that is explained by the difficulty of measuring the exact resonance peak. Moreover, the GaYIG sphere was not aligned to the temperature stable axis that explain the high $\gamma/2\pi$ (i.e, by about 28.7 GHz/T) value.

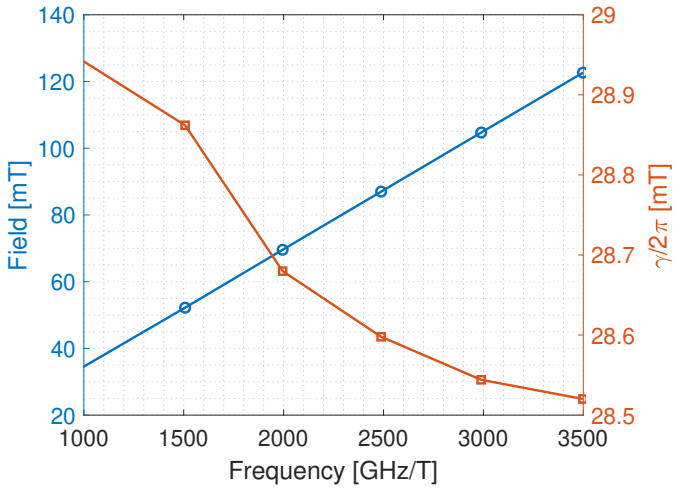

Figure C.6 – Marker value with phase detection at several frequencies. On the left axis the field marker value. On the right axis its corresponding gyromagnetic ratio.

C.3 Phase detection method conclusion

The proof of concept is demonstrated for the new phase-based detection circuit. With the tested transmission line sensor, the FMR signal can be measured over a wide field range from 36 to 120 mT, that is, from 1 to 3.5 GHz.

The main issue is the presence of a crosstalk between the field ramp rate and the FMR signal. The crosstalk creates a variable DC voltage component at the DAQ input that can be canceled by a a high pass filter of about 1 Hz. The noise can be significantly reduced by using a low pass filter of about 100 kHz as well as adding a low noise amplifier to operate far away from the noise floor of the DAQ. In addition, the performance can be increased by enlarging the tuning range, resolution and stability over time of the phase shifter. Moreover, the cables must be selected carefully to have a low phase variation with respect to the bending angle and temperature. Finally, for each set frequency the phase shifter must be adjust to have the output DC component close to zero. To simplify the operation, a digital controlled phase shifter can be used.

We did not test this detection method with the paramagnetic sample (BDPA) due to the already very low signal obtained with the YIG sample. A measurement can be performed, but all the aforementioned improvements must be implemented to have the possibility of detecting the EPR signal.

Bibliography

[1] P. Lebrun, "Particle accelerators, instruments of discovery in physics," in *CAS*, Vysoke , Slovakia, Sep. 2019.

[2] S. Sheehy, "Applications of Accelerators," in *CAS*, Vysoke , Slovakia, Sep. 2019.

[3] D. Perrelet, Y. Brischetto, H. Damerau, D. Oberson, M. Sundal, and A. Villanueva, "White-Rabbit Based Revolution Frequency Program for the Longitudinal Beam Control of the CERN PS," in *Proceedings, 15th International Conference on Accelerator and Large Experimental Physics Control Systems (ICALEPCS 2015): Melbourne, Australia, October 17-23, 2015*, 2015, p. MOPGF091. [Online]. Available: http://jacow.org/icalepcs2015/papers/mopgf091.pdf

[4] A. Peters, E. Feldmeier, C. Schömers, R. Steiner, H. Eickhoff, T. Knapp, and C. Welsch, "Magnetic Field Control in Synchrotrons," in *Joint Accelerator Conferences Website (JACoW)*, Vancouver, Canada, 01 2009, pp. 169–171. [Online]. Available: https://accelconf.web.cern.ch/accelconf/pac2009/papers/mo6pfp017.pdf

[5] C. Grech, M. Buzio, and N. Sammut, "A Magnetic Measurement Model for Real-Time Control of Synchrotrons," *IEEE Transactions on Instrumentation and Measurement*, Apr. 2019. [Online]. Available: https://ieeexplore.ieee.org/document/8680651

[6] M. Benedikt, F. Caspers, and M. Lindroos, "Application of magnetic markers for precise measurement of magnetic fields in ramped accelerators," *Part. Accel.*, vol. 63, pp. 57–73, 1999. [Online]. Available: http://cds.cern.ch/record/379810/files/p57.pdf

[7] A. Beaumont, M. Buzio, and G. Boero, "Ferrimagnetic Resonance Field Sensors for Particle Accelerators," *Review of Scientific Instruments*, vol. 90, no. 6, p. 065005, Jun. 2019. [Online]. Available: https://doi.org/10.1063/1.5097508

[8] E. Mobs, "The CERN accelerator complex - 2019. Complexe des accélérateurs du CERN - 2019," *CERN*, Jul 2019, general Photo. [Online]. Available: https://cds.cern.ch/record/2684277

[9] E. J. N. Wilson, "Fifty years of synchrotrons," *5th European Particle Accelerator Conference*, pp. 135–139, Jun. 1996. [Online]. Available: http://cds.cern.ch/record/339572

[10] L. Falbo, E. Bressi, S. Foglio, and C. Priano, "Betatron Core Slow Extraction at CNAO," in *Proc. 9th International Particle Accelerator Conference (IPAC'18), Vancouver, BC, Canada, April 29-May 4, 2018*, ser. International Particle Accelerator Conference, no. 9. Geneva, Switzerland: JACoW Publishing, June 2018, paper TUZGBF3, pp. 1237–1239, https://doi.org/10.18429/JACoW-IPAC2018-TUZGBF3. [Online]. Available: http://jacow.org/ipac2018/papers/tuzgbf3.pdf

[11] M. Modena, O. Dunkel, J. G. Perez, C. Petrone, E. Solodko, P. Thonet, D. Tommasini, and A. Vorozhtsov, "Design, Assembly and First Measurements of a Short Model for CLIC Final Focus Hybrid Quadrupole QD0," in *IPAC2012*, New Orleans, USA, 2012. [Online]. Available: http://accelconf.web.cern.ch/AccelConf/IPAC2012/papers/thppd010.pdf

[12] H. Leibrock, E. Floch, G. Moritz, L. Ma, W. Wu, P. Yuan, W. Weiyue, and Q. Wang, "Prototype of the Superferric Dipoles for the Super-FRS of the FAIR-Project," *IEEE Transactions on Applied Superconductivity*, vol. 20, no. 3, pp. 188–191, June 2010. [Online]. Available: https://ieeexplore.ieee.org/document/5433330?arnumber=5433330

[13] H. Wiedemann, *Periodic Focusing Systems*, 3rd ed. Springer, Mar. 2007, ch. 7, pp. 237–280.

[14] ——, *Perturbations in Beam Dynamics*, 3rd ed. Springer, Mar. 2007, ch. 12, pp. 411–469.

[15] J. Gareyte, J.-P. Koutchouk, and F. Ruggiero, "Landau damping dynamic aperture and octupole in LHC," CERN, Geneva, Tech. Rep. LHC-Project-Report-91. CERN-LHC-Project-Report-91, Feb 1997, revised version number 1 submitted on 2003-08-21 14:12:02. [Online]. Available: http://cds.cern.ch/record/321824

[16] A. Huschauer, H. Bartosik, S. C. Cave, M. Coly, D. Cotte, H. Damerau, G. P. Di Giovanni, S. Gilardoni, M. Giovannozzi, V. Kain, E. Koukovini-Platia, B. Mikulec, G. Sterbini, and F. Tecker, "Advancing the CERN proton synchrotron multiturn extraction towards the high-intensity proton beams frontier," *Phys. Rev. Accel. Beams*, vol. 22, p. 104002, Oct 2019. [Online]. Available: https://link.aps.org/doi/10.1103/PhysRevAccelBeams.22.104002

[17] L. Bottura, "Standard Analysis Procedures for Field Quality Measurement of the LHC Magnets Part I: Harmonics," CERN, Geneva, Tech. Rep. LHC-M-ES-0007, Nov. 2001, eDMS n. 313621. [Online]. Available: https://edms.cern.ch/document/313621/1.0

[18] S. Russenschuck, *Field computation for accelerator magnets: Analytical and numerical methods for electromagnetic design and optimization*. Weinheim: Wiley VCH Verlag GmbH, Mar. 2010. [Online]. Available: https://www.ebook.de/de/product/9218745/stephan_russenschuck_field_computation_for_accelerator_magnets.html

[19] J. Billan, L. Bottura, M. Buzio, G. D'Angelo, G. Deferne, O. Dunkel, P. Legrand, A. Rijllart, A. Siemko, P. Sievers, S. Schloss, and L. Walckiers, "Twin Rotating Coils for Cold Magnetic Measurements of 15 m Long LHC Dipoles," *IEEE Transactions on Appiled Superconductivity*, vol. 10, no. CERN-LHC-Project-Report-361, pp. 1422–1426, mar 2000.

[20] P. Arpaia, E. D. Matteis, and R. S. L. Moriello, "Unscented transform-based uncertainty analysis of rotating coil transducers for field mapping," *Review of Scientific Instruments*, vol. 87, no. 3, p. 035004, mar 2016.

[21] J. DiMarco, H. Glass, M. J. Lamm, P. Schlabach, C. Sylvester, J. C. Tompkins, and J. Krzywinski, "Field alignment of quadrupole magnets for the LHC interaction regions," *IEEE Transactions on Applied Superconductivity*, vol. 10, no. 1, pp. 127–130, Mar. 2000. [Online]. Available: https://ieeexplore.ieee.org/document/828192

[22] C. Petrone and S. Russenschuck, "Wire methods for measuring field harmonics, gradients and magnetic axes in accelerator magnets," phdthesis, University of Sannio, 2013, presented 2013. [Online]. Available: https://cds.cern.ch/record/1601973

[23] S. Russenschuck, "Rotating- and translating-coil magnetometers for extracting pseudo-multipoles in accelerator magnets," *COMPEL*, vol. 36, no. 5, pp. 1552–1567, 2017.

[24] G. Golluccio, A. Beaumont, M. Buzio, O. Dunkel, M. Stockner, and T. Zickler, "PCB coils array for measuring bent accelerator dipoles. Two case studies on the MedAustron accelerator," in *IMEKO*, Benevento, Italy, 2014, 20th IMECO.

[25] P. Arpaia, M. Buzio, J. G. Perez, C. Petrone, S. Russenschuck, and L. Walckiers, "Measuring field multipoles in accelerator magnets with small-apertures by an oscillating wire moved on a circular trajectory," *Journal of Instrumentation*, vol. 7, no. 05, pp. P05 003–P05 003, Apr. 2012. [Online]. Available: https://cds.cern.ch/record/1463586

[26] P. Arpaia, D. Caiazza, C. Petrone, and S. Russenschuck, "Uncertainty analysis of a vibrating-wire system for magnetic axes localization," in *2015 9th International Conference on Sensing Technology (ICST)*, Dec 2015, pp. 92–97.

[27] L. Bottura and K. N. Henrichsen, "Field Measurements," in *CAS - CERN Accelerator School on Superconductivity and Cryogenics for Accelerators and Detectors*. Geneva: CERN, May 2002, pp. 118–148, cERN-LHC-2002-020-MTA. [Online]. Available: https://cds.cern.ch/record/597621

[28] S. Hancock, "Energy Matching Between LEIR and PS," CERN, Geneva, techreport CERN-ACC-NOTE-2015-0019, Jul 2015. [Online]. Available: https://cds.cern.ch/record/2038693

[29] J. Belleman, V. Chohan, J. Gonzalez, S. Johnston, E. C. Schulte, and E. Thivent, "Measurement of the mean radial position of a lead ion beam in the CERN PS," in *5th European Particle Accelerator Conference*. Barcelona, Spain: JACoW, Jun. 1996, pp. 1603–1605, cERN-PS-96-023-BD. [Online]. Available: https://cds.cern.ch/record/308370

[30] P. Loschmidt, G. Gaderer, N. Simanic, A. Hussain, and P. Moreira, "White rabbit - sensor/actuator protocol for the CERN LHC particle accelerator," in *SENSORS, 2009 IEEE*, Oct 2009, pp. 781–786.

[31] V. Di Capua, P. Arpaia, M. Roda, and M. Buzio, "Real-Time Magnetic Measurement Monitoring under cRIO-LabVIEW Based Platform," 2019, not published.

[32] C. Bovet, R. Gouiran, I. Gumowski, and K. H. Reich, *A selection of formulae and data useful for the design of A.G. synchrotrons*. Geneva: CERN, 1970. [Online]. Available: https://cds.cern.ch/record/104153?ln=en

[33] P. Baudrenghien, "Low-level RF - Part I: Longitudinal dynamics and beam-based loops in synchrotrons," in *CERN Accelerator School: Specialised Course on RF for Accelerators*, no. arXiv:1201.2597, Ebeltoft, Denmark, Jun. 2010, p. 27, comments: 27 pages, contribution to the CAS - CERN Accelerator School: Specialised Course on RF for Accelerators; 8 - 17 Jun 2010, Ebeltoft, Denmark. [Online]. Available: https://cds.cern.ch/record/1415913

[34] M. E. Angoletta, S. Albright, S. Energico, S. Hancock, M. Jaussi, A. Jones, J. Molendijk, M. Paoluzzi, and J. Sanchez-Quesada, "Initial Beam Results of CERN ELENA's Digital Low-Level RF System," in *IPAC2017*, no. CERN-ACC-2017-264, Copenhagen, Denmark, May 2017, p. THPAB142. 4 p. [Online]. Available: https://cds.cern.ch/record/2289141

[35] J. C. Denard, "Beam current monitors," in *CAS - CERN Accelerator School: Course on Beam Diagnostics*, Dourdan, France, May 2009, p. 141, cERN-2009-005. [Online]. Available: http://cds.cern.ch/record/1213275

[36] R. C. Webber, "Charged particle beam current monitoring tutorial," *AIP Conference Proceedings*, vol. 333, no. 1, pp. 3–23, 1995. [Online]. Available: https://aip.scitation.org/doi/abs/10.1063/1.48014

[37] Q. King, S. Page, H. Thiesen, and M. Veenstra, "Function Generation and Regulation Libraries and their Application to the Control of the New Main Power Converter (POPS) at the CERN CPS," in *ICALEPCS*, JaCoW, Ed., Grenoble, France, Oct. 2011, pp. 886–889.

[38] F. Boattini, J. Burnet, and G. Skawinski, "POPS: The 60MW power converter for the PS accelerator: Control strategy and performances," in *2015 17th European Conference on Power Electronics and Applications (EPE'15 ECCE-Europe)*, Sep. 2015, pp. 1–10.

[39] J. Vella Wallbank, M. Buzio, D. Giloteaux, C. Grech, and N. Sammut, "Development of a Real-Time Magnetic Measurement System for Synchrotrons," 2020, unpublished, title and authors list might change.

[40] M. Buzio, "Fabrication and calibration of search coils," in *Proceedings, 2009 CAS-CERN Accelerator School: Specialised course on Magnets: Bruges, Belgium, June 16 - 25, 2009*, 2011. [Online]. Available: https://arxiv.org/ftp/arxiv/papers/1104/1104.0803.pdf

[41] E. Feldmeier, T. Haberer, A. Pters, C. Schoemers, and R. Steiner, "Magnetic field correction in normal conducting synchrotrons," in *IPAC*. Kyoto: IPAC, 2010, hIT. [Online]. Available: http://accelconf.web.cern.ch/AccelConf/IPAC10/papers/mopd004.pdf

[42] G. Franzini, O. Coiro, D. Pellegrini, M. Serio, A. Stella, M. Pezzetta, and M. Pullia, "Final design and features of the B-Train system of CNAO," in *IPAC*. Kyoto: IPAC, 2010. [Online]. Available: http://accelconf.web.cern.ch/AccelConf/IPAC10/papers/wepeb079.pdf

[43] P. Di Cesare, C. Reymond, H. Rottstock, and P. Sommer, "SPS magnetic field cycle measurement system: Investigation on Nuclear Magnetic Resonnance (NMR) system to get a faster reading of field values," CERN, Geneva, techreport CERN-SPS-PCO-Note 89-9, Apr 1989. [Online]. Available: https://cds.cern.ch/record/2158783

[44] M. Benedikt, F. Caspers, and T. Salvermoser, "Absolute Calibration of the CERN PS-Booster Bending Field with Beam and NMR," CERN, Geneva, techreport PS-OP-Note-98-23, 1998.

[45] C. Grech, A. Beaumont, M. Buzio, and N. Sammut, "Performance comparison of Nuclear Magnetic Resonance and FerriMagnetic Resonance field markers for the control of low-energy Synchrotrons," *Journal of Physics: Conference Series*, vol. 1065, no. 5, p. 052022, 2018. [Online]. Available: https://doi.org/10.1088/1742-6596/1065/5/052022

[46] C. Grech, R. Avramidou, A. Beaumont, M. Buzio, N. Sammut, and J. Tinembart, "Metrological Characterization of Nuclear Magnetic Resonance Markers for Real-time Field Control of the CERN ELENA Ring Dipoles," *IEEE Sensors Journal*, vol. 18, no. 14, pp. 5826–5833, Jul. 2018. [Online]. Available: https://ieeexplore.ieee.org/abstract/document/8370735

[47] A. Beaumont, "NMR magnetic field markers of the B-Train for the Proton Synchrotron accelerator," mathesis, UTBM, Belfort, France, Mar. 2009, eDMS:993482. [Online]. Available: https://edms.cern.ch/document/993482/1

[48] M. Buzio, A. Beaumont, P. Galbraith, S. Gilardoni, D. Giloteaux, G. Golluccio, C. Petrone, and L. Walckiers, "Development of upgraded magnetic instrumentation for CERN's real-time reference field measurement systems," in *IPAC*. Kyoto: IPAC, 2010. [Online]. Available: http://accelconf.web.cern.ch/AccelConf/IPAC10/papers/MOPEB016.pdf

[49] S. Gross, C. Barmet, B. E. Dietrich, D. O. Brunner, T. Schmid, and K. P. Pruessmann, "Dynamic nuclear magnetic resonance field sensing with part-per-trillion resolution," *Nature Communications*, vol. 7, p. 13702, Dec. 2016. [Online]. Available: https://doi.org/10.1038/ncomms13702

[50] M. Grisi, G. Marc Conley, P. Sommer, J. Tinembart, and G. Boero, "A single-chip integrated transceiver for high field NMR magnetometry," *Review of Scientific Instruments*, vol. 90, no. 1, p. 015001, Jan. 2019. [Online]. Available: https://doi.org/10.1063/1.5066436

[51] J. M. Kelly, "Magnetic Field Measurements with Peaking Strips," *Review of Scientific Instruments*, vol. 22, no. 4, pp. 256–258, apr 1951.

[52] S. Giordano, G. K. Green, and E. J. Rogers, "The Control System. Part III- Peaking Strips," *Review of Scientific Instruments*, vol. 24, no. 9, p. 848, Sep. 1953.

[53] F. Caspers, "Fonctionnement d une sonde FMR," CERN, Geneva, techreport SPS-AOP-Note 88-5 and SPS/PCO/Note 89-9, 1988.

[54] ——, "FerriMagnetic Resonance: A method to measure magnetic fields in accelerator environment," CERN, Geneva, techreport CERN-PS-AR-Note-94-21, Jul. 1994. [Online]. Available: http://cds.cern.ch/record/1706620/files/CERN-PS-AR-NOTE-94-21.pdf

[55] P. Arpaia, M. Buzio, F. Caspers, G. Golluccio, and C. Petrone, "Static Metrological Characterization of a Ferrimagnetic Resonance Transducer for Real-Time Magnetic Field Markers in Particle Accelerators," in *IEEE Internationnal Instrumentation and Measurement Technology Conference (I2MTC)*. Binjiang, China: IEEE, May 2011.

[56] P. Arpaia, M. Buzio, F. Caspers, G. Golluccio, and D. Oberson, "Metrological Performance of a Ferrimagnetic Resonance Marker for the Field Control of the CERN Proton Synchrotron," *IEEE Transactions on Applied Superconductivity*, vol. 22, no. 3, pp. 9 001 904–9 001 904, jun 2012. [Online]. Available: https://ieeexplore.ieee.org/document/6104109

[57] C. P. Poole, *Electron Spin Resonance: A Comprehensive Treatise on Experimental Techniques*, J. Wiley, Ed. Mineola, New York: DOVER PUBLICATIONS,INC, 1984.

[58] A. Schweiger and G. Jeschke, *Principles of pulse electron paramagnetic resonance*. Oxford University Press, 2001.

[59] H. Gebhardt and E. Dormann, "ESR gaussmeter for low-field applications," *Journal of Physics E: Scientific Instruments*, vol. 22, no. 5, pp. 321–324, may 1989. [Online]. Available: https://iopscience.iop.org/article/10.1088/0022-3735/22/5/011

[60] D. Duret, M. Beranger, M. Moussavi, P. Turek, and J. J. Andre, "A new ultra low-field ESR spectrometer," *Review of Scientific Instruments*, vol. 62, no. 3, pp. 685–694, 1991. [Online]. Available: https://doi.org/10.1063/1.1142068

[61] N. Kernevez, D. Duret, M. Moussavi, and J.-M. Leger, "Weak Field NMR and ESR Spectrometers and Magnetometers," *IEEE Transactions on Magnetics*, vol. 28, no. 5, Sep. 1992. [Online]. Available: https://doi.org/10.1109/20.179715

[62] D. Duret, M. Beranger, and M. Moussavi, "An absolute Earth field ESR vectorial magnetometer," *IEEE Transactions on Magnetics*, vol. 28, no. 5, pp. 2187–2189, Sep. 1992. [Online]. Available: https://doi.org/10.1109/20.179438

[63] D. Duret, J. Bonzom, M. Brochier, M. Frances, J. M. Leger, R. Odru, C. Salvi, T. Thomas, and A. Perret, "Overhauser magnetometer for the Danish Oersted satellite," *IEEE Transactions on Magnetics*, vol. 31, no. 6, pp. 3197–3199, Nov 1995. [Online]. Available: https://doi.org/10.1109/20.490326

[64] K. Lang, M. Moussavi, and E. Belorizky, "New, High-Performance, Hydrogenated Paramagnetic Solution for Use in Earth Field DNP-NMR Magnetometers," *The Journal of Physical Chemistry A*, vol. 101, no. 9, pp. 1662–1671, Feb 1997. [Online]. Available: https://doi.org/10.1021/jp962283g

[65] S. V. Sundramoorthy, B. Epel, and H. J. Halpern, "A Pulse EPR 25 mT Magnetometer with 10 ppm Resolution," *Applied Magnetic Resonance*, vol. 48, no. 8, pp. 805–811, Aug 2017. [Online]. Available: https://doi.org/10.1007/s00723-017-0902-0

[66] E. Tiesinga, P. J. Mohr, D. B. Newell, and B. N. Taylor, *The 2018 CODATA Recommended Values of the Fundamental Physical Constants (Web Version 8.0)*, National Institute of Standards and Technology, National Institute of Standards and Technology Std., May 2019. [Online]. Available: http://physics.nist.gov/constants

[67] A. J. Maubon, J.-M. Ferru, V. Berger, M. C. Soulage, M. DeGraef, P. Aubas, P. Coupeau, E. Dumont, and J.-P. Rouanet, "Effect of Field Strength on MR Images: Comparison of the Same Subject at 0.5, 1.0, and 1.5 T," *RadioGraphics*, vol. 19, no. 4, pp. 1057–1067, 1999, pMID: 10464808. [Online]. Available: https://doi.org/10.1148/radiographics.19.4.g99jl281057

[68] A. Savitsky and K. Möbius, "High-field EPR," *Photosynthesis Research*, vol. 102, no. 2, pp. 311–333, Dec 2009. [Online]. Available: https://doi.org/10.1007/s11120-009-9432-4

[69] M. E. Ladd, P. Bachert, M. Meyerspeer, E. Moser, A. M. Nagel, D. G. Norris, S. Schmitter, O. Speck, S. Straub, and M. Zaiss, "Pros and cons of ultra-high-field MRI/MRS for human application," *Progress in Nuclear Magnetic Resonance Spectroscopy*, vol. 109, pp. 1 – 50, 2018. [Online]. Available: http://www.sciencedirect.com/science/article/pii/S007965651830013X

[70] P. C. Fletcher and R. O. Bell, "Ferrimagnetic Resonance Modes in Spheres," *Journal of Applied Physics*, vol. 30, no. 5, p. 687, 1959. [Online]. Available: https://doi.org/10.1063/1.1735216

[71] J. H. Van Vleck, "Ferrimagnetic Resonance of Rare-Earth-Doped Iron Garnets," *Journal of Applied Physics*, vol. 35, no. 3, p. 882, 1964. [Online]. Available: https://doi.org/10.1063/1.1713520

[72] C. Kittel, "On the Theory of Ferromagnetic Resonance Absorption," *Phys. Rev.*, vol. 73, no. 2, pp. 155–161, Jan. 1948. [Online]. Available: https://link.aps.org/doi/10.1103/PhysRev.73.155

[73] T. Okamura, Y. Torizuka, and Y. Kojima, "The *g* Factor of Ferrites," *Phys. Rev.*, vol. 88, no. 6, pp. 1425–1426, Dec. 1952. [Online]. Available: https://link.aps.org/doi/10.1103/PhysRev.88.1425.2

[74] T. Tsutaoka, T. Kasagi, and K. Hatakeyama, "Permeability spectra of yttrium iron garnet and its granular composite materials under dc magnetic field,"

Journal of Applied Physics, vol. 110, no. 5, p. 053909, 2011. [Online]. Available: https://doi.org/10.1063/1.3626057

[75] J. Fuzerova, J. Fuzer, P. Kollar, L. Hegedus, R. Bures, and M. Faberova, "Analysis of the Complex Permeability Versus Frequency of Soft Magnetic Composites Consisting of Iron and $Fe_{73}Cu_1Nb_3Si_{16}B_7$," *IEEE Transactions on Magnetics*, vol. 48, no. 4, pp. 1545–1548, April 2012.

[76] J. Krupka, "Measurement of the complex permittivity, initial permeability, permeability tensor and ferromagnetic linewidth of gyromagnetic materials," *Measurement Science and Technology*, vol. 29, no. 9, p. 092001, jul 2018. [Online]. Available: https://doi.org/10.1088%2F1361-6501%2Faacf5d

[77] J. Nicolas, *Microwave Ferrites*. North-Holland Publishing Company, 1980, ch. 4, pp. 243–296.

[78] G. L. Matthaei, L. Young, and E. M. T. Jones, *Mechanically and Magnetically Tunable Microwave Filters*. McGraw-Hill Book Company, 1980, no. 0-89006-099-1, ch. 17, pp. 1001–1087.

[79] J. Warit, T. Ueda, and M. Tsutsumi, "Microwave circulator using yttrium iron garnet film," in *2000 Asia-Pacific Microwave Conference. Proceedings (Cat. No.00TH8522)*, Dec 2000, pp. 1212–1213.

[80] W. T. Soh, C. Y. Tan, and C. K. Ong, "Novel Coplanar Waveguide Circulator Using Metallized Yttrium Iron Garnet Disk," *Microwave and Optical Technology Letters*, vol. 55, no. 9, pp. 2143–2145, 2013. [Online]. Available: https://onlinelibrary.wiley.com/doi/abs/10.1002/mop.27755

[81] P. Roschmann, "Compact YIG bandpass Filter with Finite-Pole frequencies for Applications in Microwave Integrated Circuit," *IEEE Transaction on Microwave Theory and Techniques*, 1973.

[82] J. Krupka, B. Salski, P. Kopyt, and W. Gwarek, "Electrodynamic study of YIG filters and resonators," *Scientific Reports*, vol. 6, pp. 34 739 EP –, Oct 2016, article. [Online]. Available: https://doi.org/10.1038/srep34739

[83] E. Mallmann, S. Sombra, J. Goes, and P. Fechine, "Yttrium Iron Garnet: Properties and Applications Review," *Solid State Phenomena*, vol. 202, pp. 65–96, 05 2013.

[84] M. V. Delden, N. Pohl, K. Aufinger, and T. Musch, "A 32-48 GHz Differential YIG Oscillator With Low Phase Noise Based On a SiGe MMIC," in *2019 IEEE Radio and Wireless Symposium (RWS)*, Jan 2019, pp. 1–3.

[85] K. H. Carpenter and M. K. DaSilva, "Phase-locked yttrium iron garnet magnetometer for remote measurement of small field changes in a fluctuating background," *Review of Scientific Instruments*, vol. 53, no. 9, pp. 1414–1417, 1982. [Online]. Available: https://doi.org/10.1063/1.1137178

[86] Y. Sato and P. S. Carter, "A Device for Rapidly Aligning and Mounting Ferromagnetic Single Crystals Along Any Desired Axis," *IRE Transactions on Microwave Theory and Techniques*, vol. 10, no. 6, pp. 611–612, November 1962.

[87] M. Auer, "Novel Method to Orient Ferrimagnetic Single-Crystal Spheres," *IRE Transactions on Microwave Theory and Techniques*, vol. 10, no. 1, pp. 88–88, January 1962.

[88] M. L. Korber and K. J. Mueller, "Alignment method and system for YIG oscillator," U.S. patentus US6 313 711B1, 2000. [Online]. Available: https://patents.google.com/patent/US6313711

[89] J. F. Dillon, "Ferrimagnetic Resonance in Yttrium Iron Garnet," *Phys. Rev.*, vol. 105, pp. 759–760, Jan 1957. [Online]. Available: https://link.aps.org/doi/10.1103/PhysRev.105.759

[90] T. L. Jin, "Design of a YIG-tuned oscillator," Master's thesis, New Jersey Institute of Technology, 1974.

[91] J. Helszajn, *YIG Resonators and Filters*. Chichester, New York: John Wiley & Sons, 1985. [Online]. Available: https://www.amazon.com/YIG-Resonators-Filters-J-Helszajn/dp/047190516X?SubscriptionId=AKIAIOBINVZYXZQZ2U3A&tag=chimbori05-20&linkCode=xm2&camp=2025&creative=165953&creativeASIN=047190516X

[92] P. S. Carter, "Side-Wall-Coupled, Strip-Transmission-Line Magnetically Tunable Filters Employing Ferrimagnetic YIG Resonators," *IEEE Transactions on Microwave Theory and Techniques*, vol. 13, no. 3, pp. 306–315, May 1965.

[93] G. R. Eaton, S. S. Eaton, D. P. Barr, and R. T. Weber, *Quantitative EPR*. Springer-Verlag Wien, 2010, ch. 4.13 Modulation Amplitude Calibration, pp. 51–53. [Online]. Available: https://www.springer.com/gp/book/9783211929476

[94] D. G. Mitchell, R. W. Quine, M. Tseitlin, R. T. Weber, V. Meyer, A. Avery, S. S. Eaton, and G. R. Eaton, "Electron Spin Relaxation and Heterogeneity of the 1:1 α,γ-Bisdiphenylene-β-phenylallyl (BDPA)/Benzene Complex," *The Journal of Physical Chemistry B*, vol. 115, no. 24, pp. 7986–7990, 2011, pMID: 21574594. [Online]. Available: https://doi.org/10.1021/jp201978w

[95] W.-T. Pong, C. Durkan, H. Li, and W. Harneit, "Strategies for the Deposition of Free Radical Organic Molecules for Scanning-Probe Microscopy Experiments," *Journal of Scanning Probe Microscopy*, vol. 1, pp. 55–62, 12 2006. [Online]. Available: https://doi.org/10.1166/jspm.2006.006

[96] C. F. Koelsch, "Syntheses with Triarylvinylmagnesium Bromides. α,γ-Bisdiphenylene-β-phenylallyl, a Stable Free Radical," *Journal of the American Chemical Society*, vol. 79, no. 16, pp. 4439–4441, Apr. 1957. [Online]. Available: https://doi.org/10.1021/ja01573a053

[97] N. Azuma, T. Ozawa, and J. Yamauchi, "Molecular and Crystal Structures of Complexes of Stable Free Radical BDPA with Benzene and Acetone," *Bulletin of the Chemical Society of Japan*, vol. 67, no. 1, pp. 31–38, 1994. [Online]. Available: https://doi.org/10.1246/bcsj.67.31

[98] L. R. Becerra, G. J. Gerfen, B. F. Bellew, J. A. Bryant, D. A. Hall, S. J. Inati, R. T. Weber, S. Un, T. F. Prisner, A. E. Mcdermott, K. W. Fishbein, K. E. Kreischer, R. J. Temkin, D. J. Singel, and R. G. Griffin, "A Spectrometer for Dynamic Nuclear Polarization and Electron Paramagnetic Resonance at High Frequencies," *Journal of Magnetic Resonance, Series A*, vol. 117, no. 1, pp. 28 – 40, 1995. [Online]. Available: http://www.sciencedirect.com/science/article/pii/S1064185885799755

[99] A. Hajimiri and T. H. Lee, "Design issues in CMOS differential LC oscillators," *IEEE Journal of Solid-State Circuits*, vol. 34, no. 5, pp. 717–724, May 1999.

[100] Y. Shin, T. Kim, S. Kim, S. Jang, and B. Kim, "A Low Phase Noise Fully Integrated CMOS LC VCO Using a Large Gate Length pMOS Current Source and Bias Filtering Technique for 5-GHz WLAN," in *2007 International Symposium on Signals, Systems and Electronics*, July 2007, pp. 521–524.

[101] R. L. Fjerstad, "Some Design Considerations and Realizations of Iris-Coupled YIG-Tuned Filters in the 12-40 GHz Region," *IEEE Transactions on Microwave Theory and Techniques*, vol. 18, no. 4, pp. 205–212, April 1970.

[102] M. Aigle, G. Hechtfischer, W. Hohenester, R. Junemann, and C. Evers, "A systematic way to YIG-filter-design," in *2007 European Microwave Conference*, Oct 2007, pp. 668–671.

[103] Y. Gurevich and J. Velázquez-Pérez, *Peltier Effect in Semiconductors*. John Wiley and Sons, 04 2014, pp. 1–21.

[104] K. W. Whites, "Lecture 7: Transmission Line Matching Using Lumped L Networks," Tech. Rep., 2015.

[105] G. Boero, G. Gualco, R. Lisowski, J. Anders, D. Suter, and J. Brugger, "Room temperature strong coupling between a microwave oscillator and an ensemble of electron spins," *Journal of Magnetic Resonance*, vol. 231, pp. 133–140, Jun. 2013. [Online]. Available: https://doi.org/10.1016/j.jmr.2013.04.004

[106] K. C. Gupta, R. Garg, and I. J. Bahl, *Microstrip Lines and Slotlines*. Dedham: Artech House Books, Apr. 1979. [Online]. Available: https://www.ebook.de/de/product/20644982/ramesh_garg_microstrip_lines_and_slotlines.html

[107] B. C. Wadell, *Transmission Line Design Handbook*. Boston: ARTECH HOUSE INC, May 1991. [Online]. Available: https://www.ebook.de/de/product/4296409/brian_c_wadell_transmission_line_design_handbook.html

[108] F. Caspers, "RF engineering basic concepts: the Smith chart," *CAS - CERN Accelerator School: Specialised Course on RF for Accelerators*, no. arXiv:1201.4068, p. 22, Jan 2012, comments: 22 pages, contribution to the CAS - CERN Accelerator School: Specialised Course on RF for Accelerators; 8 - 17 Jun 2010, Ebeltoft, Denmark. [Online]. Available: http://cds.cern.ch/record/1417989

[109] Y. Anand and W. J. Moroney, "Microwave mixer and detector diodes," *Proceedings of the IEEE*, vol. 59, no. 8, pp. 1182–1190, Aug 1971.

[110] V. Milanovic, M. Gaitan, J. C. Marshall, and M. E. Zaghloul, "CMOS foundry implementation of Schottky diodes for RF detection," *IEEE Transactions on Electron Devices*, vol. 43, no. 12, pp. 2210–2214, Dec 1996.

[111] A. Beaumont, D. Giloteaux, A. V. Matheoud, M. Buzio, and G. Boero, "Electron Paramagnetic Resonance Magnetic Field Sensors for Particle Accelerators," 2020, submitted to RSI the 10 Feb. 2020 under reference RSI20-AR-00188.

[112] G. Boero, "private communications," Jan. 2020, signal and noise computation for the resonators.

[113] Y. E. Nesmelov, A. Gopinath, and D. D. Thomas, "Aqueous sample in an EPR cavity: sensitivity considerations," *Journal of Magnetic Resonance*, vol. 167, no. 1, pp. 138 – 146, 2004. [Online]. Available: http://www.sciencedirect.com/science/article/pii/S1090780703004348

[114] J. P. Goldsborough, M. Mandel, and G. E. Pake, "Influence of Exchange Interaction on Paramagnetic Relaxation Times," *Physycal Review Letters*, vol. 4, pp. 13–15, Jan 1960. [Online]. Available: https://link.aps.org/doi/10.1103/PhysRevLett.4.13

[115] A. V. Matheoud, N. Sahin, and G. Boero, "A single chip electron spin resonance detector based on a single high electron mobility transistor," *Journal of Magnetic Resonance*, vol. 294, pp. 59 – 70, 2018. [Online]. Available: http://www.sciencedirect.com/science/article/pii/S1090780718301733

[116] A. V. Matheoud, "Electron Spin Resonance detectors from 400 MHz to 360 GHz," Ph.D. dissertation, EPFL, Lausanne, 2019. [Online]. Available: http://infoscience.epfl.ch/record/264213

[117] A. Matheoud, N. Şahin Solmaz, L. Frehner, and G. Boero, "Microwave inductive proximity sensors with sub-pm/ Hz resolution," *Sensors and Actuators A: Physical*, vol. 295, 05 2019.

[118] E. Ortigueira, I. Bastos, L. B. Oliveira, J. P. Oliveira, and J. Goes, "A simplified design of a MOSFET-only wideband Gilbert Cell," in *Proceedings of the 18th International Conference Mixed Design of Integrated Circuits and Systems - MIXDES 2011*, June 2011, pp. 225–230.

[119] A. V. Matheoud, "Private communications," Jan. 2020, oscillator schematics reproduced with permission.

[120] A. Drozd, A. Honma, S. Kaufmann, F. Manolescu, and I. McGill, "Reliability Tests of Aluminium Wedge Wire Bonding on Auto-catalytic Silver Immersion Gold (ASIG) PCB Metallization," CERN, Geneva, techreport PH-EP-Tech-Note-2011-002, Dec 2011. [Online]. Available: https://cds.cern.ch/record/1408696

[121] T. Yalcin and G. Boero, "Single-chip detector for electron spin resonance spectroscopy," *Review of Scientific Instruments*, vol. 79, no. 9, p. 094105, 2008.

[122] J.-P. Burnet, C. Carli, M. Chanel, R. Garoby, S. Gilardoni, M. Giovannozzi, S. Hancock, H. Haseroth, K. Hübner, D. Küchler, J. Lewis, A. Lombardi, D. Manglunki, M. Martini, S. Maury, E. Métral, D. Möhl, G. Plass, L. Rinolfi, R. Scrivens, R. Steerenberg, C. Steinbach, M. Vretenar, and T. Zickler, *Fifty years of the CERN Proton Synchrotron: Volume 1*, ser. CERN Yellow Reports: Monographs, S. Gilardoni and D. Manglunki, Eds. Geneva: CERN, 2011. [Online]. Available: http://cds.cern.ch/record/1359959

[123] M. Juchno, "Magnetic Model of the CERN Proton Synchrotron," phdthesis, EPFL, Lausanne, Switzerland, Sep. 2013, no 5964.

[124] R. Gouiran, "Decouplage des champs quadrupolaire et sextupolaire avec les enroulements polaires du CPS," CERN, techreport MPS/SM/Note 74-26, Dec. 1974.

[125] P. Lefèvre and R. Gouiran, "Projets de nouveaux enroulements polaires pour le CPS. Part 1: Champs multipolaires nécéssaires (Lefevre, P)," CERN, Geneva, Tech. Rep. CERN-MPS-DL-Note-74-11, Jun 1974. [Online]. Available: http://cds.cern.ch/record/1266239

[126] R. Wasef, "8th Order Super-Structure Resonance driven by Space Charge," phdthesis, Johann Wolfgang Goethe University, Nov 2017, presented 28 Jun 2018. [Online]. Available: https://cds.cern.ch/record/2670261

[127] A. Beaumont, "Reliability of magnetic field markers for the PS accelerator," CERN, techreport EDMS:2275495, Dec. 2015. [Online]. Available: https://edms.cern.ch/document/2275495/1

[128] A. Beaumont and M. Buzio, "The New LEIR B-Train," CERN, Geneva, Switzerland, techreport EDMS: 2308150, Dec. 2019, internal Note 2019-49. [Online]. Available: https://edms.cern.ch/document/2308150/1

[129] S. Albright, R. A. Fernández, M. E. Angoletta, H. Bartosik, A. Beaumont, G. Bellodi, N. Biancacci, M. Bozzolan, M. Buzio, F. D. Lorenzo, A. Frassier, D. Gamba, S. Hirlander, A. Huschauer, S. Jensen, V. Kain, G. Kotzian, D. Kuchler, A. Latina, T. Levens, E. Mahner, E. Manosperti, O. Marqversen, D. Nicosia, M. O'Neil, E. Ozturk, A. S. Hernandez, R. Scrivens, G. Tranquille, F. J. C. Wenander, C. Wetton, and M. Zampetakis, "Review of the LEIR operation in 2018," 2020, aST note.

[130] R. Alemany-Fernández, S. Albright, O. Andujar, M. E. Angoletta, J. Axensalva, H. Bartosik, G. Baud, N. Biancacci, M. Bozzolan, S. Cettour Cave, K. Cornelis, J. Dalla-Costa, M. Delrieux, A. Dworak, A. Findlay, F. Follin, A. Frassier, M. Gabriel, A. Guerrero-Ollacarizqueta, M. Haase, S. Hirlaender, S. Jensen, V. Kain, L. V. Kolbeck, Y. Le Borgne, D. Manglunki, O. Marqversen, S. Massot, D. Moreno Garcia, D. Nicosia, S. Pasinelli, L. Pereira, D. Perez, A. Rey, J. Ridewood, F. Roncarolo, A. Saá Hernández, R. Scrivens, O. G. Sveen, G. Tranquille, and E. Veyrunes, "Performance of the CERN Low Energy Ion Ring (LEIR) with Xenon beams," in *Proceedings, 9th International Particle Accelerator Conference (IPAC 2018): Vancouver, BC Canada, April 29-May 4, 2018*, 2018, p. TUPAF020. [Online]. Available: http://cds.cern.ch/record/2648426

[131] M. Brice, "View of the LEIR ring (Low-Energy Ion Ring). Vue de l'anneau du LEIR (l'anneau d'ions de basse énergie)," Sep 2005, cERN PhotoLab / Experiments and Tracks. [Online]. Available: http://cds.cern.ch/record/951445

[132] G. Boero, "private communications," Jul. 2018, phase detection.

Glossary

AD Antiproton Decelerator. 6, 83

B-Train Real time magnetic field system. 2, 11, 12, 75–77, 85, 90–96, 98, 103, 104, 111
BDPA α,γ-Bisdiphenylene-β-phenylallyl paramagnetic free radial with Benzene. 19, 31, 34, 47, 48, 54, 58, 124

CMOS Complementary Metal Oxide Semiconductor. 57
CTRI Control timing electronic card for PCIe chassis, receive the CERN master timing frame (Telegram). 104

DAQ Data Acquisition System. 25, 48, 50, 120, 122, 124

ELENA Extra Low ENergy Antiproton. 6, 9, 11, 88
EMI Electro-Magnetic Interference. 64, 111
EPR Electron Paramagnetic Resonance. 2, 15, 25, 34, 47–50, 58, 70, 103, 104, 124
ESR Electron Spin Resonance. iii, 2, 13, 15, 16, 18, 20, 26, 31, 35, 38, 76, 77, 119

F8L Figure of eight Loop. 76
FE Finite Element simulation. 31, 84
FIRESTORM Field In REal-time STreaming from Online Reference Magnets. 11
FMR Ferrimagnetic Resonance. 2, 13, 18, 19, 25, 28, 32, 33, 35, 41, 44, 76–78, 80, 81, 84–86, 92, 93, 120, 123, 124
FPGA Field-Programmable Gate Array. 111
FWHM full width at half maximum. 42, 52

GaYIG Gallium doped Yttrium Iron Garnet alloy. 18, 19, 30, 33, 36, 119, 122, 123
GCPW Grounded Co-Planar Waveguide. 35–38, 119

HDMI High Definition Multimedia Interface. 104

LED Light-Emitting Diode. 104
LEIR Low Energy Ion Ring. iii, 2, 6, 9, 11, 28, 43, 44, 75, 83, 87, 89–98, 100
LF Low-Frequency. 41, 48, 50
LHC Large Hadron Collider. iii, 1, 5–7

Linac3 Linear accelerator 3, providing ion beam. 89
LLRF Low Level Radio-Freuqency. 2, 10, 87, 92, 94, 95, 98
LS2 CERN Long Shutdown number 2. 90
LVDS Low Voltage Differential Signaling. 104, 111

MM Magnetic Measurement. 8, 10

NMR Nuclear Magnetic Resonance. 2, 8, 13, 15, 17, 18, 25, 26, 31

PCB Printed Circuit Board. 32, 47, 48, 57, 103
PFW Pole Face Winding. 76, 80
PLL Phase Locked Loop. 59, 103, 104, 111, 117
PPM Pulse-to-Pulse Modulation. 91
PS Proton Synchrotron. iii, 2, 6, 9, 11, 13, 28, 42, 44, 75–77, 80, 100
PSB Proton Synchrotron Booster. 6, 9, 11, 75, 100

RF Radio-Freqency. 6, 9, 18, 41, 44, 49, 50, 92, 94

SMD Surface Mount Device. 31
SNR Signal-to-Noise Ratio. 52, 53, 55, 67, 72
SPEC Standard CERN control electronic card for PCIe chassis, including extension card connector for devices control. 103, 104, 111
SPI Serial Peripheral Interface. 103, 104
SPS Super Proton Synchrotron. 6, 7, 9, 10

TeV Tera electron Volt. 5
TTL Transistor–Transistor Logic. 104

VCO Votage Controlled Oscillator. 103, 111
VCXO Voltage Controlled Crystal Oscillator. 103
VNA Vector Network Analyser. 30, 38

WR White Rabbit ethernet protocol network including timing synchronisation. 89

YIG Yttrium Iron Garnet alloy. 13, 18–21, 25, 31–33, 36, 43, 44, 52, 54, 76, 77, 80, 81, 103